# IMPROVED UNDERSTANDING AND CONTROL OF MAGNESIUM-DOPED GALLIUM NITRIDE BY PLASMA ASSISTED MOLECULAR BEAM EPITAXY

A Dissertation
Presented to
The Academic Faculty

By

**Shawn D. Burnham**

In Partial Fulfillment
Of the Requirements for the Degree
Doctor of Philosophy in the
School of Electrical and Computer Engineering


August, 2007

**IMPROVED UNDERSTANDING AND CONTROL OF MG-DOPED GAN BY PLASMA ASSISTED MOLECULAR BEAM EPITAXY**

Dr. W. Alan Doolittle
School of Electrical and Computer Engineering
*Georgia Institute of Technology*

Dr. Ian T. Ferguson
School of Electrical and Computer Engineering
*Georgia Institute of Technology*

Dr. John D. Cressler
School of Electrical and Computer Engineering
*Georgia Institute of Technology*

Dr. John F. Dorsey
School of Electrical and Computer Engineering
*Georgia Institute of Technology*

Dr. W. Brent Carter
School of Materials Science and Engineering
*Georgia Institute of Technology*

Date Approved: June 2007

The secret things belong to the LORD our God, but the things revealed belong to us and to our children forever, that we may follow all the words of this law.

Moses, Deuteronomy 29:29

# ACKNOWLEDGEMENTS

First and foremost, I would like to thank Jesus Christ for allowing me access to the infinite wisdom of the God of this universe. Second, I would like to thank my amazing wife, the definition of love, patience and devotion. Third, I would like to thank my parents and family for the many years of support and molding. I could never repay any of these gifts.

Dr. William Alan Doolittle is the finest mentor I have ever known. His invaluable guidance has taught me to blend imagination with knowledge for truly exciting research. Without his consistent, but patient dissemination of knowledge and commitment to individual development, this work would not exist. As a testament to his influence, his research group members have also been extremely helpful, and deserve individual mention: Walter Henderson, Gon Namkoong, Alexander Carver, David Pritchett, Elaissa Trybus, Kyoung-Keun Lee, W. Laws Calley III, and Daniel Billingsley. There have also been many helpful undergraduates that have come and gone throughout the years.

Dr. Edward Thomas was very helpful in interpreting data from and maintaining the SIMS system. The MiRC cleanroom staff was very helpful with all processing steps and I'd like to individually thank Gary Spinner, Brandon Harrington, Tran-Vinh Nguyen, and Charlie Suh. I would also like to express my appreciation for my dissertation reading committee for their guidance and feedback: Dr. Ian Ferguson, Dr. John Cressler, Dr. John Dorsey, and Dr. W. Brent Carter.

This work was supported by basic science grants from the Office of Naval Research, monitored by Dr. Colin Wood, and by the NEW-EPIC MURI program from the Air Force Office of Scientific Research, monitored by Dr. Donald Silversmith.

TABLE OF CONTENTS

LIST OF TABLES

LIST OF FIGURES

# SUMMARY

Control of conductivity through doping is a prerequisite for the development of any semiconductor, and control of p-type doping has proven especially difficult with gallium nitride (GaN). By an improved understanding of magnesium (Mg) doped GaN through an exhaustive review of current limitations, increased control over the material was achieved by addressing several of these issues. The review of Mg-doped GaN reveals that the material suffers from a low solubility of Mg in GaN, a tendency of Mg to accumulate and segregate at surfaces, a memory effect of Mg in a growth chamber, a high vapor pressure of Mg at low temperatures, a low sticking coefficient of Mg on GaN, a deep ionization energy of Mg acceptors in GaN, unintentional hydrogen and oxygen doping, a significant compensation of Mg acceptors at high dopant concentrations, and a drastic dependence upon the growth regime or III – V ratio. As these issues were addressed, repeatable and reliable Mg-doped GaN became a reality using the tools and techniques developed as a result.

To address the issues of the memory effect, low sticking coefficient and high vapor pressure of Mg, a new Mg dopant source was implemented, characterized and modeled for p-type doping of GaN with plasma-assisted molecular beam epitaxy (PAMBE). The device enhanced the sticking coefficient by energizing the outgoing Mg flux, and also allowed the first reported demonstration of an abrupt junction between two non-zero Mg-doped GaN films and the first reported demonstration of a graded Mg-doped GaN film. The significant compensation of Mg acceptors at high dopant concentrations was used advantageously to develop a new *ex situ* resistivity analysis

technique using secondary ion mass spectroscopy (SIMS) to characterize doping of buried layers. The new technique was used to identify the barrier between conductive Mg doping and resistive Mg doping by analyzing a film with increased Mg concentration, which was then used to optimize Mg-doped GaN. Because Mg doping exhibits a drastic dependence upon the growth regime or III – V ratio, a new growth and regime characterization technique was developed using reflection-high energy electron diffraction (RHEED). The technique uses specific RHEED intensity responses to repeat growth conditions and assure III – V ratio, or growth regime, for Mg-doped GaN. During the development of this technique, a new surface kinetics growth model for III-nitrides was discovered based on desorption mass spectroscopy (DMS) observations. This model suggests preferential buildup of the metal bilayer before growth begins with an unfamiliar cation-anion exchange process initially upon metal shutter opening, which has important implications for Mg-doped GaN because of surface segregation issues. Using the new RHEED growth and regime characterization technique, a new growth technique called metal modulated epitaxy (MME) was developed. MME was determined to increase repeatability, uniformity and smoothness of PAMBE grown films.

The MME technique was enhanced with a closed-loop control using real-time feedback from RHEED transients to control shutter transitions. This enhancement, called "smart shuttering," led to improved growth rate and further improvement of surface roughness and grain size. Moreover, growth rate and grain size were repeatable within low percentages using the technique. Effects of smart-shuttering MME were observed with silicon (Si), Mg and indium (In) during GaN growths. Repeatable Mg-doped GaN was achieved with a variation of less than 8%, and a peak hole carrier concentration of

$4.7 \times 10^{18}$ $cm^{-3}$. However, no appreciable amount of In was incorporated when attempting to grow indium gallium nitride (InGaN) using MME, as a result of high In desorption. Therefore, by understanding the limitations of Mg-doped GaN, most of the problems were overcome using different tools and techniques for increased control. Using the results of these studies, consistent Mg-doped GaN films can be grown with repeatability and reliability.

# CHAPTER 1: INTRODUCTION

Conventional elemental and III-V compound semiconductors have proven to be extremely useful, but are not suitable for many applications. For example, high-temperature and high-power transistors are necessary for various automotive, power distribution and avionics applications. Furthermore, short wavelength light emitters and detectors are necessary for various display, storage and communication applications. Conventional semiconductors suffer from large background carrier concentrations, low breakdown electric fields and indirect or narrow band gaps. The gallium nitride (GaN) and related alloy material system exhibits qualities that make it an excellent solution for some of the application needs unmet by conventional semiconductors. However, issues of p-type doping GaN with magnesium (Mg) must first be addressed, understood, and overcome before this material system is able to meet these needs.

Prior to October, 1932, a nitride of each member of the known Group III elements [Boron (B), Aluminum (Al), Gallium (Ga), Indium (In), Thallium (Tl)] had been reported, with the exception of gallium. At that time, however, an ever-growing development began with the first report of powder "Gallic Nitride," what we now know of as "Gallium Nitride" (GaN), by flowing ammonia gas over metallic gallium at high temperatures (700-1000° C) [1]. Though much progress has already been made in the nearly 75 years since, GaN is still the topic of a phenomenal amount of research because of its useful properties. For example, GaN exhibits a direct band transition with a band gap of [2]

$$E_G(T) = 3.486 - \frac{8.32 \times 10^{-4} T^2}{835.6 + T} eV, \quad (1)$$

which is a function of temperature, T, in Kelvin. This equation results in a band gap of approximately 3.44 eV at room temperature [3]. Such a wide band gap is useful for electrical applications that are exposed to high temperature. Likewise, the approximately 365 nm wavelength emitted by photons generated by the recombination of electrons and holes across the band gap [4] is useful for color displays, laser printers, high-density information storage and underwater communication [5]. GaN was again reported synthesized in 1938 [6] and 1959 [7], with the latter including photoluminescence (PL) data and the first attempt at Mg doping. However, it wasn't until 1969 that larger areas (2 $cm^2$) of GaN were deposited on sapphire using chemical vapor deposition (CVD) [8]. The first GaN diode was insulating-to-n-type and created in 1971 [9], but the material was still relatively low quality and suffered from a large native background electron concentration, thought to be caused by nitrogen vacancies [10] or oxygen impurities [11]. The quality of GaN was greatly improved in 1983 with the introduction of an AlN buffer layer that helped to nucleate and produce smooth GaN films [12].

Though n-type conductivity was easy to achieve with GaN, it was not until 1989 that p-type conductivity was first obtained and the first p-n junction came with it [13]. The Mg acceptors had been activated by liberating bonded hydrogen, using low-energy electron beam irradiation (LEEBI). In 1992, it was discovered that Mg-doped GaN from hydrogen-containing growth systems could also be annealed in nitrogen to thermally liberate the hydrogen from the Mg acceptors, making the process much easier and reproducible [14]. Magnesium was the first p-type dopant of GaN resulting in conductivity [13] and is now the most widely used and studied dopant for p-type GaN.

However, acceptable hole concentrations and control of Mg-doped GaN have been a challenge because of various doping difficulties, including a high vapor pressure of Mg at low temperatures [15], memory effects of Mg in a growth chamber [16, 17], a low sticking coefficient of Mg on GaN, a tendency of Mg to accumulate and segregate at surfaces [18], a low solubility of Mg into GaN [11], a deep ionization energy of Mg acceptors in GaN [19] and a significant compensation of Mg acceptors at high dopant concentrations [11]. The result is a narrow window of Mg-doped GaN growth conditions that yield low-resistivity GaN, below which the material is highly resistive because of the lack of free carriers and above which it is highly resistive because of some of the complications listed above. Therefore, the need for acceptable hole concentrations and adequate control of Mg-doped GaN have led to much work devoted to systematic control and optimization of Mg-doped GaN [20-29].

## 1.1 Molecular beam epitaxy

Solid source molecular beam epitaxy (MBE) is the most frequently used epitaxial growth technique based on the principles of physical vapor deposition (PVD). MBE involves a beam nature of mass flow toward a crystalline substrate in an ultra-high vacuum (UHV) environment (base pressure less than $10^{-9}$ Torr [30]). Precise control over the mass flow beam is achieved by evaporating source material in the Knudsen mode from a furnace called an effusion cell. Thin crystalline epitaxial films form on the crystalline template substrate when these thermal molecular or atomic beams react on the substrate surface [31].

MBE was first performed with GaAs in 1968 [32], but it wasn't until 1970 that the term "molecular beam epitaxy" was used [33]. The technique was developed out of

necessity, as demand grew for a growth technology that would produce single crystalline films as thin as 500 Å [34]. However, it also provided the advantages of a cleaner growth process and lower growth temperatures over preceding high-pressure and high-temperature growth techniques. Figure 1 and Figure 2 show illustrations of typical MBE configurations and associated components.

For the presented experiments, a Riber 32 MBE system was used for epitaxial growth. The Riber 32 MBE system has three vacuum chambers: an introduction chamber, a growth chamber and an analytic chamber that separates the others. The growth chamber is equipped with five standard effusion cells: four for the group III (metal) elements (Ga, In and two for Al), as well as one for the dopant silicon (Si). The remaining two ports were occupied by a Veeco 200cc Corrosive Series Valved Cracker for the Mg source and a Veeco UNI-Bulb radio-frequency (rf) plasma for the nitrogen source. The plasma source was operated at 350 W with a mass flow controller (MFC) controlling the flow of high-purity molecular nitrogen into the source. The nitrogen flow rate for the plasma source was set to 0.35 sccm (sccm denotes cubic centimeters per min at standard temperature and pressure) for AlN using the Namkoong method [35] and slow GaN growths, and 0.5 or 1.3 sccm for AlN using the MME method [26] and faster GaN growths. The range of flow rates is a result of changing the plasma aperture, which is described in Appendix B, but resulted in approximately the same growth rate.

To monitor the growth surface and environment *in situ*, a Staib 20 KeV reflection-high energy electron diffraction (RHEED) gun was used with a filament current of 1.5 A and a Stanford Research Systems RGA200, mounted in the growth chamber facing the sample, was used with an electron multiplier for desorption mass spectroscopy (DMS).

The fluorescent RHEED screen was monitored with a 12-bit (or 22-bit as developed herein) charge-coupled device (CCD) camera connected to a computer using k-Space Associates kSA400 software for analysis

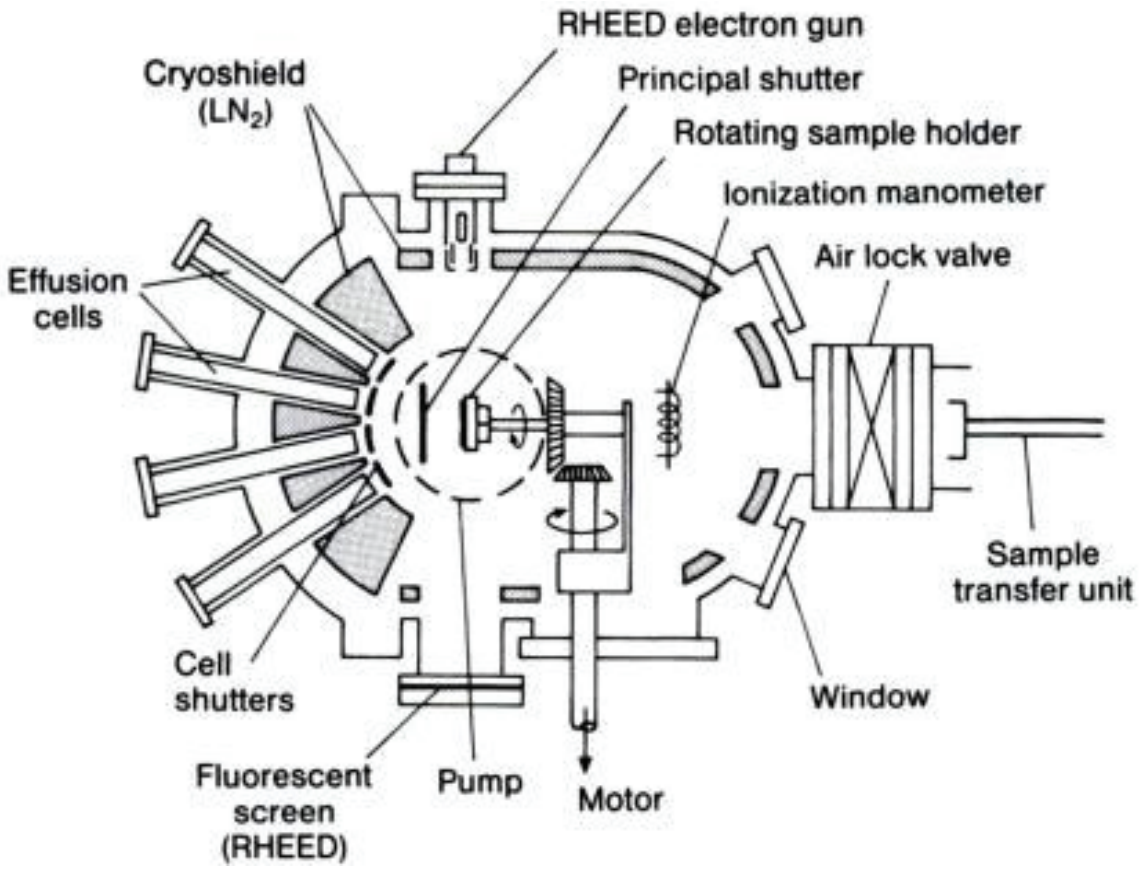


Figure 1: Schematic illustration of a MBE machine and associated components [36].

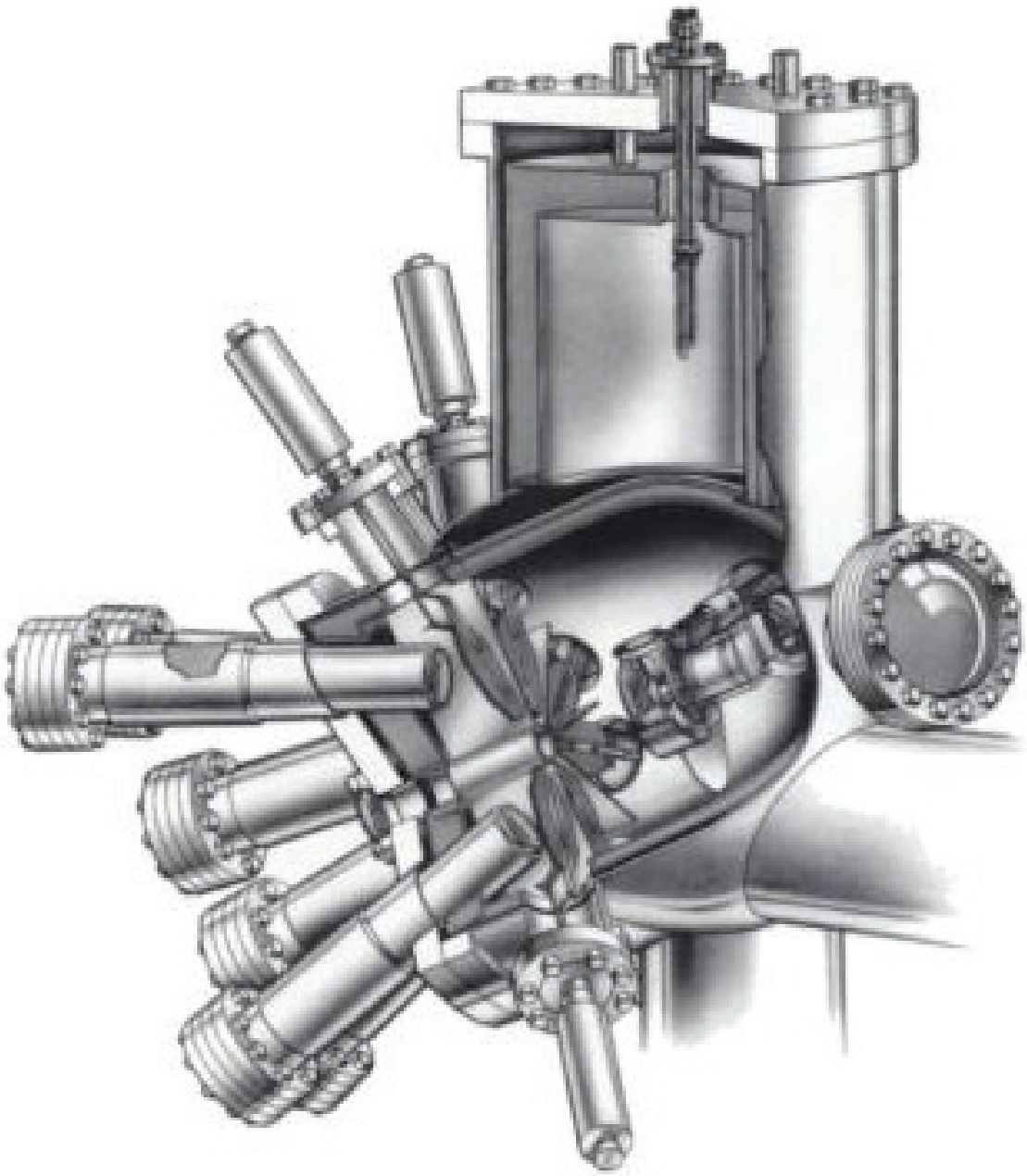

Figure 2: Cutaway illustration of a MBE machine showing typical three dimensional geometry [31].

## 1.2 GaN properties

Wurtzite GaN is a polar material with lattice constants of a = 3.189 Å and c = 5.185 Å [37]. Because GaN substrates are not readily available, GaN is most commonly

grown in a polar direction on [0001] sapphire (with a = 4.765 Å , c = 12.982 Å and 15% mismatch [38]), or silicon carbide (SiC) (with a = 3.0806 Å , c = 15.1173 Å and 3.1% mismatch [38]). Polarity describes whether the bonds along the c-direction are from cation sites to anion sites, or vice versa, from bottom to top. It has been established that the [0001] direction is "Ga polar," and the bonds along the positive c-direction are from cation (Ga) to anion (N) atoms, from bottom to top. Likewise, the $[000\bar{1}]$ direction is "N polar" and has c-direction bonds from anion (N) to cation (Ga) atoms, from bottom to top, as shown by Figure 3 [39].

Figure 4 shows a comparison of GaN to other semiconductor's band gap versus lattice constant. GaN can be alloyed with other materials such as AlN and InN, also shown in the figure, for a wide range of band gap engineering. Upon the discovery of GaN, Johnson noted that it "is an exceedingly stable compound" because it did not begin to decompose until reaching temperatures near 1000° C [1]. The wide band gap of GaN and thermal stability make this material ideal for high-temperature usage, since the intrinsic carrier concentration is much lower than with conventional semiconductors at elevated temperatures [40], as seen in Table 1. Likewise, the chemical stability of the material makes it ideal for harsh chemical environments, though this also makes etching GaN difficult [37]. GaN devices also exhibit a large breakdown electric field, compared to conventional semiconductors, of $\varepsilon_{BR} \approx 3 \times 10^6$ V/cm [41] (listed in Table 1), which is useful for high-power applications. The GaN electron saturation drift velocity is also high compared to conventional semiconductors, at $v_{sat} = 2.5 \times 10^5$ m/s and listed in Table 1, which makes GaN a good material for high-frequency devices. Table 1 summarizes

some common properties of wurtzite GaN compared to those of the traditional semiconductors, silicon (Si) and gallium arsenide (GaAs).

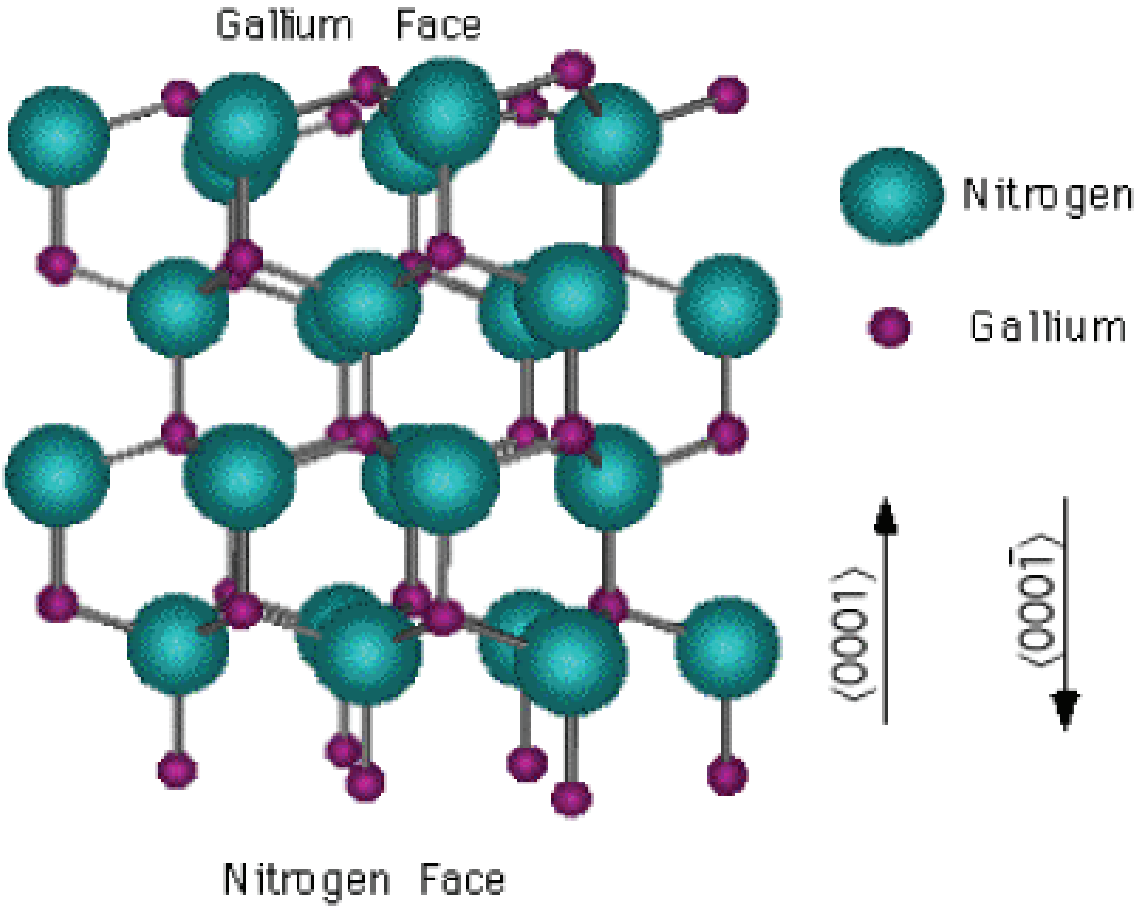


Figure 3: Wurtzite GaN crystal structure showing polarity conventions (color online) [39].

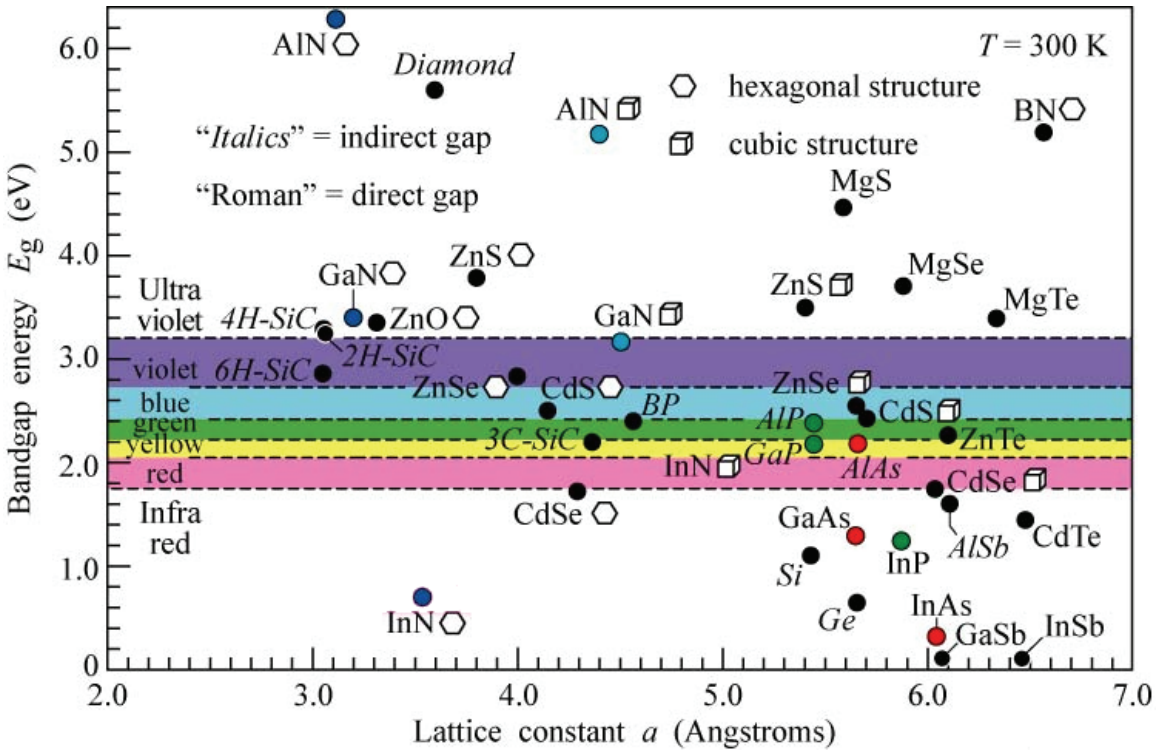


Figure 4: Band gap energy versus lattice constant for common semiconductors at room temperature (color online) [42].

Table 1: Properties of wurtzite GaN compared to traditional semiconductors.

| Property | Symbol [unit] | GaN [Ref.] | Si [Ref.] | GaAs [Ref.] |
|---|---|---|---|---|
| Band gap (T = 300K) | $E_G$ [eV] | 3.44 [2] | 1.12 [43] | 1.42 [43] |
| Lattice constant (T = 300K) | a [Å] | 3.189 [37] | 5.43 [43] | 5.65 [43] |
| | c [Å] | 5.185 [37] | | |
| Intrinsic carriers (T = 300K) | $n_i$ [$cm^{-3}$] | $1.9 \times 10^{-10}$ | $1 \times 10^{10}$ [43] | $2 \times 10^{6}$ [43] |
| Dielectric constant | $K_r$ | 9.5 [44] | 11.8 [43] | 12.9 [45] |
| Electron mass | $m_e^*/m_0$ | 0.2 [44] | 1.18 [43] | 0.066 [43] |
| Hole mass | $m_h^*/m_0$ | 0.95 to 1.1 [46] | 0.81 [43] | 0.52 [43] |
| Break down electric field | $\varepsilon_{BR}$ [V/cm] | $3 \times 10^{6}$ [41] | $3 \times 10^{5}$ [47] | $2.5 \times 10^{5}$ [47] |
| Saturation drift velocity | $v_{sat}$ [cm/s] | $2.5 \times 10^{7}$ [41] | $1 \times 10^{7}$ [47] | $1 \times 10^{7}$ [47] |

The structure of III-nitride surface morphologies has been studied through theoretical models [48-51] and experimentation [49-61] in an attempt to further define and characterize three distinct regimes of growth: N-rich, metal-rich with droplets and an intermediate metal-rich regime without droplets. Most of these studies focus only on the N-rich and droplet regimes, but others provide information on the benefits of growing in the intermediate regime [52-54], which exhibits a laterally contracted metal bilayer at the surface, without disadvantageous droplet formation [48-51]. Figure 5a shows a diagram relating the growth regimes of GaN to substrate temperature and Ga flux. The droplet regime barrier was defined by experimentally fitting [52]

$$F_{Ga}^{*} - F_{N}^{\text{available}} = \left(2.2 \times 10^{15}\,\text{nm/min}\right) \times \exp\left(\frac{-\left(2.832\,\text{eV}\right)}{kT}\right) \quad (2)$$

to empirical data for excess Ga flux, as shown in Figure 5b, where $F_{Ga}^{*}$ is the flux of Ga at the droplet regime barrier, $F_{N}^{\text{available}}$ is the available nitrogen (both in units of nm/min), k is Boltzmann's constant and *T* is temperature in K. Figure 6 and Figure 7 show atomic force microscopy (AFM) and transmission electron microscopy (TEM) data, respectively, for samples grown in each of the three regimes. Although the best surface morphology results are shown for the sample grown in the droplet regime, the presence of droplets can be undesirable for device structures. The intermediate regime yields the smoothest morphology in the absence of droplets. However, only a few of these works attempt to develop a quantitative, reproducible procedure for determining growth regime *in situ* for all three regimes.

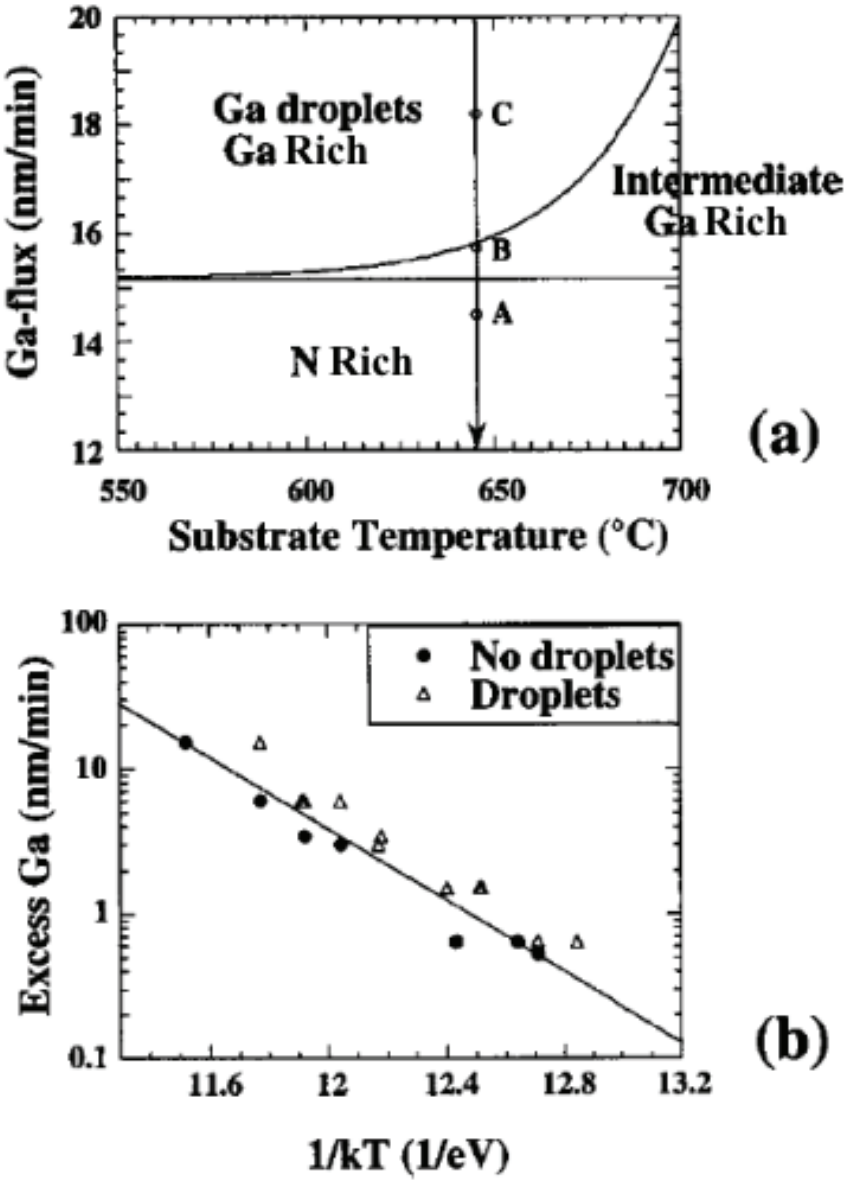


Figure 5: (a) Surface morphology diagram for empirical data showing the behavior of the three regimes of GaN growth with temperature and Ga flux. (b) Excess Ga, defined by equation 2, versus 1/kT, showing empirically derived droplet regime barrier [52].

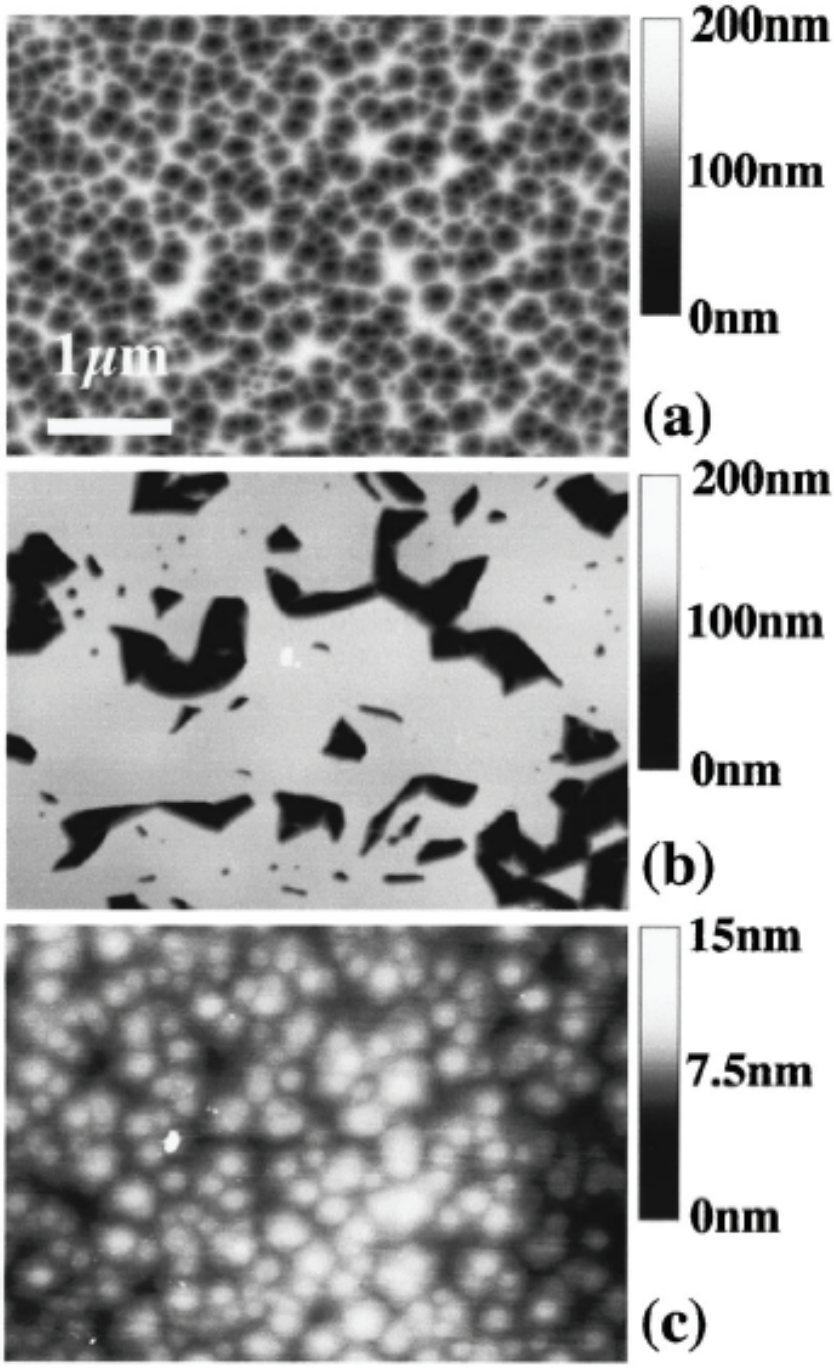


Figure 6: AFM images of samples grown in the three different growth regimes, with labels corresponding to the points in Figure 5a, showing smoother morphology with increasing Ga flux [52].

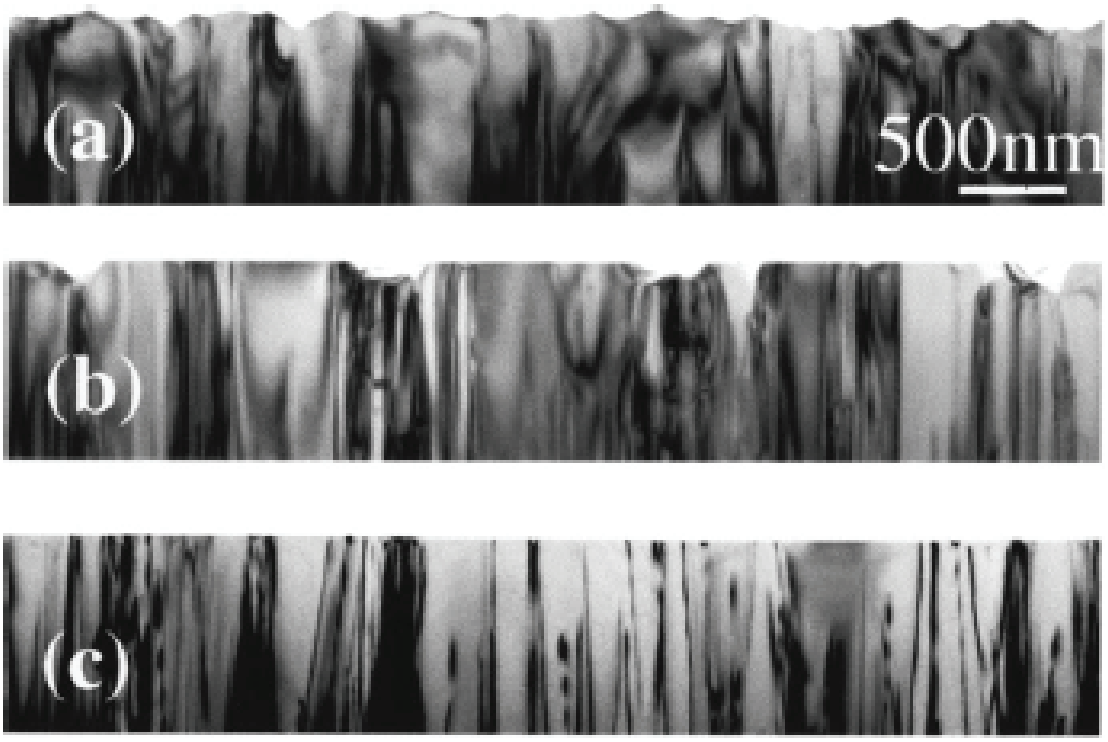


Figure 7: TEM images of samples grown in the three different growth regimes, with labels corresponding to the points in Figure 5a, showing smoother morphology with increasing Ga flux [52].

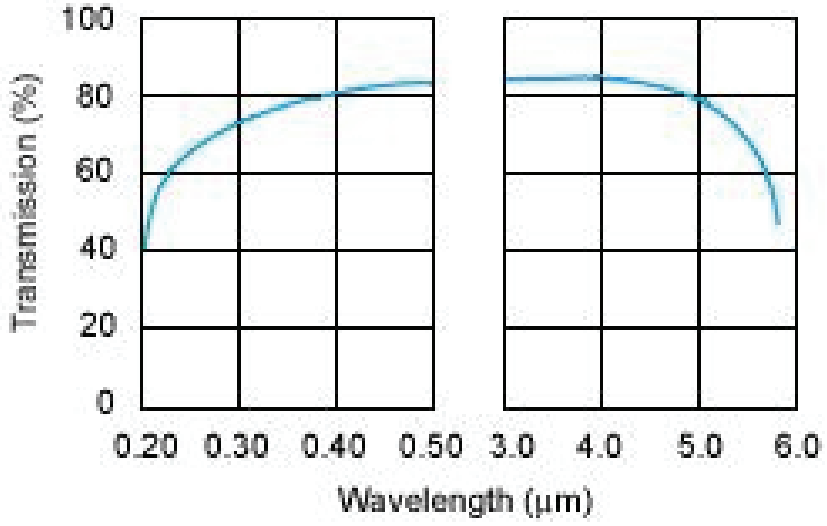


Figure 8: Transmission curve for sapphire, showing transparency at infrared wavelengths (greater than 0.75 μm) (color online) [55].

All films in the presented experiments were grown on [0001] basal c-plane oriented sapphire substrates, approximately 430 μm thick, with a polished growth surface and rough backside. Refractory metals were deposited on the rough backside to promote thermal absorption, since sapphire is transparent to heat and infrared radiation at low temperatures, as seen in Figure 8. The samples were chemically cleaned before loading into the vacuum system, as detailed in appendix A.1. Before growing GaN, a nitridation layer and AlN buffer layer were grown, as detailed in appendix A.2.

# CHAPTER 2: DIFFICULTIES OF MG-DOPED GAN

To achieve p-type doping with III-V semiconductors, either group IV atoms should substitute the group V atoms, or group II atoms should substitute the group III atoms. Unfortunately with the GaN material system, the group IV atoms (Si, germanium (Ge) and carbon (C)) do not satisfy this requirement. Si and Ge prefer to substitute for the group III atom, thus acting as donors [56, 57] and C is amphoteric, substituting both group III and group V atoms, and resulting in highly resistive material [58]. Furthermore, it has been found that the group II elements with d-shells (i.e., calcium and higher masses) form deep acceptor levels, thought to be due to resonance with lower valance bands [59]. The remaining practical alternatives to p-type doping are Mg and Be, with Mg being the most successful p-type dopant for GaN.

## 2.1 Solubility

Perhaps the greatest difficulty of doping GaN with Mg is the issue of solubility. Solubility is the ability of a solute to be dissolved in a solvent. In the case of a crystalline semiconductor material, it is specifically the ability of a dopant to incorporate into the lattice. In general, the more alike a solute and solvent are, the easier it is for the solute to replace the solvent in a material [60]. Likewise, the solubility for a substitutional impurity depends on the chemical similarity and size difference between a dopant atom and the host atom it is intended to replace. However, many times there exists no impurity that closely resembles the host atom, which makes the solubility low and doping difficult. Exceeding the solubility limit produces competing compound phases, impurity

segregation or precipitation and substitution on the "wrong site." Competing compound phases are a problem with p-type doping of GaN with Mg [11, 61].

The low solubility limit of Mg in GaN can be seen by comparing the limiting Mg concentration to that of pure Ga and N atoms in wurtzite GaN. The total concentration of Ga and N atoms in pure wurtzite GaN can be found using [62]

$$[\mathrm{GaN}] = \frac{n_{GaN}}{V_{GaN}} = \frac{6}{\frac{3\sqrt{3}}{2}a^2 c} = \frac{12}{3\sqrt{3}\left(3.189\times10^{-8}\,\mathrm{cm}\right)^2\left(5.185\times10^{-8}\,\mathrm{cm}\right)} = 4.379\times10^{22}\,\mathrm{cm}^{-3} \tag{3}$$

for a large hexagonal close-packed (HCP) unit cell, where $V_{GaN}$ is the volume of a large HCP unit cell, $n_{GaN}$ is the number of atoms in a large HCP unit cell and a and c are lattice constant parameters for GaN [37]. Furthermore, it has been found that the Mg saturation limit for GaN is reached at a Mg concentration of the mid $10^{19}$ $cm^{-3}$ range [61]. Therefore, by comparing the Mg concentration limit to the GaN atomic concentration, the maximum Mg weight percentage allowed before exceeding saturation can be found using

$$\frac{M_{Mg}}{.5\left(M_{Ga}+M_{N}\right)}\frac{[\mathrm{Mg}]}{[\mathrm{GaN}]} \approx \frac{24.3}{.5(69.7+14)}\frac{5\times10^{19}}{4.379\times10^{22}} \approx 0.066\ \mathrm{wt.\%} \tag{4}$$

where $M_{Mg}$, $M_{Ga}$ and $M_N$ are the atomic masses for Mg, Ga and N respectively. From this calculation, the impact of the extremely small solubility limit can be appreciated. It is because of this low solubility limit that solubility has been identified as the determining factor for p-type doping limits with Mg-doped GaN [63].

## 2.2 Surface segregation and pyramidal defects

To make matters worse, Mg tends to segregate on the surface of GaN [64, 65], forming localized, highly concentrated areas of Mg, which can exceed saturation faster than if the Mg were spread evenly over the surface. These highly concentrated areas can continue to build up Mg concentration to a level of approximately 1.2 monolayers, at which time the surface Mg concentration is depleted by the formation of defects [65]. These defects change the film polarity of Ga-polar films to N-polar [66]. Furthermore, Mg has been found to enhance the growth rate of GaN for certain crystallographic directions [67] and impede growth in others [68]. As a result, the formation and propagation of the defects form pyramid-shaped defects, with the tip pointing toward the [0001] direction [69]. The pyramid defects have a hexagonal base in the (0001) plane with six facets in $\{1\bar{2}13\}$ planes [61] and are shown in Figure 9. Since Mg substitutes for Ga in GaN for p-type GaN, Mg would be bonded to surrounding N atoms. Thus, $Mg_3N_2$ is a competing compound formed at high levels of Mg-doped GaN [61] and is thought to be the cause of the polarity inversion of Ga-polar films to N-polar [61]. However, it was found for MOCVD that no defects were formed if the Mg flux was lower than a Mg molar precursor ratio of 0.02 to the group III source, as seen in Figure 10, indicating this flux defines the saturation limit [65]. Above this critical flux, there is a defect-free region at the beginning of growth, while the Mg concentration is accumulated on the surface. Once the critical surface concentration is exceeded, the Mg is depleted at the surface and formed into the material through defects and the process is repeated. This results in an oscillation effect of defect concentration throughout a film, as shown in Figure 11 [65]. The oscillation of defect concentration is a result of the cycle of buildup of Mg on the

surface in the absence of defects, then depletion of the surface Mg through defect formation.

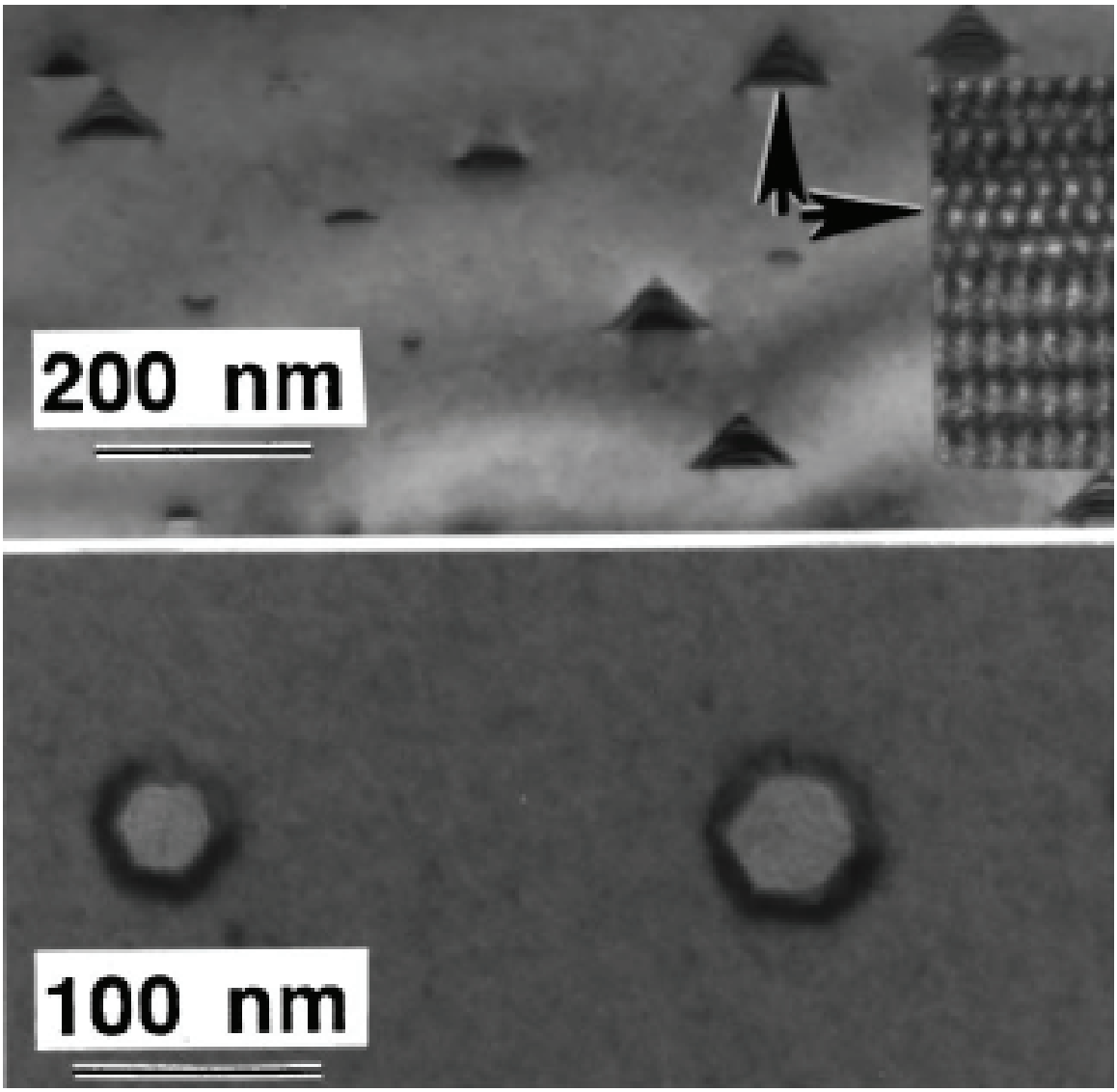


Figure 9: Cross section view of defects on top and surface view of defects on bottom [68].

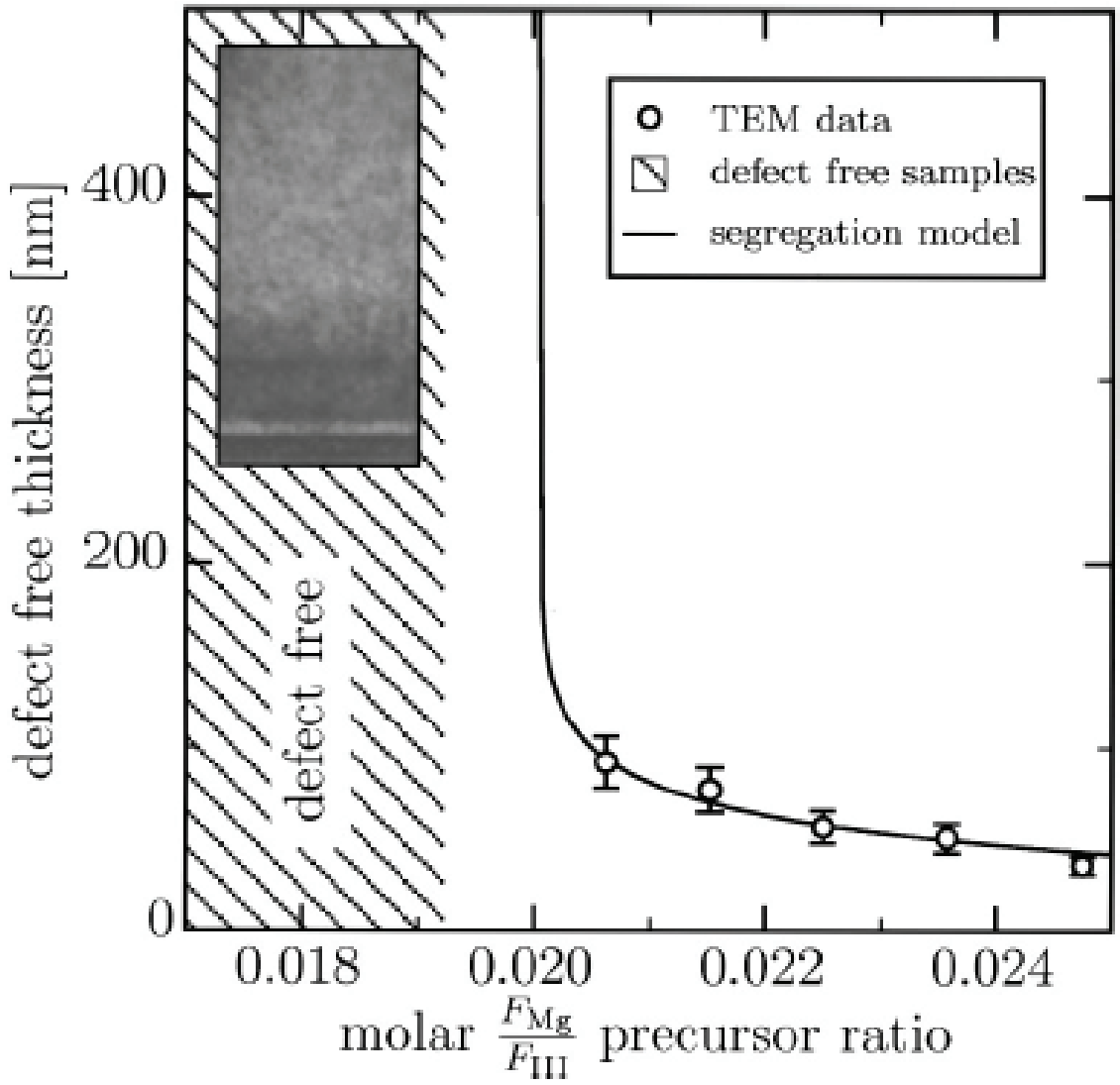


Figure 10: Response of defect-free thickness to precursor ratio, showing complete defect-free growth for a molar precursor ratio less than 0.02 [65].

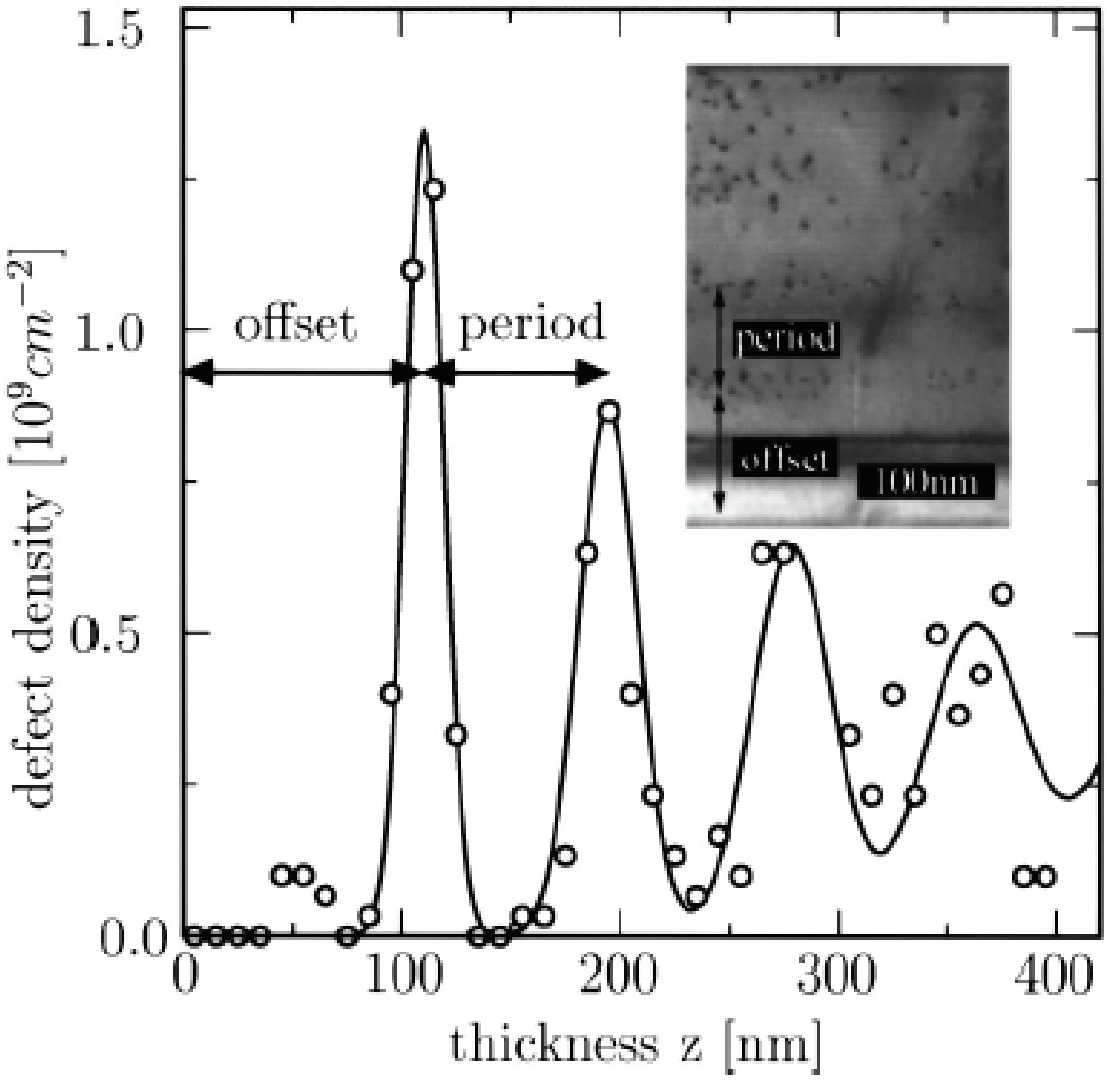

Figure 11: Relationship of defect density and thickness, showing an initial defect-free offset and following oscillation with period [65].

## 2.3 Memory effect

Mg incorporation also exhibits a delay upon Mg source exposure followed by a persistence upon Mg source removal, known as the memory effect [16, 17]. Mg memory effects describe the undesirable tendency of Mg to accumulate on the walls of the growth environment. The first study of Mg memory effects with GaN was done in 1994 [17] and

was motivated by similar observations of Mg in GaAs [70]. It was found that the steady-state Mg concentration would be reached in a film only after sufficient Mg had preferentially accumulated onto the walls of the growth chamber. The delay in steady-state Mg incorporation could be circumvented by moving the substrate to a "waiting position" out of the path of source gasses, thus interrupting growth, then turning on the Mg source and allowing Mg to accumulate onto the walls before resuming growth, as shown in Figure 12. Conversely, when the Mg source is turned off, the accumulated Mg slowly desorbs from the chamber walls to create an unintentional background concentration of Mg. However, it has been suggested that this delay in incorporation is due to Mg surface segregation instead of wall adsorption [65], though it is not explained why the growth interruption solves the observed memory effect. Finally, both the pyramidal defects and memory effects are reported overwhelmingly more often for CVD than for MBE. However, the few reports of the memory effect in MBE are a result of heated components such as the shutter, which was found to re-evaporate Mg when the Mg source shutter was closed and heated [29]. Therefore, the larger memory effect with CVD is probably a result of the colder wall system that MBE uses, which condenses Mg and doesn't allow it to re-evaporate. Nevertheless, the re-evaporation of Mg from heated components remains an issue to be resolved for MBE.

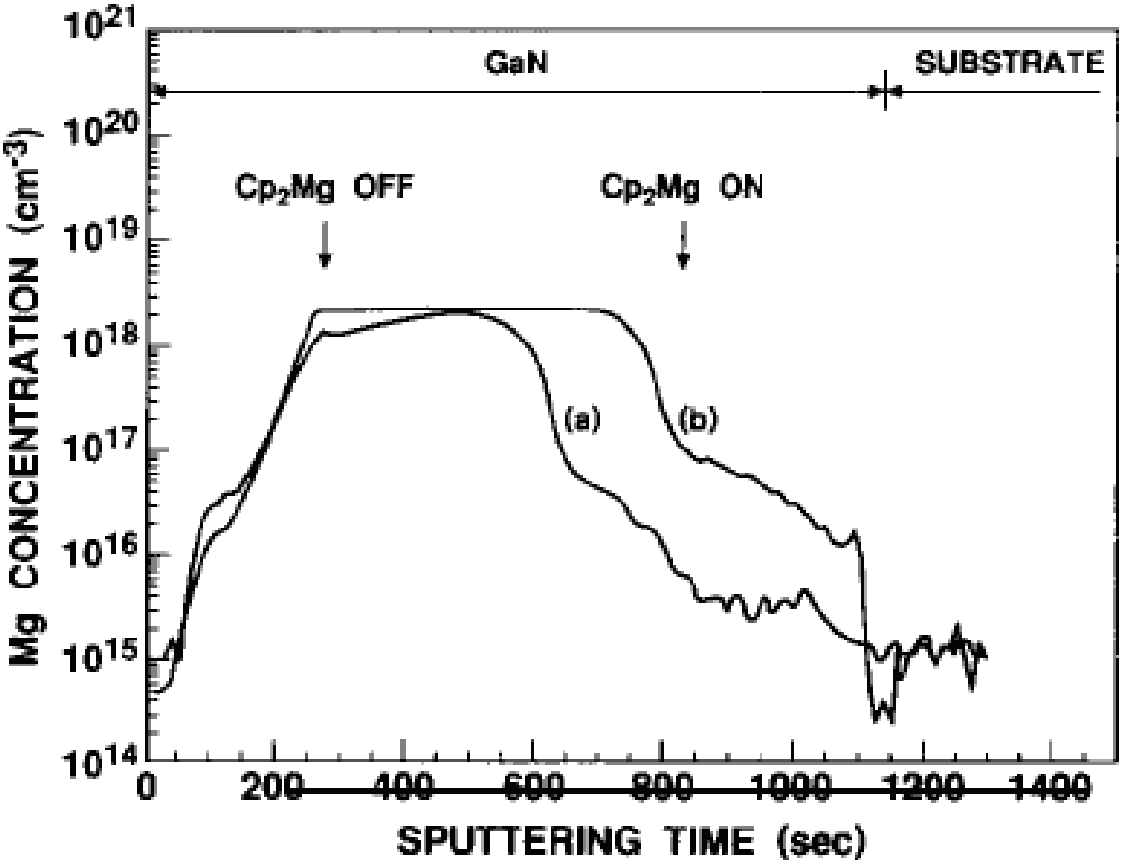

Figure 12: (a) Demonstrated memory effect of Mg-doped GaN, with (b) interruption solution showing no delay in Mg incorporation [17].

## 2.4 High vapor pressure

Conversely, control of Mg as a dopant source in MBE can be especially difficult because of the ultra-high vacuum environment. The temperature needed for dopant-level vapor pressures of Mg is relatively low [15] and the vapor pressure curve has a large slope at these low temperatures, as seen in Figure 13. As a result of this slope, the Mg flux is highly sensitive to thermal fluctuations. Because conventional effusion cells use thermal energy to control the flux of Mg, they have a limited flux control because of this steep vapor pressure curve and also suffer from large fluctuations in Mg flux as a result of small fluctuations in temperature. Conventional effusion cells can also demonstrate

sluggish response to temperature changes, because of the long thermal time constants associated with temperature changes of the cell, making controllable changes in the flux of the Mg dopant a slow process.

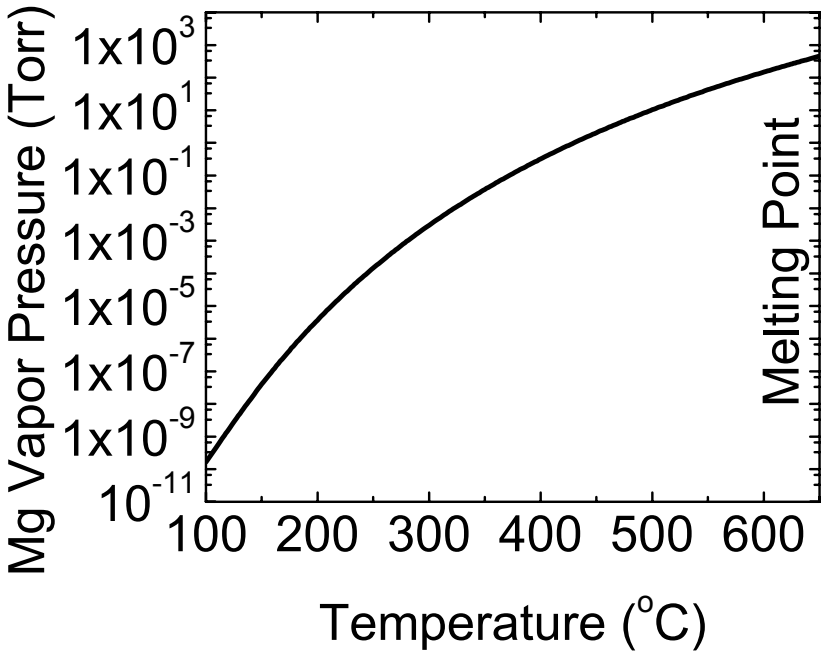


Figure 13: Vapor pressure curve for Mg [71], which shows a steep slope for low temperature, which are used for dopant-level fluxes.

## 2.5 Low sticking coefficient

The sticking coefficient of a particle onto a surface is a number from 0 to 1 representing the probability that the particle will stay on the surface. The necessary Mg flux for a specific concentration is determined by the sticking coefficient of Mg on GaN. The issue of a low sticking coefficient of Mg on GaN is not covered well in the literature, so it will be briefly outlined here. The equation [72]

$$F = \frac{P(T)a}{\pi L^2\sqrt{2\pi mkT}} = \frac{N_A P(T)a}{\pi L^2\sqrt{2\pi\frac{M}{1000}RT}}$$

$$= \frac{\left[\frac{6.022\times10^{23}}{\text{mol}}\right]\left[\frac{133.3\text{kg}}{\text{torr}\cdot\text{m}\cdot\text{s}^2}\right]\left[P(T)\text{torr}\right]\left[\pi(r)^2\,\text{cm}^2\right]}{\left[\frac{10000\text{cm}^2}{\text{m}^2}\right]\left[\pi(L)^2\,\text{cm}^2\right]\sqrt{\left[\frac{2\pi(8.314)\text{m}^2\cdot\text{kg}}{\text{s}^2\cdot\text{mol}\cdot\text{K}}\right]\left[\frac{\text{kg}}{1000\text{g}}\right]\left[M\frac{\text{g}}{\text{mol}}\right]\left[T\text{K}\right]}} \qquad (5)$$

$$= \frac{r^2}{L^2}\frac{3.513\times10^{22}P(T)}{\sqrt{MT}}\frac{1}{\text{cm}^2\text{s}}$$

gives the flux from an effusion cell, where $N_A$ is Avogadro's constant in $\text{mol}^{-1}$, $P(T)$ is the equilibrium pressure in Torr at the cell temperature, $T$, in K, "$a$" is the area of the effusion cell aperture in $\text{cm}^2$, $r$ is the radius of the effusion cell aperture in cm, $L$ is the distance from the effusion cell aperture to the substrate in cm, $M$ is the molecular mass of the evaporated species in g/mol and $R$ is the molar gas constant in J/mol/K (the units were included in the equation for assurance of unit balance). The final product given for this equation can be verified without the geometric adjustments by the equation given for the evaporation rate of a liquid or solid surface [73]. When divided by a growth rate, $\dot{G}$ in units of cm/s, the concentration of a dopant with unity sticking coefficient is given by

$$N_i = \frac{r^2}{L^2}\frac{3.513\times10^{22}P(T)}{\dot{G}\sqrt{MT}}\,\text{cm}^{-3}. \qquad (6)$$

Therefore, to find the sticking coefficient, S, the actual dopant concentration, N, can be divided by $N_i$, or $S = N/N_i$. Approximating r as 0.6 cm [74] and L as 13.4 cm and using a paper that includes the remaining necessary data as an example, where $\dot{G} = 8.33 \times 10^{-9}$ cm/s, $T_{Mg} = 625$ K and $N \approx 8 \times 10^{17}$ at/cm$^3$ [75], a representative sticking coefficient for Mg on GaN can be found. At this Mg temperature, the equilibrium vapor pressure is approximately $3 \times 10^{-4}$ Torr [71]. Using this data, a sticking coefficient is found with

$$S = \frac{N}{N_i} = \frac{N}{\frac{r^2}{L^2}\frac{3.513\times10^{22}\,P(T)}{\dot{G}\sqrt{MT}}} = \frac{8\times10^{17}}{\frac{0.6^2}{13.4^2}\frac{3.513\times10^{22}\left(3\times10^{-4}\right)}{8.33\times10^{-9}\sqrt{(24.3)(625)}}} \qquad (7)$$

$$= \frac{8\times10^{17}}{2.06\times10^{22}} = 3.88\times10^{-5}.$$

Although this result is valid only for the MBE growth of Mg-doped GaN with solid source Mg as the evaporated dopant, it clearly shows the extremely low sticking coefficient of Mg on GaN. Furthermore, this result is contradictory to reports of a high sticking coefficient in metalorganic CVD (MOCVD) [17].

2.6 High ionization energy

Once all of the above issues of incorporating Mg into the GaN lattice have been successfully overcome, there remains the issue of freeing the hole, or activating the Mg acceptor. The ionization energy (also called the binding or activation energy) is the minimum amount of energy required to remove the most loosely held electron of an atom or ion. For a donor, it is the energy needed to move an electron from the impurity state associated with the donor to the conduction band and for an acceptor, it is the energy needed to move a hole from the impurity state associated with the acceptor to the valance band (or, more precisely, to move an electron from the valance band to the impurity state). In order for an impurity to be useful as a dopant, the ionization energy must be attainable at the operational temperature. At room temperature, the impurity ionization energy has to be comparable to the thermal energy, kT = 26meV, or less for complete ionization. If the dopant results in a much deeper impurity state than the available thermal energy, the impurity will likely remain unionized, even if the dopant is perfectly soluble and perfectly incorporated into the lattice. Using the dielectric constant and effective hole mass for GaN as $K_r$ = 9.5 [44] and $m_h^*/m_0$ = 0.95 to 1.1 [46], respectively,

the acceptor binding energy can be estimated based on that for a hydrogen atom using [43]

$$E_A \approx \frac{13.6}{K_r^2}\frac{m_h^*}{m_0} = 0.143 \text{ to } 0.166 \text{ eV}. \quad (8)$$

Previous studies have found activation energies between 112 and 190 meV [76-80], with the majority being around 160 to 170 meV [77-80] and in good agreement with the above estimate. This results in an approximately 1% activation of Mg in GaN at room temperature [78] and would require an operational temperature over 1650° C to fully ionize the acceptors. The activation energy of Mg acceptors is even deeper for aluminum gallium nitride (AlGaN) alloys [81]. Recently, activation as high as 10% has been reported for GaN using a high growth temperature with high Ga and Mg fluxes [82], but this result has not been repeated. The limitation of low acceptor activation is further complicated by a high level of background electron concentration [10]. The native defects of GaN are donors that have a theoretical energy level of 30 meV using $m_e^*/m_0$ = 0.2 [44] and an empirically measured value of 25.2 meV [83]. Therefore, it is much easier to activate these donors than it is to activate the Mg acceptors because of the heavy hole mass and nearly all of these donors will be activated at room temperature. Figure 14 shows the energy band diagram for GaN, including the donor and acceptor levels, with thermal energy for comparison. The native donor concentration in GaN is approximately $4 \times 10^{16}$ $cm^{-3}$ [84] and sets a lower limit on hole concentration as a result of automatic compensation.

## 2.7 Unintentional dopants

Unintentional dopants are introduced from various sources and also limit the amount of desirable dopants that can be incorporated into the material. Because ideal

crystal growth conditions are not easily attainable, ubiquitous residual impurities such as hydrogen and oxygen are one source of these unintentional dopants. Another source of unintentional doping comes from equipment used to grow the crystal, such as outgassing from certain types of heaters and fixtures [85]. However, for high-pressure growth systems, such as CVD, these contaminants are unavoidable. Hydrogen is often used as a carrier gas for the sources in CVD systems and forms a stable bond with Mg dopants in GaN, passivating the acceptor [86]. Furthermore, Figure 15 shows that as GaN is doped more as p-type, therefore lowering the Fermi energy, H is incorporated more readily [11]. Therefore, as more Mg is incorporated successfully into the lattice without exceeding the solubility limit, more H is also incorporated to passivate the Mg. Fortunately, however, the Mg can later be activated by thermally liberating the H in an inert gas environment [87], which actually helps to keep the Fermi level near mid-gap so more Mg can be successfully incorporated and activated later [11, 86]. However, the incorporation of oxygen has been found to form a donor with an energy level of 78 meV [88] and thus will compensate the hole concentration. Furthermore, it was suggested that oxygen is the source of native donors in GaN, instead of nitrogen vacancies [11]. Alternatively, high-vacuum growth systems that do not use hydrogen, such as MBE, do not suffer from hydrogen or oxygen compensation as heavily as other systems and can therefore achieve *in situ* p-type material.

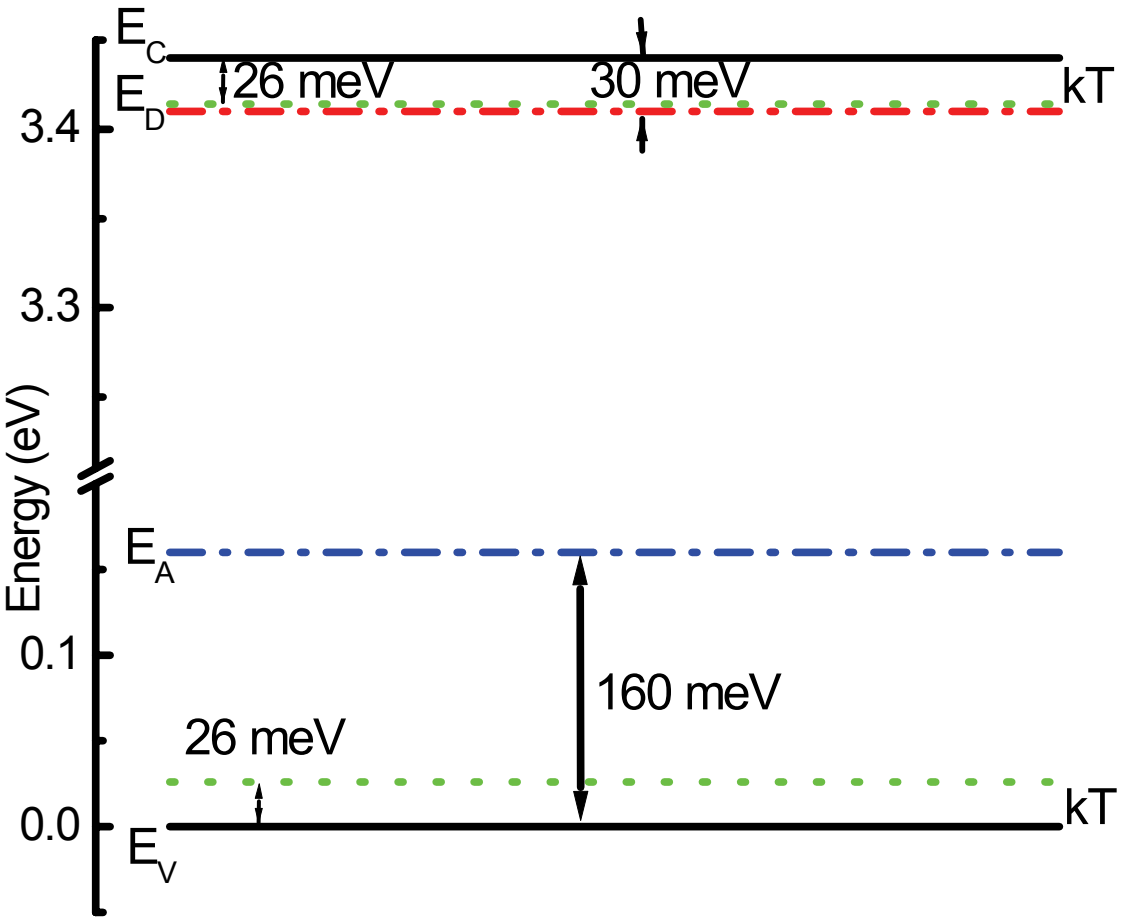


Figure 14: Energy diagram of GaN showing energy levels of donors and acceptors and the thermal energy at room temperature (color online).

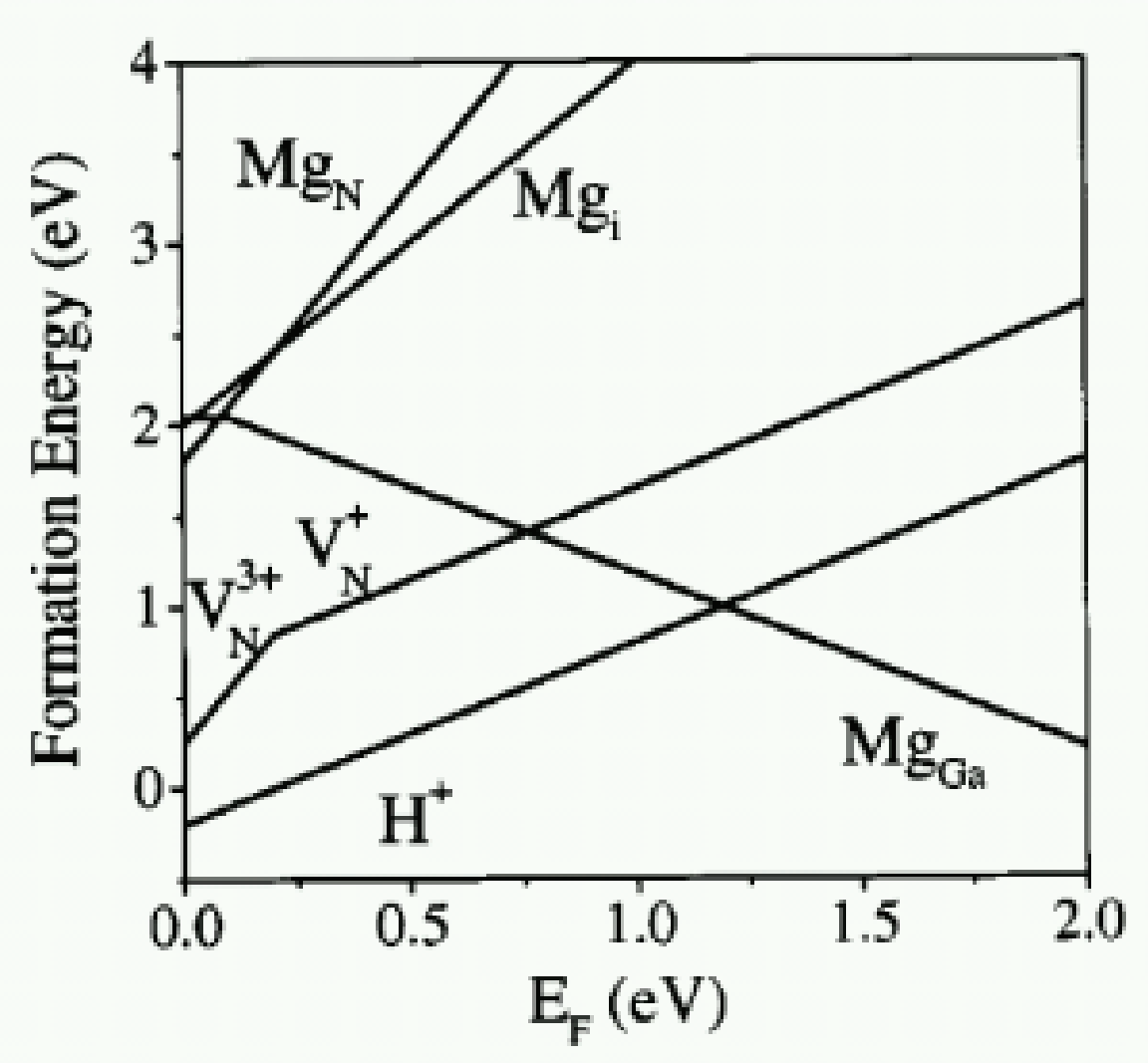


Figure 15: Formation energy as a function of Fermi level for Mg in different configurations (Ga-substitutional, N-substitutional and interstitial configuration). Vacancies and interstitial H are also included [11].

## 2.8 Compensating defects

As mentioned above and demonstrated in Figure 15, doping produces more free carriers and alters the Fermi energy, making the creation of oppositely charged native defects easier. This effect creates an upper limit on the possible concentration of free carriers generated by doping. Because these defects are oppositely charged, the

formation of these compensating defects involves charge transfer from the dopant to the defects (or vice-versa), which negates the effect of the intentional dopant. Figure 15 illustrates how Mg-doped GaN suffers from this limitation [11]. For a low Fermi energy, $E_f$, (indicating p-type doping) the formation energy for Mg to substitute for Ga as an acceptor becomes larger than defects such as Mg interstitial, accompanying N vacancy (double donor), or even a Mg N-substitutional (single donor). These defects can cause compensation to the acceptor doping, limiting the concentration of hole carriers. Indeed, it has been observed that hole concentration decreases with increased Mg flux past a critical Mg flux [89, 90]. Relating this back to the solubility limit, the $Mg_3N_2$ competing phase should not contribute either way to the doping level, although formation of the compound does limit the amount of useful Mg that can be incorporated into the Ga sites and effective hole carrier concentration is therefore reduced. However, it has been observed that the solubility limit is coincident with the formation of compensating defects and the $Mg_3N_2$ compound [61], which suggests the $Mg_3N_2$ defects may play some role as compensating donors.

## 2.9 Current status

Despite the plethora of complications associated with Mg-doped GaN, current state-of-the-art reports show promising results and give a reference for comparison. Mg incorporation as determined by secondary ion mass spectroscopy (SIMS) has been reported as high as $8 \times 10^{20}$ cm$^{-3}$ for MOCVD [76], and $3.5 \times 10^{20}$ cm$^{-3}$ for MBE [29]. However, above approximately $2 - 3.5 \times 10^{20}$ cm$^{-3}$, the Mg incorporation begins to decrease with increased Mg flux [29]. M-plane $(10\bar{1}0)$ oriented substrates have been used to achieve hole concentration as high as $p = 7.2 \times 10^{18}$ cm$^{-3}$, though the material was

highly resistive [91]. Current electrical characterization for state-of-the-art films grown on c-plane substrates are shown in Table 2. Reasonably high hole carrier concentrations range from $1 - 3 \times 10^{20}$ $cm^{-3}$. However, hole concentrations have been reported as high as $6 - 7 \times 10^{20}$ $cm^{-3}$, though the material was either metastable and reduced upon annealing, and/or not repeatable.

Table 2: Electrical characteristics of state-of-the-art Mg-doped GaN on c-plane substrates. *The hole concentration reported was metastable, and was reduced by half upon annealing

| Hole concentration ($10^{18}$ $cm^{-3}$) | 3 | 3 | 6* | 7 |
|---|---|---|---|---|
| Mobility (cm2V-1s-1) | 9 | 2 | 0.3 | 0.3 |
| Resistivity (Ω·cm) | .23 | 1.04 | 3.47 | 2.97 |
| Reference | [84] | [82] | [92] | [93] |

## 2.10 Summary

P-type doping of GaN, specifically with Mg [94], has been an integral part in the development of devices with this material system. The successful implementation of GaN optoelectronic and electronic devices, such as ultraviolet light emitting diodes and high-speed/high-power heterojunction bipolar transistors, depends on the effective use of Mg doping for p-type films. However, Mg doping of GaN is not a trivial task and is riddled with several complications. For example, changing the III-V ratio or substrate temperature, even slightly, changes the resulting Mg and/or hole concentration [21, 95]. This effect is mostly due to changes in the probability of Mg substituting for Ga and thus the solubility, surface accumulation and sticking coefficient will all determine the resulting change in carrier concentration and polarity. The difficulties of Mg doping GaN are vast and multi-faceted, including the following obstacles:

- A low solubility of Mg into GaN [11]
- A tendency of Mg to accumulate and segregate at surfaces [18]
- Memory effects of Mg in a growth chamber [16, 17]
- A high vapor pressure of Mg at low temperatures [15]
- A low sticking coefficient of Mg on GaN
- A deep ionization energy of Mg acceptors in GaN [19]
- Unintentional hydrogen and oxygen doping [86, 88]
- A significant compensation of Mg acceptors at high dopant concentrations [11]

Some of the listed Mg complications are more adverse for certain growth techniques than for others. For example, the Mg vapor pressure is more of a problem with high-vacuum systems such as MBE than for lower vacuum systems such as MOCVD. Conversely, the excessive substrate temperature of MOCVD, often above 900º C, results in poor Mg incorporation for the same reason: the high Mg vapor pressure at those temperatures. Additionally, the Mg memory effect is reported more for low vacuum systems such as CVD rather than high-vacuum systems such as MBE. However, complications such as low Mg solubility, deep Mg ionization energy and compensation at high Mg concentrations affect all growth systems. Therefore, regardless of the growth technique, there are lower and upper limitations to Mg doping of GaN, as there are with the doping of other material systems. The resulting challenge is to standardize the growth of Mg-doped GaN within the window of successful growth conditions with improved growth control. This can be done with new equipment, characterization and growth techniques. Once this challenge is overcome, Mg-doped GaN will be easier to

create, more repeatable, more reliable, and therefore more applicable to various needs requiring this promising material.

# CHAPTER 3: MG SOURCE WITH A VALVED THERMAL TIP

Solutions to the challenges of doping GaN with Mg do not usually come without a trade-off because of the coupling of parameters. For example, maximizing incorporation using conventional effusion cells by increasing cell temperature results in a large background concentration of Mg and an increase in memory effects, which make abrupt concentration changes difficult. Therefore, minimizing the required magnesium flux, thus minimizing memory effects [16, 17], is an important consideration. Additionally, MBE uses shutters that are relatively cold when open and heat up when closed. Mg can condense on the shutters during open cycles and re-evaporate, desorb and re-deposit on the substrate when the shutters close. A new source for Mg doping of GaN with MBE was studied to address the issues of high Mg vapor pressure, Mg memory effects and low Mg sticking coefficient. Additionally, a new doping method was explored with the new source to improve the magnesium incorporation by a factor of 10, while maintaining constant Mg flux. The new source allows enhanced flux control, facilitating graded dopant layers such as that used in graded base heterojunction bipolar transistors [96] .

## 3.1 Flux energetics

The thermal energy of the molecular beam from an effusion cell is a direct function of the thermal energy that is used to control the flux from the cell. The desired flux determines the required temperature of the cell and likewise, the required temperature of the cell fixes the thermal energy of the molecular beam impingent on the growth surface. Since it is possible that the small sticking coefficient observed for Mg on GaN [18] could partially be a result of the low thermal energy of the molecular beam,

which is a direct result of the low temperature required for the dopant level flux from a conventional effusion cell, it may be beneficial to have a more thermally energetic species of Mg impingent on the growth surface. However, it is almost impossible to address these issues with a conventional effusion cell, because molecular beam flux and energetics are coupled together through the cell temperature.

A valved dopant source can control beam flux independently of beam energetics while providing excellent stability, control and reproducibility, which are all difficult to obtain with a conventional effusion cell. Additionally, the valve offers the advantage of eliminating the need for a temperature variable shutter, which was found to be a cause of Mg memory effects in MBE [29]. A valved cracker source has an evaporation region, similar to a conventional effusion cell, which produces a flux that is attenuated by a needle valve to control flux independently of evaporator temperature. A cracker also has a thermal energizing tip that can further energize the flux as it enters the growth chamber. The cracker tip determines the energetics of the beam, while the valve restricts the flux of the source from the evaporator region, thus controlling both the flux and the thermal energy of the molecular beam. It should be noted, however, that beam flux control can be difficult if the temperature of the evaporator is raised too high for the valve to adequately attenuate the flux to a reasonable dopant level, which is merely a limitation depending on the precision of the valve. In the case of selecting a cracker for Mg, it is necessary to have a valve made of a material that will not alloy to Mg to avoid valve position freezing. Thus, an all PBN valve design is highly preferred. This proposed valved dopant source with thermal energizing tip is more suitable than a conventional

effusion cell for Mg-doped GaN because of the ability to achieve greater stability, rapid and accurate flux control and reproducibility of beam flux and energetics.

## 3.2 Model of valved source

The Veeco 200cc Corrosive Series Valved Cracker, shown in Figure 16, has characteristics of an all-PBN valve design, which will not alloy with Mg and an independent temperature control of the bulk material verses thermal tip. Therefore, this device was chosen as the valved dopant source to meet the above requirements. A model was needed to characterize the operation of this device, and because the operation of the cracker valve is similar to a needle valve, the beam equivalent pressure (BEP) was modeled using the conductance theory of an ideal needle valve. The relationship among BEP, conductance and area is given by

$$\text{BEP} \propto C \propto A = \pi\left(r_0^2 - r_i^2\right) = P2 - \pi r_i^2, \tag{9}$$

where C is conductance, A is area, $r_0$ is the outer radius of the needle valve, $r_i$ is the inner radius of the needle valve and P2 is a fitting parameter, equal to the area of a circle with radius $r_0$, As shown in this equation, the BEP is proportional to conductance and the conductance through a needle valve is proportional to the area of opening, as shown in Figure 17b. The area of opening through the needle valve can be modeled as a circle with radius $r_0$, with an inner circle of radius $r_i$ subtracted. The inner circle radius expands and contracts based on the position of the needle valve. The model

$$\text{BEP} = P1\left(P2 - \pi\left(x - P3\right)^2\right) \tag{10}$$

uses x as the valve position and P1, P2 and P3 as fitting parameters. The equation was fit to experimental data, resulting in

$$\text{BEP} = 4.2 \times 10^{-4}\left(2.08 \times 10^5 - \pi\left(x - 290\right)^2\right)[\text{Torr}],\ x > 48\ \text{mils}, \tag{11}$$

with x in units of mils. There was a region of background limited conduction also observed, which was modeled with the exponential function

$$\mathrm{BEP} = 0.172 \times \mathrm{e}^{\frac{x}{11.287}} \text{ [Torr]}, x < 48 \text{ mils}. \quad (12)$$

The two curve fits are plotted in Figure 18 and are compared to experimental data. The boundary between these to regions was at a valve position of approximately 48 mils, though the temperature of the bulk evaporator material (350° C in this particular case) determines the valve position of this boundary between the background limited flux and conduction limited flux. Flux measurements from the cracker source varied by less than 10% in the conduction-limited regime, allowing good reproducibility. These equations were derived and fit to experimental data to characterize the cracker under the given growth conditions and demonstrate the controllability of the cracker source.

Figure 16: Veeco MBE corrosive series valved cracker (color online) [97].

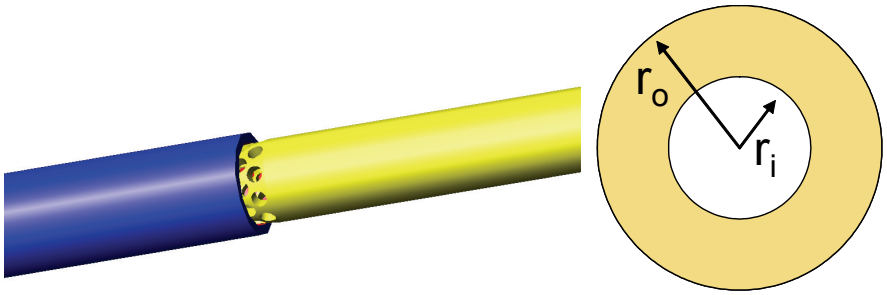


(a) (b)

Figure 17: Model of valved Mg source as needle valve (a) side view and (b) top view (color online).

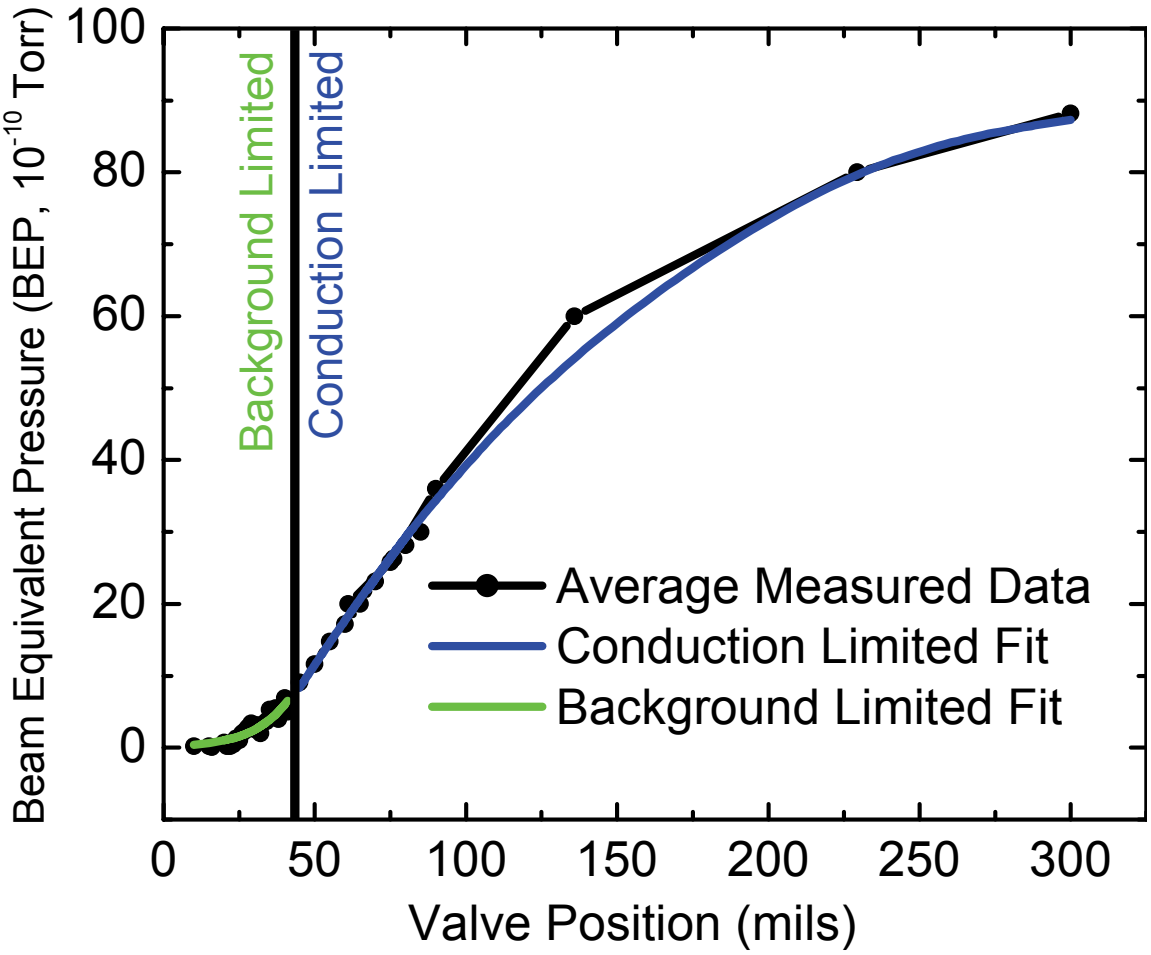


Figure 18: Model of cracker valve in background and conduction limited regime plotted with measured flux data. The transition point is at a valve position of approximately 48 mils and is determined by the bulk evaporator temperature (color online).

## 3.3 Growth conditions

The Mg cracker was used in the previously described MBE system and the valve position, evaporator temperature and thermal tip temperature were all controlled by Veeco controllers. The cracker evaporator temperature remained at 350° C, while the thermal tip was set to either 625° C or 900° C for experiments. Tantalum-backed sapphire substrates were prepared for GaN growth according to Appendix A. The samples were indium bonded to a silicon wafer to secure them in the vacuum chamber sample block. A nitrogen flow rate of 0.35 sccm was used for some Mg-doped GaN films, while most used a nitrogen flow rate of 0.5 sccm for faster growth, with a growth rate of approximately 0.45 μm per h. Following nitridation and the AlN buffer layer, the substrate temperature was reduced to 550° C and the Mg-doped GaN experiments were grown on the AlN layer.

The effect of the thermal tip was tested by growing two stepped Mg-doped profiles at a thermal tip temperature of 625° C (below the melting point of Mg, 650° C [15]) and 900° C (above the melting point of Mg). All other variables in the experiment were kept constant between the two samples and during the growths, including the Ga flux, Mg flux at each step, N-flow-rate, rf power and substrate temperature. The stepped Mg-doped profile was characterized by seven Mg-doped regions, grown for 10 min each at constant fluxes, separated by 10-min growths of undoped GaN. The Mg flux was increased systematically for these steps, from $1 \times 10^{-10}$ to $3 \times 10^{-9}$ Torr, BEP. SIMS was

performed on the two samples according to appendix D.1, with the results shown in Figure 19.

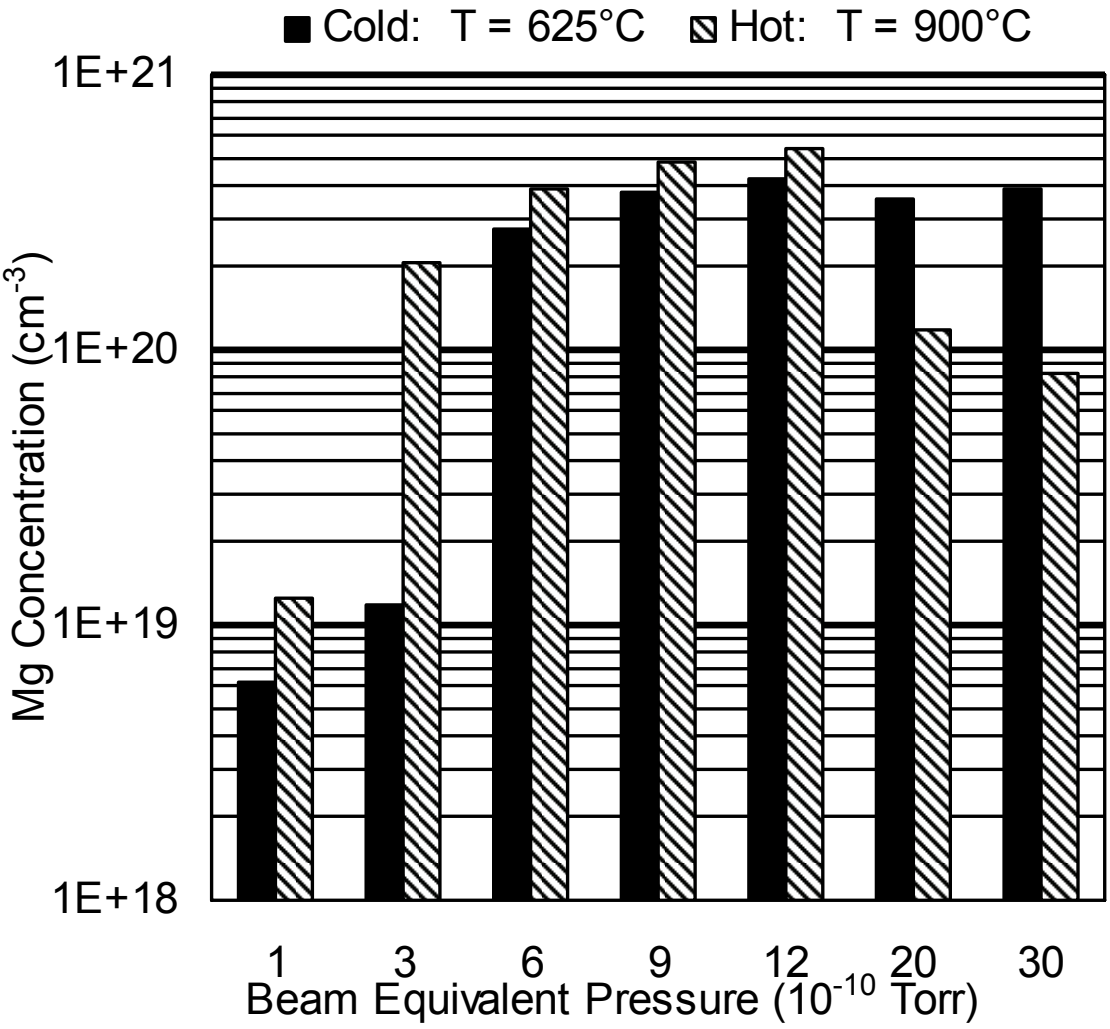


Figure 19: SIMS data from a Mg-step profile for cold and hot cracker, showing enhanced sticking coefficient and an order of magnitude increase in Mg incorporation for same BEP of $3 \times 10^{-10}$ Torr from cold cracker to hot cracker. Also shown is the faster rise of incorporation at low Mg BEP, as well as a faster decrease of incorporation at high Mg BEP for the hot cracker case compared to the cold cracker case.

## 3.4 Effects of thermal tip

It is apparent from Figure 19 that the change in the temperature of the cracker tip has an effect on the sticking coefficient of Mg on GaN. At a Mg BEP of $3 \times 10^{-10}$ Torr, the incorporation for the hot cracker is over an order of magnitude greater than the cold cracker. The hot cracker also shows sustained higher Mg incorporation around the saturation point, incorporating 30% more Mg than the cold cracker [29]. Finally, the hot cracker drops off from the saturation peak faster than the cold cracker as Mg flux is increased. These three different characteristics of Mg incorporation between the hot and cold cracker tips suggest a shift in the saturation point toward a lower flux as the thermal energetics of the beam are increased. This result appears to indicate that the sticking coefficient is enhanced with increasing beam thermal energy, thus enhancing the incorporation of a fixed Mg flux with more thermal energy. Furthermore, the highest Mg incorporation was over $5 \times 10^{20}$ $cm^{-3}$, which is near the previously reported maximum value [76].

## 3.5 Valve control capabilities

Figure 20 shows the Mg profile from SIMS analysis of a sample grown with two steps of increasing Mg fluxes (retaining constant thermal energy) and demonstrates the enhanced control of the valved cracker. The small dip between the two peaks is a result of a thin, undoped layer of GaN. An abrupt junction between two non-zero values of Mg incorporation such as this is not possible with a conventional effusion cell. This enhanced control is significant because it demonstrates an advantage of the valved cracker's behavior with the first reported demonstration of such a profile with Mg-doped GaN. The cracker's operation is analogous to a digital-to-analog converter in an

electrical circuit, because of its exact, quantified digital input and wide-range of analog flux output. Its digital input quality allows for precise control and repeatability of valve position, while the analog flux output allows for a nearly continuous range of fluxes. This behavior gives enhanced control of Mg doping over the conventional effusion cell.

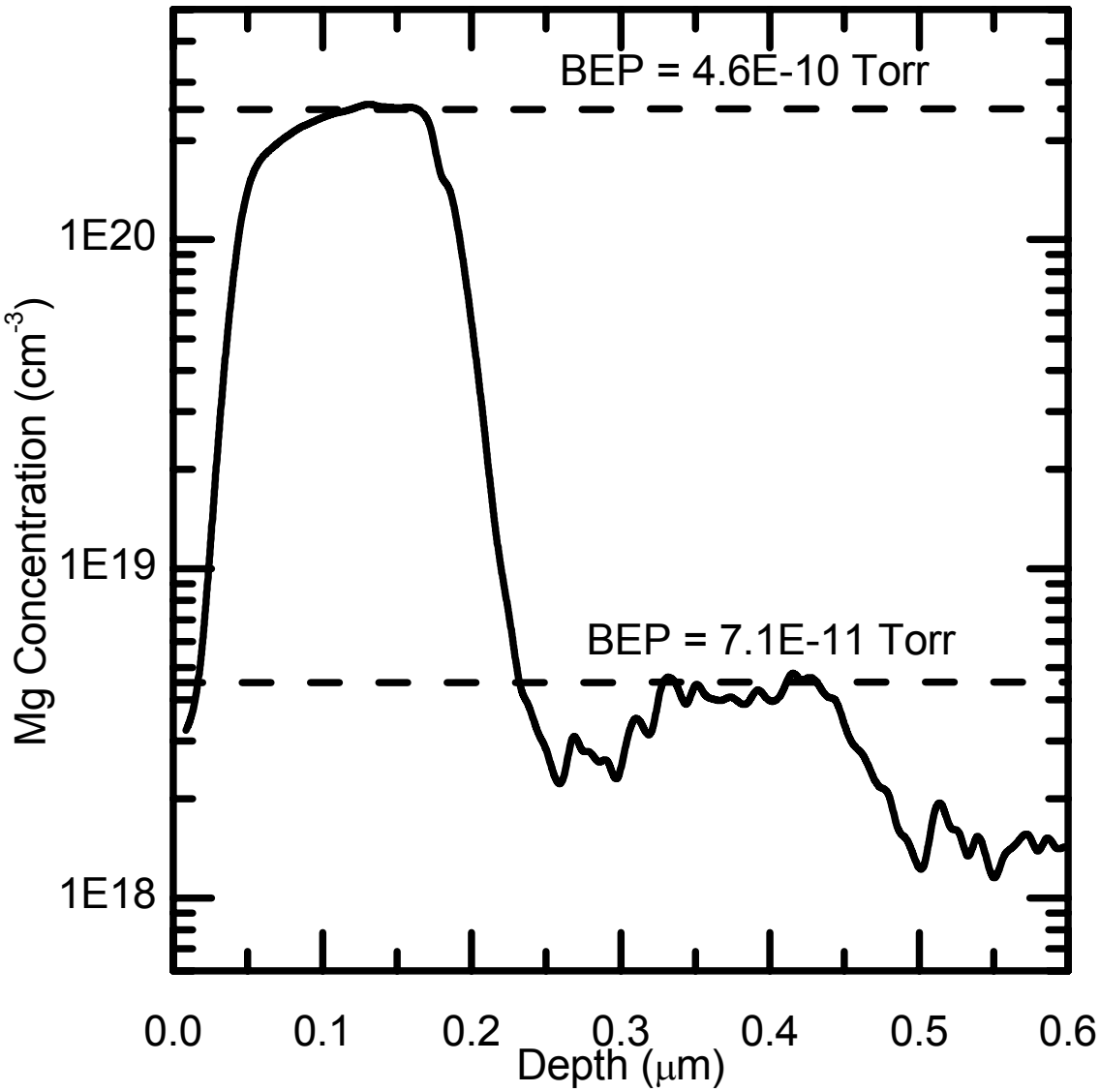


Figure 20: SIMS concentration profile shown of an abrupt Mg junction separated by a thin undoped region, demonstrating improved doping control over sluggish conventional effusion cells, which are limited by thermal time constants.

## 3.6 Mg dependence upon III – V ratio

An interesting finding during this study is the dependence of Mg incorporation on Ga flux, as shown in Figure 21. Although it is well known that more Mg is incorporated as Ga flux is decreased since there are more available sites for the Mg atoms [98], Figure 21 shows a contradiction to that theory, but only at a certain critical flux. Initially, Mg incorporation increases with Ga flux in the Ga range of $3.1 \times 10^{-7}$ down to $1.9 \times 10^{-7}$ Torr, BEP. But at approximately $1.5 \times 10^{-7}$ Torr, BEP, there is a much smaller peak than the peaks around it. After this flux, from the Ga range of $1.3 \times 10^{-7}$ to $1 \times 10^{-7}$ Torr, BEP, the Mg incorporation continues to increase with decreasing Ga flux, as expected. It is also interesting to note that the RHEED pattern changes from streaky to spotty and back to streaky in this transition. This may explain why some groups have success growing Mg-doped GaN from N-rich conditions and others have success from Ga-rich conditions: there may be more than one optimum peak for Mg incorporation over the Ga flux range.

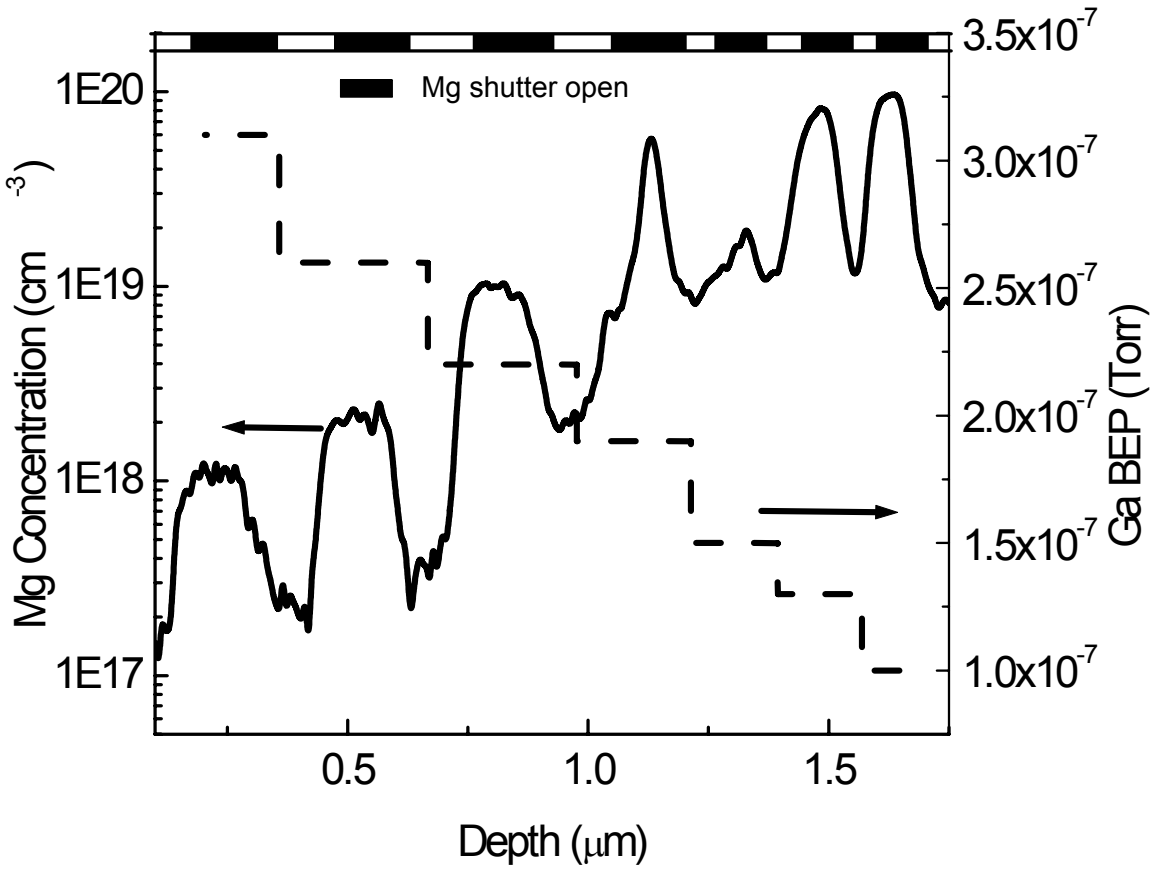

Figure 21: SIMS data showing profile of step-Mg-doped sample with constant Mg flux and changing Ga flux.

## 3.7 Summary

A valved source with an independent thermal tip used for the Mg dopant source in MBE of GaN appears promising for enhancing dopant incorporation and control compared to a conventional effusion cell. As shown, the sticking coefficient of Mg on GaN was apparently enhanced based on increased SIMS-determined Mg concentration. Dopant concentration was clearly increased by over an order of magnitude for the same Mg BEP by increasing the temperature of the thermal cracking tip. It was also shown that the cracker source can be characterized through a mathematical model to allow precise and repeatable performance for improved controllability. An abrupt profile was

demonstrated using this improved controllability. Linearly graded doping profiles can also be achieved and could be useful in future studies of graded base doping of an HBT to improve base transport times using field-assisted transport [96]. Although the Mg incorporation may depend inversely on the Ga flux, there are exceptions to this, according to observed saddle points in the Mg incorporation as the Ga flux is changed. Finding the optimal Ga flux may depend on the direction from which one approaches this saddle point (i.e., from the N-rich or Ga-rich direction). The enhanced incorporation and control of Mg-doped GaN using a valved source with a thermal tip rather than a conventional effusion cell may result in further advances to meet the needs of the wide range of GaN devices.

# CHAPTER 4: *EX SITU* RESISTIVITY ANALYSIS OF DOPING USING ED-SIMS

## 4.1 The SIMS energy distribution

The energy distribution (ED) of ions from SIMS is determined by the ionization mechanism [99, 100], primary ion chemistry[101, 102], primary ion energy [103, 104], surface atom chemistry [102-108] and surface charging effects [109]. However, when performing SIMS on a homogeneous material with a consistent primary ion beam chemistry and current, significant changes in the ED can be caused only by changes in surface charging [109]. Surface charging during SIMS can occur with highly resistive, wide band gap, or insulating material. The bombardment of charged primary ions causes charge buildup on the surface of the material since it is difficult to dissipate the charge in vacuum. Surface charge buildup in SIMS not only affects the energy distribution of the secondary ions, but also causes drastic variation in the trajectories of primary and secondary ions [109], thus influencing the secondary ion yield. The effect of surface charging on secondary ion yield has already been observed and noted for insulating films such as SiN passivation layers [110] and wide band gap materials such as GaN [111]. However, no work has been found that uses the charging phenomenon and associated secondary ion yield effects for beneficial reasons. For example, it should be possible to use SIMS to observe changes in the host atom secondary ion (HASI) ED to quantitatively optimize the conductivity of otherwise highly resistive semiconductors. The optimization could be accomplished simply by observing changes in the ED in correlation to changes in resistivity for various doping concentrations in the semiconductor. While resistivity optimization is also possible using multiple bulk samples of constant Mg-doped GaN,

this technique would allow quicker optimization by combining those multiple experiments into one single growth. This technique has been used to quantitatively optimize Mg doping of GaN. However, because of its universal applicability, this technique could theoretically be used to quantitatively optimize doping of any semiconductor.

## 4.2 Growth and analysis conditions

One cm by one cm square sapphire substrates were coated with Ta and In on the backside, and prepared for GaN growth according to Appendix A. The substrate temperature was then reduced to 550° C and the Mg-doped GaN experiments were grown on the AlN buffer layer. The previously characterized Veeco 200 cc Corrosive Series Valved Cracker was used as the Mg dopant source [21, 22, 112]. The Mg bulk evaporator and tip temperature remained constant at 330° C and 625° C, respectively and cracker valve position was used to control the Mg flux.

The SIMS instrument used was an Atomika Ion microprobe A-DIDA 3000-30, with a typical analytical chamber base pressure of $3 \times 10^{-9}$ Torr. The ion guns were mass filtered and neutral trapped using $O_2^+$ and $Cs^+$ projectile ions as the primary ion beam. It was operated at an oxygen beam potential of +15keV at normal incidence to the surface and energy of approximately +15keV at a 45° angle to the surface for cesium. The secondary ion detector consisted of a quadrupole mass spectrometer and an electron multiplier. The secondary ion current signal was set at 50 nA and electronically gated for 30% of a $200 \times 200$ $\mu m^2$ rastered area to minimize crater edge effects. SIMS depth profiles of Mg concentration in the GaN films were performed using standards measured at Evans East to quantify the Mg concentration. Energy distribution SIMS (ED-SIMS)

was performed by sputtering through the film and observing the ED of sputtered Ga HASIs. The EDs were then compared to the depth profile of Mg concentration in the GaN material. By sweeping the sample target bias potential from –20 V to +50 V, the full ED of the Ga HASIs could be observed. In both regular SIMS (used to obtain a depth profile of the Mg concentration) and ED-SIMS cases, the maximum Ga HASI count rate was obtained for a 0 V target bias potential by adjusting a compensating electron flood gun, used to neutralize any initial charging effects at the beginning of the measurement. Once determined, the electron flood gun beam conditions were kept constant at -2.5 kV and 2.5 mA for all samples and all target voltages, allowing the ED peak to shift from the initial 0 V position in the event of a conductivity change. Further details of the SIMS experiment are found in appendix D.1.

To observe the effects of exceeding the saturation limit of Mg in GaN on conductivity, a sample was grown, with Mg linearly graded from a closed valve position (0 Torr, beam equivalent pressure, BEP) to a valve position of 65 mils (approximately $1\times10^{-9}$ Torr, BEP) by increasing the valve position at a linear rate of 1 mil per min. This linear increase in valve position resulted in a Mg BEP profile following approximately the shape of the background limited portion of the flux curve in Figure 18, which is defined by equation 12 [21]. The ED of Ga HASIs versus sputter time (which corresponds to sputter depth) from the ED-SIMS analysis are shown in Figure 22. The signal for Ga at a target bias potential of 0 V is highlighted in black and the Mg concentration is aligned in white corresponding to the Ga signal at 0 V, for reference. Figure 23 shows the comparison of three distinct regions of Figure 22 in 2D for more detail.

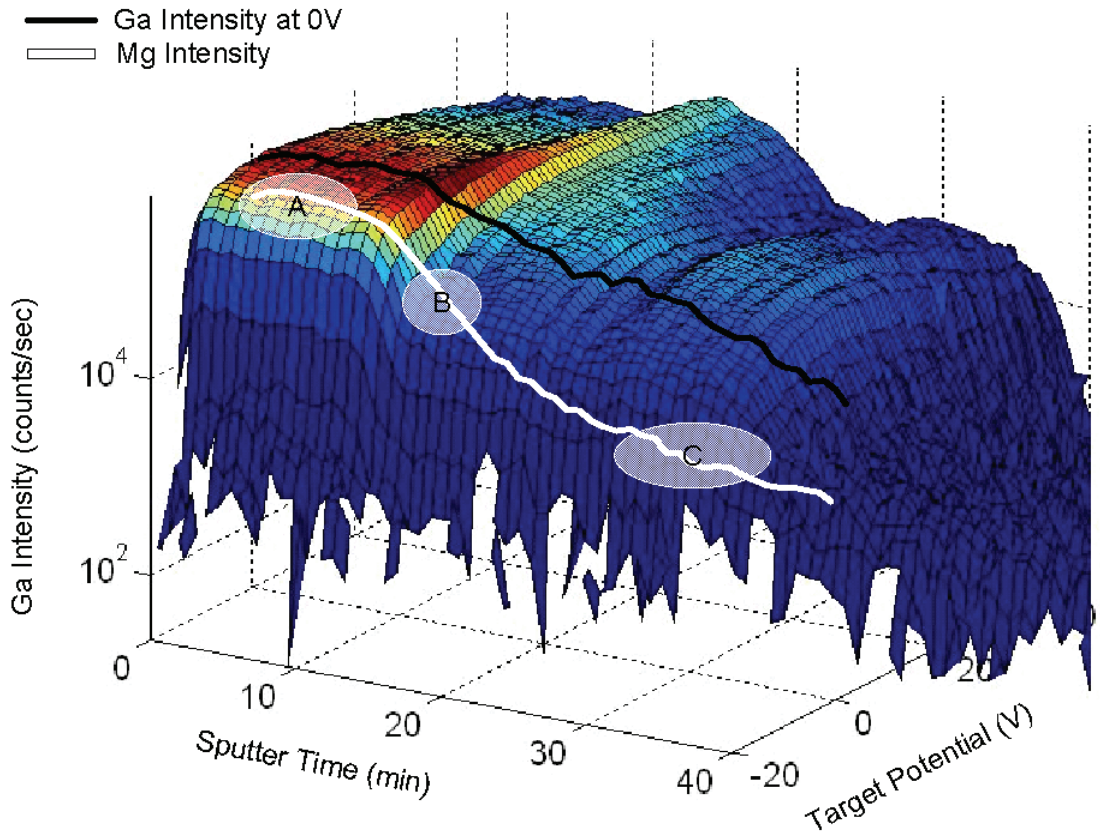


Figure 22: The energy distribution of Ga HASIs from ED-SIMS of Mg graded sample, showing energy shifts in different regions of resistivity. The black line highlights the Ga HASI intensity at a target bias potential of 0 V and the white line shows an overlay of the Mg secondary ion intensity, aligned to the Ga intensity at 0 V. The three regions of conductivity change are shown as "A," "B," and "C" (color online).

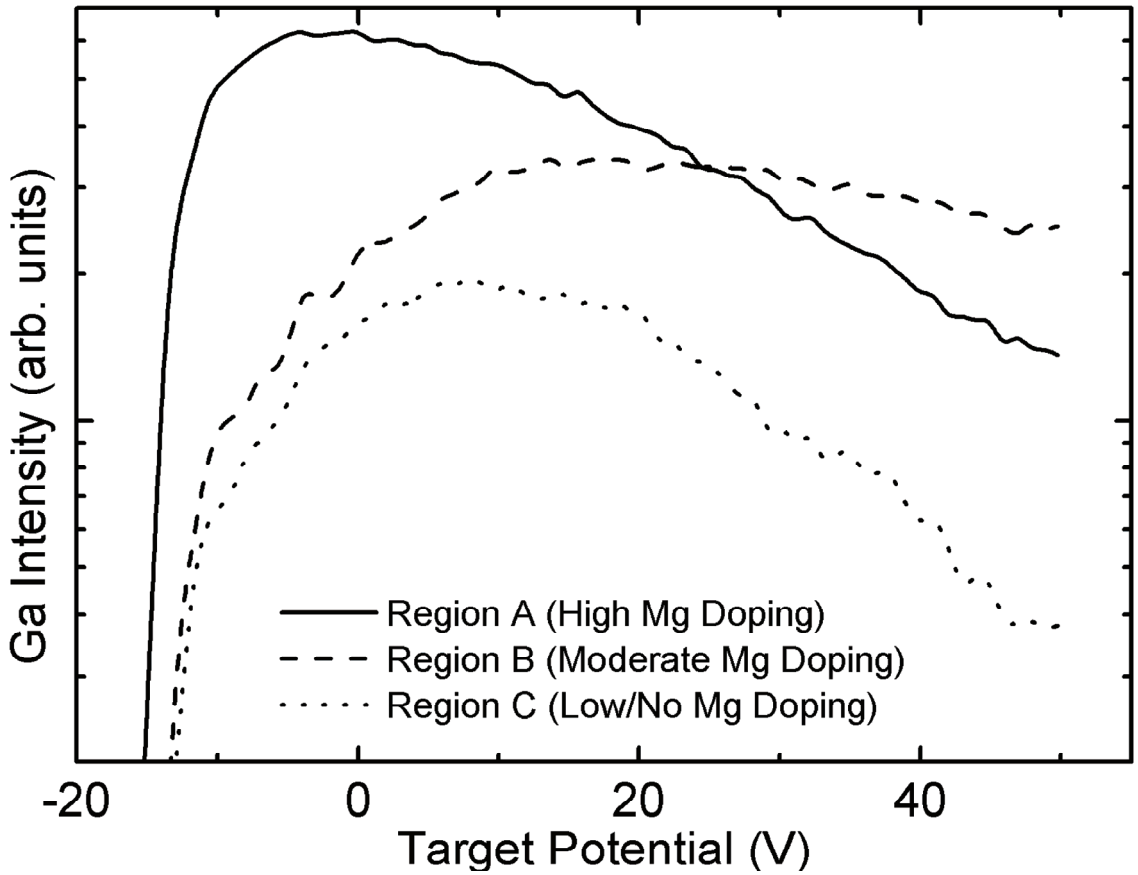


Figure 23: A reproduction of Figure 22, showing detail of the energy distribution in the regions of interest: A (High Mg doping, above critical doping level), B (Moderate Mg doping, below critical doping level) and C (Low or No Mg doping). This data shows a shift in peak energy to higher target bias potentials and changes in the shape of the distribution for the different doping regions.

To quantify valve positions and doping concentrations for the changes seen in the Ga HASI ED, a step profile of Mg doping was grown with constant Mg-doped GaN grown between layers of undoped GaN. The seven layers of constant Mg doping were grown at Mg valve positions of 22 (~$1 \times 10^{-10}$), 32 ($3 \times 10^{-10}$), 43 ($6 \times 10^{-10}$), 55 ($9 \times 10^{-10}$), 67 ($1.2 \times 10^{-9}$), 105 ($2.0 \times 10^{-9}$) and 190 ($3.0 \times 10^{-9}$) mils (Torr, BEP) with layers of undoped GaN between them, all for five min each, with all other variables remaining constant. A SIMS depth profile monitoring secondary ions for Mg, Ga at 0 V target bias

potential, Ga at +12V target bias potential and Ga at -12V target bias potential was done and is shown in Figure 24.

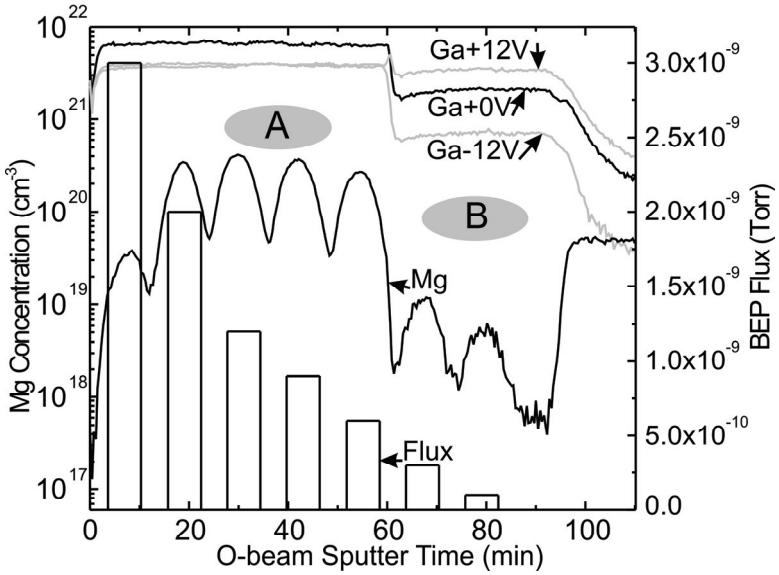


Figure 24: A O beam SIMS measurement of a step profile of Mg-doped GaN, showing regions "A" and "B" of Mg doping concentration and the effect of shifting the Ga HASI energy distribution as a result of changing from one region (conductivity) to another.

## 4.3 Cs-beam SIMS analysis

Further SIMS analysis using a $Cs^+$ primary ion source was also performed using a technique to eliminate changes in the sputter yield caused by changes in the matrix [113]. The $Cs^+$ beam SIMS analysis was done to ensure that the Mg concentration was kept low enough for all doping levels used to not cause changes in the matrix, which could modify the Mg sputter yield. As previously mentioned, changes in the chemistry of the surface atoms can lead to changes in the ED and secondary ion yield. Therefore, it is important to rule out changes in the concentration of Mg in GaN as a cause of matrix change and thus ED changes to isolate surface charging as the only contributing factor to any

observed changes in the ED. The following discussion describes how this was done and is based on the work by Thomas *et al.* [114].

The impact of $Cs^+$ primary ions on a specimen surface gives rise not only to the positive ions of the specimen, but also to positive ions of a molecular combination of the specimen and the Cs ion. For example, the $CsGa^+$ secondary ion is also generated and the signal can be modeled as [114]

$$\text{Signal}(CsGa^+) = fI_B C_{Ga} \sigma l \,, \tag{13}$$

where $f$ is an instrument transmission function, $I_B$ is the incident primary ion beam flux, $C_{Ga}$ is the concentration of Ga in the GaN matrix, $\sigma$ is the cross section of the $Cs^+ + Ga \rightarrow CsGa^+$ reaction and $l$ is the distance traveled by the Ga through the GaN matrix. It has been shown that $\sigma$ and $l$ have little variation with changes in the detected species (Ga in this case) and the matrix (GaN in this case) [115, 116]. Therefore, this signal of CsGa+ should be linearly related to the concentration of Ga [113]. Conversely, using the equation that is normally used to predict the fraction of positive monatomic species ejected from a solid [117] along with an equation to scale by the flux, the $Ga^+$ secondary ion signal can be modeled as [114]

$$\text{Signal}\left(Ga^+\right) = fNAe^{-\frac{I-\phi}{B}} = fI_B S \frac{C_{Ga}}{C_{GaN}} Ae^{-\frac{I-\phi}{B}} \,, \tag{14}$$

where N is a model of the flux of the emerging Ga, $S$ is the sputtering coefficient of the matrix, $C_{GaN}$ is the concentration of the GaN matrix, $I$ is the ionization potential of Ga, $\varphi$ is the work function of the GaN matrix and A and B are both constants for the GaN matrix.

It has been shown that $I$, $\varphi$, $A$ and $B$ vary drastically with changes in the detected species and/or the matrix [118]. While equation 13 indicates that the $CsGa^+$ signal isn't affected by matrix changes, traditional interpretation of the positive ion signal suggests that the $Ga^+$ signal would be highly affected by matrix changes. Thus, a profile comparison of the two signals described by equation 13 and equation 14 should indicate if sputter yields are being affected by matrix changes caused by changes in the Mg concentration. Therefore, each profile sample was additionally analyzed with the Cs beam to verify the Mg levels were kept low enough to avoid matrix change effects. Figure 25 shows the Cs-beam analysis of the Mg step profile sample, with the Ga and CsGa signals stable and offset by a constant throughout the film. The deviations at the extremities are due to non-steady-state surface effects [119] and matrix changes at the substrate interface. The low, noisy CsMg signal is also shown in Figure 25 for reference and the data is reproduced in Figure 26 with data from Figure 24 for clarity. From the Cs beam analysis results, it was found that the concentrations of Mg used in these experiments had no noticeable effects on the matrix according to comparison of the Ga and CsGa signal profiles, shown in Figure 25 and Figure 26, thus indicating that the levels of Mg concentration are low enough to not affect the sputter yield as a result of matrix changes for both the Cs and O beam SIMS analysis.

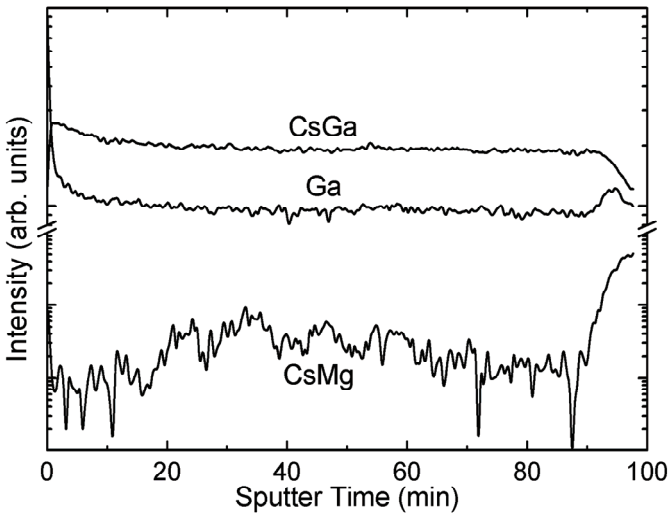


Figure 25: The SIMS data from Mg step profile sample (seen in Figure 24), using Cs beam, showing stable Ga and CsGa signals, offset by a constant throughout the bulk of the film, indicating the absence of matrix effects for the O beam analysis. Signal deviations at the extremities are due to non-steady-state surface effects [119] and matrix changes at the substrate interface. Also shown is the noisy CsMg signal for reference.

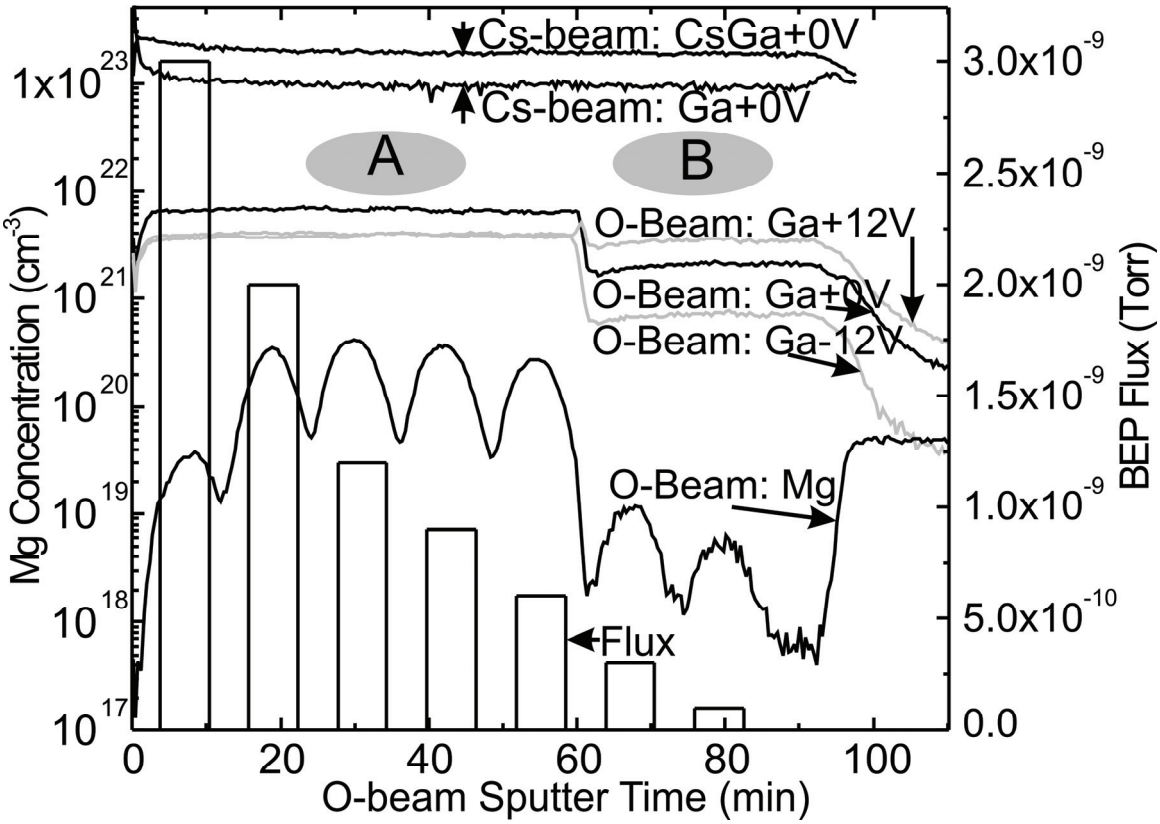


Figure 26: Combined data from Figure 24 and Figure 25, shown for clarity. A step profile of Mg-doped GaN showing regions "A" and "B" of doping Mg concentration according to O-beam SIMS and the effect of shifting the O-beam Ga HASI energy distribution as a result of changing from one region to another. Also shown are the Ga and CsGa signals from a Cs-beam SIMS scan, which are not affected by the region change, indicating the O-beam observations are not caused by a changing matrix. The Mg flux used for each doping step is shown for reference and it is important to note the concentration scale is only valid for the Mg signal.

## 4.4 Resistivity analysis

### *4.4.1 Graded Mg profile*

The only variable that can alter the shape of the ED for these experiments was surface charging effects. Therefore, the ED shifts seen in Figure 22 can be interpreted as changes in the charge state of the sample with increasing depth. These changes in charge state correspond to decreasing Mg doping and result in conductivity changes throughout

the sample. At high Mg fluxes, well above the saturation limit [29], Mg-doped GaN material will be highly resistive resulting from the formation of compensating Mg compounds and high compensation from unintentional defects [11]. Since this analysis was done on a Mg-graded GaN sample up to well beyond the saturation point at the surface, the surface was highly resistive. Furthermore, there is no noticeable change in the EDs of Ga HASIs for approximately the first 10 min of sputtering, indicating that there are no drastic changes to the conductivity of the sample. This highly resistive region is labeled "A" for reference. Shortly after 10 min, beyond region "A," the EDs begin to noticeably change shape. The shift in the EDs was expected as the sputtered crater reached deeper layers of lower resistivity from lower Mg doping, since a doping level below the saturation limit would eventually be reached and conductivity would therefore change drastically. In this deeper region, the specimen develops less charging as a result of better conductivity, which coincides with the decreasing Mg grade, or more specifically, the free carriers created by the Mg as the concentration becomes less than the saturation limit. This conductive region, which shows variable EDs of the Ga HASIs, persists for about 10 min and is labeled "B" for reference. Further into the sputtering process, beyond region "B," a second stable region of the EDs is observed. Again, a region of stable EDs indicates a region of constant resistivity in the layer. Because there were no layers of constant Mg doping in the sample, this second region of stable EDs must be highly resistive, though this time, the high resistance is due to low or zero Mg doping and thus a lack of free carriers. In this region, the sample conductivity is background limited, or undoped and thus either does not vary with changes in the low Mg flux, or the layer is not doped with Mg at all. This second highly resistive, stable region

is labeled “C” for reference and lasts about 10 min of sputter time. Finally, beyond region “C,” the EDs go through another drastic change as the Ga HASI signal drops to the level of background noise, indicating the sputtered crater has reached the AlN buffer layer and substrate.

The characteristic profiles for each of the regions, “A,” “B,” and “C,” are comparatively shown with more detail in Figure 23. Shifting of the peak energy can be clearly seen in this figure. The peak energies are centered approximately on -5V, +20 V and +5V for regions “A,” “B,” and “C,” respectively. The peak movement shows the EDs shifted to higher peak energies for conductive layers and back to lower peak energies for highly resistive layers, which is consistent with the use of positive primary ions.

*4.4.2 Step Mg profile*

The results from the Mg-graded GaN sample were augmented by the step profile of Mg-doped GaN, shown in Figure 24. From left to right, as the sputtering process begins, the Mg incorporation level initially rises from a layer grown with higher Mg flux to a layer of decreased Mg flux, which is predicted behavior well above saturation for Mg-doped GaN [29]. However, the Ga HASI ED is unchanged during this time since conductivity remains low as a result of defects associated with this high level of Mg doping. Furthermore, when the Mg incorporation level drops significantly at the sixth peak from the left, corresponding to a Mg concentration of approximately $1 \times 10^{19}$ $cm^{-3}$, a shift in the Ga HASI ED appears, indicating a layer of different conductivity has been reached. It can clearly be seen in Figure 24 that the ED peak shifts to higher energies/voltages for the decreasing Mg incorporation by noting the Ga HASI signal at -

12V target bias potential drops below the same signal at 0 V, which drops below the same signal at +12V. The power of this technique is illustrated by the ability to observe these changes in resistivity for buried layers of Mg-doped GaN, which aren't directly electrically measurable and finding optimal resistivity among the used fluxes without analyzing several samples. The observed changes in the EDs in the Mg step profile experiment reinforce the conclusions of the Mg graded profile for both regions "A" and "B." Region "C" was not characterized in the step profile experiment since no low doped or undoped bulk layer was grown significantly thick enough. Furthermore, it is interesting to note the relationship between increasing Mg flux and Mg incorporation, which initially increases with flux, but finally decreases with increasing Mg flux.

### *4.4.3 Ruling out matrix effects*

Matrix effects from the varying Mg concentration were ruled out using the previously discussed Cs-beam SIMS technique. Figure 25 shows the consistent relationship between detected Ga ions and detected CsGa complex ions throughout the film of the Mg step profile sample. After a short time to reach sputtering equilibrium at the top of the film (time zero), the Ga and CsGa signals are extremely stable and consistent until reaching the AlN/Sapphire substrate. Since the Ga signal would be affected by any changes in the matrix and the CsGa signal would not, the fact that they are both constant shows that there are no changing matrix effects present in this scan, or the data from other scans of this sample, including those using the oxygen beam. Also shown in the figure is the noisy CsMg signal, which is overcome by the shoulder of the Al signal at the AlN/sapphire interface. This technique was also applied to the Mg linear profile to verify the absence of matrix effects. Furthermore, since deposited Cs metal

atoms from the primary beam would assist in dissipating charge buildup, surface charging effects are not seen with the Cs-beam SIMS analysis.

### *4.4.4 Electrical characterization*

To examine the electrical properties of these three distinct regions of Mg doping, additional bulk samples, grown with a constant Mg concentration corresponding to regions "A," "B," and "C," were compared using National Institute of Standards and Technology methods for resistivity and van der Pauw Hall measurements [120], as described in Appendix C. For samples grown with a constant Mg concentration corresponding to region "A," a resistivity of approximately $\rho = 90\ \Omega\cdot cm$ was measured. Likewise, for samples grown with a constant Mg concentration corresponding to region "C," a resistivity of approximately $\rho = 110\ \Omega\cdot cm$ was measured. However, the most promising results came in samples grown with a constant Mg concentration corresponding to region "B." For samples grown in this region of Mg concentration, at a Mg flux just below $6 \times 10^{-10}$ Torr, BEP, an average resistivity of $\rho = 0.59\ \Omega\cdot cm$, an average mobility of $\mu = 8.8\ cm^2/Vs$ and an average hole concentration of $p = 1.2 \times 10^{18}\ cm^{-3}$ were measured, near the best reported values [82]. These electrical results confirm the analysis of the ED-SIMS data and provide a method for optimizing the conductivity and therefore the carrier concentration in Mg-doped GaN.

## 4.5 Summary

Monitoring changes in the EDs of the Ga HASIs during a SIMS depth profile of varying Mg-doped GaN has shown to be a good way to identify changes in the resistivity of layers. More specifically, this technique can allow the identification of the boundary between conducting and insulating layers and has therefore proven to be useful to

optimize the Mg-doping of GaN. The method outlined also provides a quicker alternative for optimizing resistivity from growing and measuring multiple bulk samples. Changes in the EDs of HASIs in SIMS for a homogeneous material, such as Mg-doped GaN, indicate changes in surface charging effects. Therefore, the regions of constant and varying Ga HASI EDs observed in graded and step-profile Mg-doped GaN samples were used to relate the electrical properties of bulk Mg-doped GaN samples with different Mg doping concentrations. Furthermore, it may be possible to use this method of analyzing the EDs through ED-SIMS analysis to quantitatively optimize the Mg concentration in GaN while still maintaining low resistivity. Finally, because of the universal applicability of ED-SIMS to all semiconductors which are normally highly resistive in undoped or highly doped cases, this may prove to be a useful method of optimizing doping of other semiconductors as well.

# CHAPTER 5*: IN SITU* GROWTH CHARACTERIZATION USING RHEED AND DMS

Currently, most epitaxy of III-nitrides via MBE relies heavily on qualitative and subjective analysis of RHEED patterns. Traditional RHEED oscillations, discovered in the 1970s for GaAs [121], are rarely observed in III-nitrides because the amplitude of the oscillations is small enough to be lost in the signal noise and is quickly dwarfed by long-range disorder from nuclei formation, growth and metal surface coverage [122, 123]. Thus, until recently, most III-nitride researchers have relied on a qualitative RHEED pattern, including the "streakiness", relative dimness of the streaks to the background and similar qualitative properties to indicate the growth regime and most researchers still rely on qualitative techniques. Such subjective RHEED image analysis is difficult to reproduce, especially given the extreme sensitivity of material quality to III/V ratios. Interpretation and reproduction of qualitative analysis techniques are particularly difficult during nucleation of new mismatched layers. Therefore, an *in situ* quantitative growth regime determination technique using RHEED and DMS was developed. This technique was developed with AlN while trying to optimize buffer layers for Mg-doped GaN, but is applicable to all III-nitrides that exhibit the three growth regimes, including GaN, AlN and AlGaN. The results of this technique can be used to improve reliability of Mg-doped GaN by monitoring growth regime *in situ*.

## 5.1 Growth conditions

Sapphire substrates were coated with molybdenum on the roughened backside and were then either used as 2 in. diameter substrates, or diced into 1 cm squares for

substrates. The samples were prepared for growth according to Appendix A. Following low-temperature nitridation, the samples were heated to 800° C at 2° C/s to prepare for the experiments. To determine representative growth conditions above and below the Al droplet regime, four samples of bulk AlN were grown for 20 min each on 2 in. substrates with constant Al cell temperatures. Two of the samples were grown below the droplet regime barrier at Al cell temperatures of 1080° C (Al flux of $2 \times 10^{-7}$ Torr beam equivalent pressure, BEP) for sample A and 1090° C ($2.4 \times 10^{-7}$ Torr BEP) for sample B and two of the samples were grown above the droplet regime barrier at Al cell temperatures of 1095° C ($2.6 \times 10^{-7}$ Torr BEP) for sample C and 1100° C ($2.9 \times 10^{-7}$ Torr BEP) for sample D. While samples C and D were clearly grown in the Al-rich regime, since they had Al droplets in the center of the sample, samples A and B had no Al droplets in the center 1 in. diameter of the sample. However, Al droplets did exist outside the center 1 in. diameter region, near the edge of the sample. This effect is thought to be due to the higher concentration of nitrogen supplied by the plasma source at the center 1 in. diameter, since the plasma aperture was also approximately 1 in. in diameter before the aperture change, described in Appendix B. Therefore, these samples with droplets only on the edge are thought to be representative of the N-rich or intermediate regime. Furthermore, the smaller 1 cm square samples were used to verify the various observations of the study were not a result of nonuniformity on the larger 2 in. substrates. Unless otherwise noted, the results from the smaller 1 cm square samples reflected those from the larger 2 in. samples.

RHEED intensity and DMS [124] responses to shutter transitions were recorded at the cell temperatures. The nitrogen plasma was constantly exposed to the substrate

during the length of the experiments, while the Al shutter was opened and closed. To rule out any possible run to run variations, particularly substrate temperature variations, a single test sample was used to characterize RHEED intensity and DMS responses at these four Al cell temperatures after the individual bulk growths, to correlate surface characteristics with the RHEED signatures.

Figure 27 shows the RHEED intensity responses for Al cell temperatures corresponding to samples A, B, C and D, or 1080, 1090, 1095 and 1100° C, respectively, exposed to the sample for 30 s each. Likewise, Figure 28 shows the RHEED intensity responses for Al cell temperatures corresponding to those used for samples B, C and D, or 1090, 1095 and 1100° C, respectively, exposed to the sample for 3 min each. The second, longer Al cell exposure data were taken to observe any effect of exposure time on the delay to RHEED response upon closing the Al shutter for the droplet regime. The time constant of the exponentially decaying RHEED intensity upon Al shutter opening was derived by nonlinear least squares fitting for each Al cell temperature in both experiments and is shown in the figures.

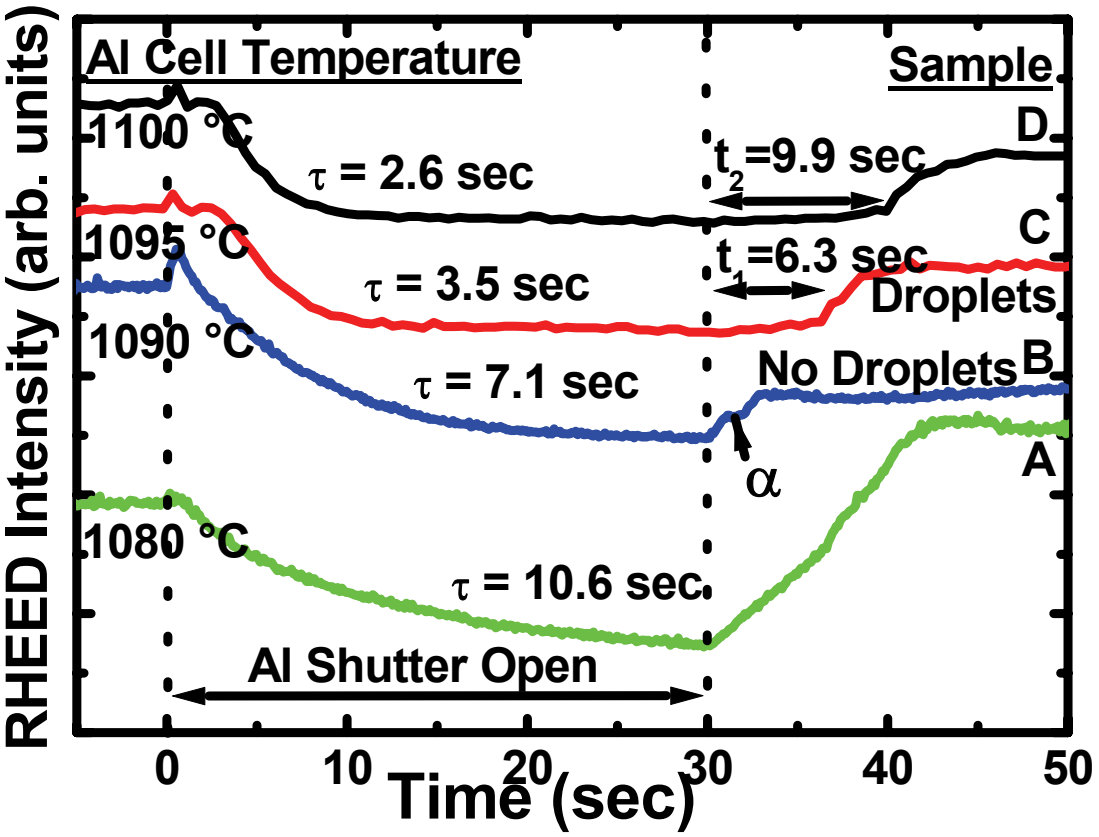


Figure 27: RHEED intensity signatures from AlN as a function of time with increasing Al flux, bottom to top. Time constants for each response are shown beside the curve and are inversely correlated to Al flux. Droplets were formed for samples C and D, or Al cell temperatures above 1090° C. Also shown is the two-step response to closing the Al shutter for Al cell temperature of 1090° C, denoted as feature α and corresponding to the growth condition for sample B. Lastly, the delay in response grew with flux once in the droplet regime as shown by $t_1 < t_2$ (color online).

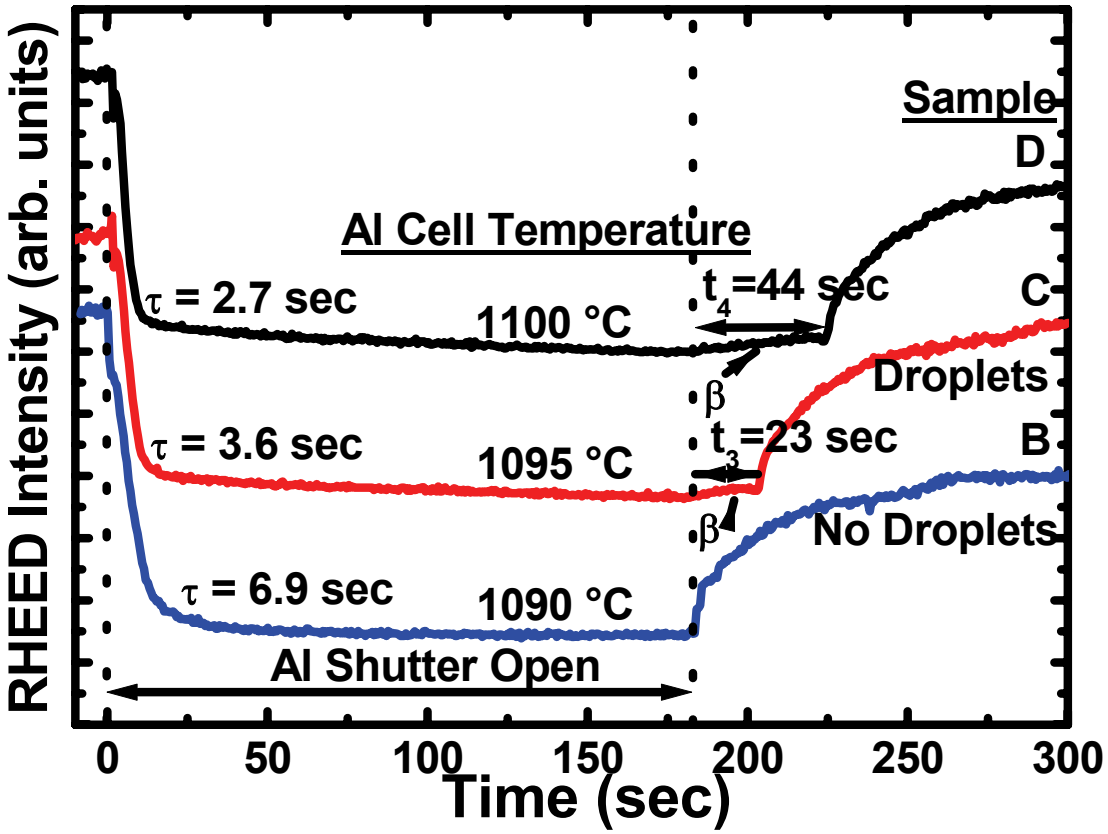


Figure 28: RHEED intensity signatures from AlN with a longer shutter open time. The delay time is related to the integrated Al droplet volume on the surface and requires time to be consumed into the Al bilayer and/or capped by the nitrogen. The time constants of falling RHEED intensity upon opening the Al shutter are shown again to vary inversely with Al flux. Also shown is a unique RHEED intensity response to accumulated droplets, denoted as feature β and response delay dependence on flux and time, shown by $t_1 < t_2 < t_3 < t_4$ (color online).

## 5.2 Characteristic RHEED responses to growth regime

### *5.2.1 Falling RHEED intensity time constant*

Immediately apparent from Figure 27 is the inverse relationship between the time constant of the falling RHEED intensity upon Al shutter opening and the Al cell temperature/flux. This inverse relationship between flux and time constant is consistent with the general trend of previous studies [125]. The derived time constants for the

short and long shutter transition RHEED tests varied by an average of 0.1 s, less than 3%, for each Al flux level. The time constant is therefore proven repeatable and can thus be used as a quantitative measure between and throughout runs to maintain consistent growth conditions by adjusting flux to maintain time constant values. Furthermore, since the quantitative metric of growth condition found from the time constant depends only on incoming minus desorbed flux (or net flux), it is not affected by emissivity or substrate temperature changes, as are other optical growth characterization techniques.

Lastly, the time constants were plotted on an Arrhenius plot with the flux measurements at each Al cell temperature used, and the data is shown in Figure 29. The activation energy for the time constant series was -11.68 eV, while the activation energy of the Al flux from the effusion cell was 2.93 eV.

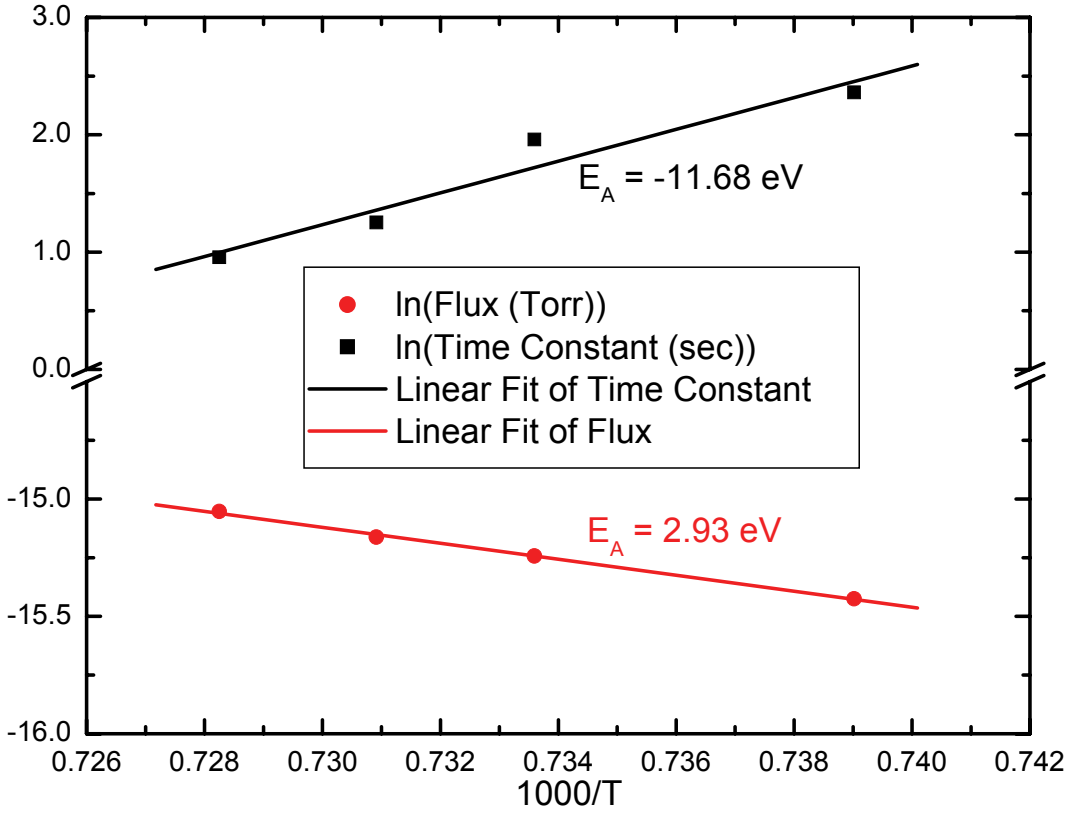


Figure 29: Arrhenius plot of flux and time constant for each Al cell temperature used in Figure 27, with activation energy shown for each series (color online).

### *5.2.2 Falling RHEED intensity oscillations*

Also observed in Figure 27 and Figure 28 is an initial RHEED intensity increase for all samples, which may be a partial oscillation. The feature is small for sample A and much more apparent in Figure 27 than in Figure 28 since it lasts only for 1 – 2 s, but exists in both figures. It is also important to note that the time constant derivations, discussed previously, were done after the effects of these features were subdued and thus an exponential curve could be fitted to the data. Although other studies have demonstrated sustained growth RHEED oscillations with AlN [123, 126], those growths had lower substrate temperature and lower Al fluxes. However, since AlN film quality

has been shown to decrease with substrate temperature [35], even the unique partial oscillations at the elevated temperatures are useful for characterizing growth regime.

Furthermore, for samples C and D, or Al cell temperatures above 1090° C, the partial oscillation feature develops into a full oscillation, but only for one period before the evanescent intensity is overcome and decreases dramatically. The period of this full oscillation is between 1.7 and 2.1 s and could be indicative of AlN growth or Al bilayer buildup. If the oscillation is evidence of AlN growth, the growth rate can be calculated by assuming that the period of oscillation is the time taken to grow a monolayer of AlN. Using half the height of a single unit cell of AlN, ½ (4.98 [127]) Å , over the period of oscillation, the growth rate was estimated to be 0.53 – 0.43 μm/h, which is slightly higher than the approximate actual 0.3 μm/h growth rate, as determined by SIMS and profilometry, as detailed in Appendix D. These RHEED oscillations may slightly overestimate the actual steady-state growth rate because of the effects of long time range effusion cell cooling and subsequent flux reductions upon opening of the cell shutter. Alternatively, the oscillation-like signature could be indicative of the Al bilayer buildup, which would allow the determination of the rate of bilayer formation. Since the bilayer is made up of approximately two to three monolayers of metal atoms [51] and a full RHEED growth oscillation indicates the formation of one monolayer, the bilayer should be completely formed in two to three times the period of oscillation. For these experiments, with oscillation periods ranging from 1.7 to 2.1 s, this assumption would suggest approximately 3.4 – 8.4 s for bilayer buildup for the given growth conditions.

### *5.2.3 Rising RHEED intensity delay and oscillations*

More information can be derived by observing the RHEED intensity response to the Al shutter closing, providing an indicator of growth regime, since it depends only on desorption of Al from the sample. There exist clear regime distinctions in Figure 27 and Figure 28 for Al shutter closing. For sample A, with the most N-rich conditions, there is an immediate and nearly constant rate of rise in the RHEED intensity upon Al shutter closing. Conversely, for samples C and D in the droplet regime, there was a delay in the RHEED intensity response, dependent upon the Al cell temperature/flux. Finally, for sample B, the growth in the intermediate regime, there was a combination of the two responses. Initially, there was an immediate and constant rate of rise for the RHEED intensity; but before reaching steady-state intensity there was a slight delay at an intermediate stable intensity. The resulting response has a two-step appearance and is labeled as α in Figure 27. The feature is barely visible in Figure 28 for the same Al cell temperature because of the feature's brevity and the scale of the graph. Possible causes of feature α include oscillations from growth of AlN as the Al bilayer is consumed, oscillations from the Al bilayer as it is depleted [53], or an aggregate effect of the RHEED beam sampling a region larger than the droplet-free inner diameter of the sample. This final possibility may cause feature α in the RHEED response as a result of the combined sampling of regions with Al droplets and regions without Al droplets and therefore a combination of the more N-rich and droplet responses. This possibility is important because it allows the ability to predict problems with flux uniformity and also gives clues as to the diameter of the droplet-free region in the center of the sample. In an attempt to discern the likelihood of this interpretation, growths were repeated on the 1 cm

samples with identical results. However, while the smaller 1 cm samples exhibited this behavior, they too could suffer from nonuniformity on a much smaller scale as edges are typically cooler than centers.

The correlation between the RHEED intensity delay and Al-rich conditions in the droplet regime is a result of droplet buildup that must be desorbed or consumed by AlN growth before the RHEED intensity can recover and increase. Supporting this correlation, the delay in response is consistently increased for higher Al cell temperatures/flux and/or longer exposure times, i.e., $t_1 < t_2 < t_3 < t_4$, as shown by Table 3. For longer periods of delay, as those shown in Figure 28, a slow, long-range RHEED intensity rise is observed for droplet conditions immediately upon closing the Al shutter. These features are labeled as β and are dwarfed by a dominant RHEED intensity rise after the aforementioned delay. Interpretation of feature β is unknown at this time, but could also be a result of nonuniformity due to the RHEED beam sampling a large surface area, as it did not appear in the smaller 1 cm square samples.

Table 3: Relationship between the RHEED intensity delay time to increasing flux and increasing exposure time. RHEED intensity delay time is denoted as $t_i$, where $i$ corresponds to the appropriate flux/temperature and exposure time parameters. Percentage increase in flux and exposure time is not correlated with the increase in the RHEED intensity delay.

| | | Exposure Time (s) | | Increase (%) |
|---|---|---|---|---|
| Flux (Torr, BEP) | Temperature (° C) | 30 | 180 | 200.00 |
| $2.63 \times 10^{-7}$ | 1095 | $t_1 = 6.3$ | $t_2 = 23$ | 265.08 |
| $2.89 \times 10^{-7}$ | 1100 | $t_3 = 9.9$ | $t_4 = 44$ | 344.44 |
| Increase (%) | 9.92 | 0.46 | 57.14 | 91.30 | |

## 5.3 III-nitride mass balance analysis

The process of III-nitride growth can be described with the mass balance equation

$$J = Kc_1 + D_1c_1 + \frac{dc_1}{dt} + D_2c_2 + \frac{dc_2}{dt} + D_3c_3 + \frac{dc_3}{dt}, \tag{15}$$

where $J$ is the impingent flux, $K$ is the incorporation or growth rate, $c_i$ is the effective surface concentration, $D_i$ is the desorption rate, 1 represents the adsorbed metal atoms, 2 represents the metal bilayer, and 3 represents excess metal in droplet form. $D_i$ can be written as

$$D_i = D_o e^{-\frac{E_{di}}{kT_s}}, \tag{16}$$

where $D_o$ is a constant, $E_{di}$ is the activation energy for desorption, $k$ is Boltzmann's constant, and $T_s$ is the substrate temperature. When N-rich or metal-rich before the buildup of excess metal ($c_2$ and $c_3$ equal to zero), equation 15 reduces to

$$J = (K + D_1)c_1 + \frac{dc_1}{dt}, \tag{17}$$

with the solution

$$c_1(t) = \frac{J}{K + D_1}\left(1 - e^{-(K+D_1)t}\right), \tag{18}$$

which is valid for $0 \le t \le \infty$ if N-rich ($J \le J_1$) and for approximately $0 \le t \le \frac{3}{K + D_1}$ if metal-rich ($J \ge J_1$), where

$$J_1 = c_1(\infty)(K + D_1). \tag{19}$$

The multiple of 3 represents about 95% coverage of the metal adatoms before the buildup of the metal bilayer begins. In the intermediate regime, the surface metal concentration

$c_1$ is full or saturated, $c_1(\infty)$ becomes a constant and $dc_1/dt$ becomes zero. Therefore, equation 15 reduces to

$$J - J_1 = D_2 c_2 + \frac{dc_2}{dt}, \tag{20}$$

with the solution

$$c_2(t) = \frac{J - J_1}{D_2}\left(1 - e^{-(D_2)t}\right), \tag{21}$$

which is valid for approximately $\frac{3}{K + D_1} \le t \le \infty$ in the intermediate regime ($J \le J_2$),

and approximately $\frac{3}{K + D_1} \le t \le \frac{3(2.5)}{K + D_1}$ for the droplet regime ($J \ge J_2$), where

$$J_2 = c_2(\infty)D_2 + J_1. \tag{22}$$

The 2.5 multiple for the upper time limit in the droplet represents the approximately 2.5 layers of metal creating the bilayer [48-51].

Finally, in the droplet regime, the bilayer is completely built, the bilayer concentration is full or saturation, $c_2(\infty)$ becomes a constant and $dc_2/dt$ is zero. Therefore, equation 15 reduces to

$$J - J_2 = D_3 c_3 + \frac{dc_3}{dt}, \tag{23}$$

with the solution

$$c_3(t) = \frac{J}{D_3}\left(1 - e^{-(D_3)t}\right), \tag{24}$$

which is valid for approximately $t \ge \frac{3(2.5)}{K + D_1}$ in the droplet regime ($J \ge J_2$).

Assuming the exponential decay of the RHEED intensity transient reflects the exponential increase in surface metal concentration, the extracted time constant of each flux is equal to

$$\tau = \frac{1}{AJ + D_1}. \tag{25}$$

Therefore, the time to build one nearly complete layer of metal can be estimated by $3\tau$. Furthermore, the time to build up a bilayer of metal can be estimated by $(2.5)(3\tau)$, and any time greater than this should result in droplets.

This analysis was applied to the observed RHEED data for the 30 second shutter opening tests with droplets. The time constants these two signals was 2.6 and 3.5 seconds. Therefore, it should take 7.8 and 10.5 seconds to form a nearly complete layer of metal. The bilayer should completely form within approximately 19.5 and 26.25 seconds. The extra 10.5 and 3.75 seconds with the metal shutter opened after this bilayer buildup time will contribute to droplets, and the subsequent delay of RHEED intensity response upon shutter opening confirms this. While the delays of 9.9 and 6.3 upon shutter closing do not exactly match that of the extra time with the metal shutter open, the full mass balance model must be used to explain this discrepancy.

For the intermediate case the time constant was 7.1 seconds, so the time to form a nearly complete layer of metal should be 21.3. The approximate time needed to form a complete metal bilayer is 53.25 seconds, which was longer than the shutter open time, thus no complete metal bilayer was able to form, and since there were no droplets formed, there was an immediate RHEED intensity response upon shutter closing. Finally, for the most N-rich case, the time constant was 10.6 seconds, meaning the shutter opening time was not long enough for a complete metal layer to form, which would take

31.8 seconds. Since the most N-rich case did not build any excess metal on the surface, there was no delay in the RHEED intensity response upon shutter opening.

## 5.4 Nitride MBE growth kinetics model

DMS of mass 27, nominally that of Al, was recorded during the longer Al RHEED tests in an attempt to measure the desorbed Al from the sample and the results are shown in Figure 30. However, instead of mass 27 rising upon the Al shutter opening as expected, it exhibits an initial peak, followed by a steep decline to a value below the initial level. Likewise, when the Al shutter is closed, mass 27 initially declines, but then rises quickly back to the initial level, making the steady-state value of mass 27 actually higher when the Al shutter is closed. This seemingly contradicting behavior has been previously observed with DMS of aluminum gallium arsenide (AlGaAs) [128] and is actually a result of the shoulder of the large $N_2$ peak at mass 28. Therefore, the mass 27 signal is a better measure of desorbed nitrogen than of desorbed Al. As a result of the high pressure of $N_2$ in the system during growth, the peak for $N_2$ at mass 28 was beyond the upper limit of detection for the mass quadrupole and therefore comparison to the behavior of mass 27 was not possible. However, atomic nitrogen at mass 14 was monitored and found to closely match mass 27, as seen in Figure 31. To rule out the possibility of this effect being outgassing from components in the chamber, a mass spectrum was obtained and a peak unrelated to AlN, mass 40 of argon (Ar), was monitored during the shutter transition. As shown in Figure 31, mass 40 was found to be unaffected by the shutter transitions, indicating the behavior is not a characteristic of outgassing.

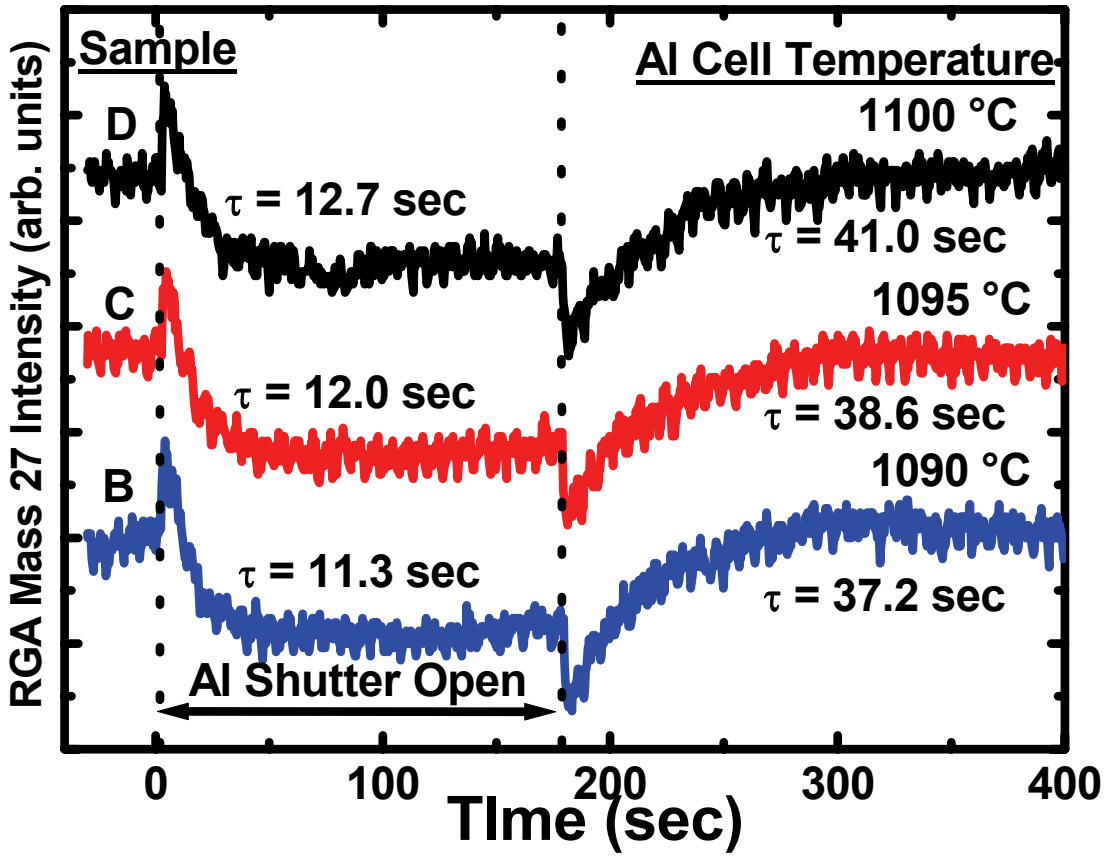


Figure 30: DMS signal showing response of mass 27 to Al shutter opening and closing. Time constants are shown for each transition and are positively correlated to the Al cell temperature/flux (color online).

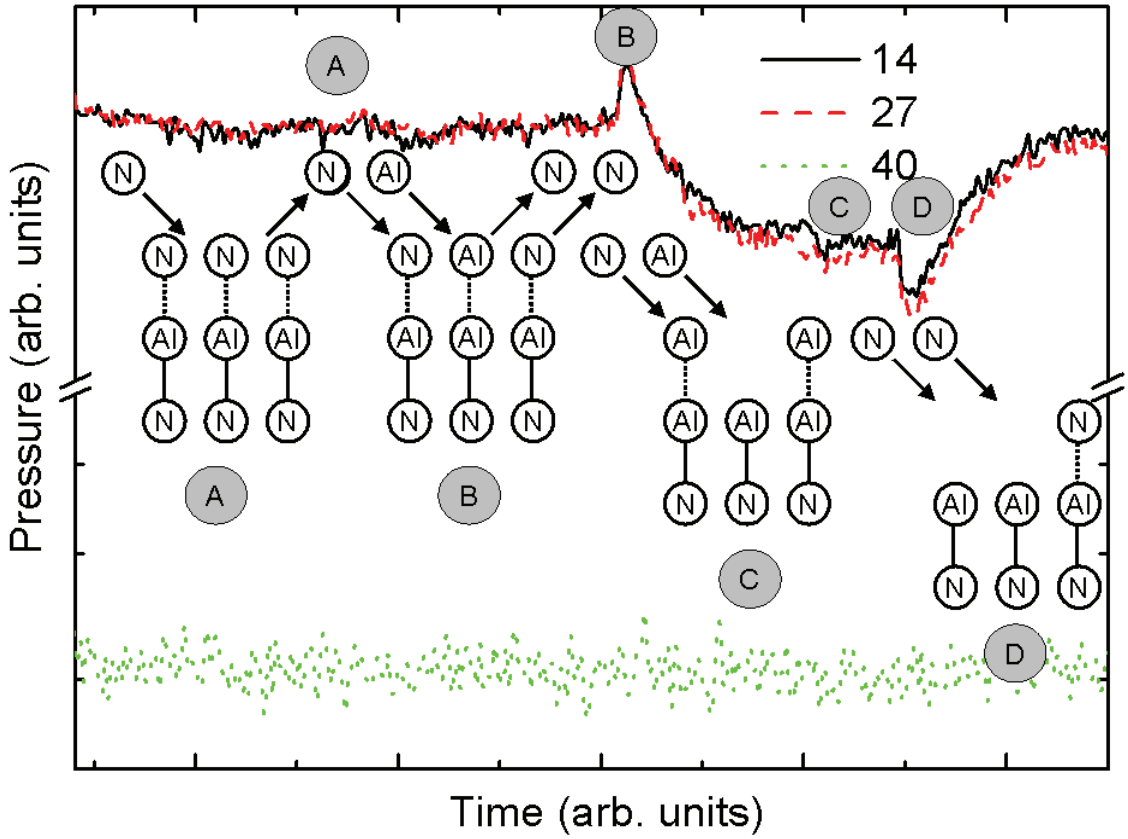


Figure 31: DMS data for masses 27, 14 and 40, showing the effect on nitrogen upon shutter transition. Mass 27 is shown in lieu of mass 28, since the peak for N2 was beyond the upper limit of the mass quadrupole. Mass 40 for Ar is included to show that the effect is not due to outgassing. Also shown are cartoons representing the different theoretical stages of the AlN surface, resulting in the observed DMS signal (color online).

In the case of DMS of AlGaAs [128], this behavior was observed for desorbed Ga when growing GaAs, upon opening and closing the Al shutter to begin and end AlGaAs. It was theorized that this response was a result of a cation-cation exchange process, where Al was exchanging or replacing weakly bonded surface Ga atoms upon shutter opening, as had been previously been observed [129], thus causing the temporary spike in desorbed Ga upon shutter opening. This theory was later supported by successfully modeling the process [130]. The similarity of the results of AlGaAs and AlN suggest a

similar process is occurring with AlN. However, with AlN, this would require a cation-anion exchange instead of the familiar cation-cation exchange. This concept of cation-anion exchange is foreign and revolutionary in the modeling of surface growth kinetics of AlN. Furthermore, because of the similarities between AlN and GaN, this new model may also be applicable to GaN growth.

When AlN is sufficiently thick (greater than 670 Å), it is mostly Al-polar [35] and Al-polar material is Al-terminated in vacuum [39]. The AlN in this experiment was thicker than 670 Å, thus making it mostly Al-polar material. With the Al shutter closed, the static AlN surface is exposed only to the nitrogen plasma, causing weakly adsorbed nitrogen to terminate the Al-polar surface. This condition is illustrated by the cartoon and region "A" in Figure 31. Upon opening of the Al shutter, the Al atoms exchange with or replace the weakly adsorbed N atoms to form the Al bilayer [131], therefore desorbing additional N, along with the impingent nitrogen atoms for a short time. This exchange process results in a temporary spike in desorption of nitrogen from the sample, illustrated by the cartoon and region "B" in Figure 31. Once the top layer of nitrogen is exchanged or replaced and steady-state is reached with the Al shutter open growth proceeds by consuming the Al bilayer, which is constantly being rebuilt by the impingent Al flux. In this state, more nitrogen is consumed and less is desorbed from the surface than with static AlN when the Al shutter closed, since growth is taking place. This behavior is illustrated by the cartoon and region "C" of Figure 31. Upon closing the Al shutter, the Al bilayer is consumed by growth of AlN with the impingent nitrogen. However, weakly adsorbed nitrogen layer is reestablished, consuming even more

nitrogen and resulting in a brief dip in the desorbed nitrogen signal. This behavior is illustrated by the cartoon and region "D" of Figure 31.

## 5.5 Summary

*In situ* determination of the growth regime in both AlN and GaN is critical for maintaining consistency between and throughout growth runs. Specific RHEED intensity responses to the metal source shutter transitions have been observed that appear to be a good indicator for specific growth regimes. First, the RHEED intensity decrease upon Al shutter opening was found to be inversely correlated to the Al cell temperature/flux. Second, a spike in RHEED intensity was observed for intermediate Al-rich conditions and an oscillation was observed for Al-rich droplet regime conditions. Third, the RHEED intensity responded differently for Al-rich droplet regime versus the Al-rich intermediate regime upon Al shutter closing. Of the observed features, only growth oscillations have been previously reported for either AlN or GaN [122, 123, 126], making this the first demonstration of the three unique features described above. DMS data were observed during Al shutter transitions and resulted in a new surface kinetics model proposed for III-Nitrides that exhibit a bilayer. This new model proposes a cation-anion exchange initially upon metal shutter opening, similar to previously observed cation-cation exchange processes, and shows preferential buildup of the metal bilayer before growth. Together, these observed characteristics offer a set of tools available to quantitatively characterize the growth regime *in situ* and provide data for the realization of a closed-loop III-nitride growth control system.

# CHAPTER 6: FILM IMPROVEMENT AND STANDARDIZATION WITH MME

With these quantitative, objective and *in situ* analysis techniques, the ability to repeat and maintain growth regime conditions is possible, including growth in the intermediate regime, resulting in smooth material [48-51]. Extending the idea further, by modulating the metal source shutter under normal droplet regime conditions, thus oscillating around the barrier between intermediate and droplet regimes, growth in the intermediate regime near the droplet regime is possible, further improving material quality. This technique is called metal modulation epitaxy (MME). A similar growth technique was introduced in 1987 for GaAs/AlGaAs, called migration enhanced epitaxy (MEE) [132]. However, with MEE, the anion (As) shutter and cation (Ga and Al) shutters were opened exclusively with an alternating pattern. Because the cation atoms are reactive with anion atoms, the cation atoms had a longer surface diffusion length in the absence of the anion. The effect was enhanced migration for the cation atoms and improved material quality from better epitaxial self-organization. A modulated growth technique was also recently demonstrated for improved intrarun uniformity of GaN [133]. However, it would be useful to observe any surface morphology improvements as a result of enhanced migration using a modulated growth technique with the knowledge gained from the *in situ* analysis technique. While these experiments were done with AlN for buffer layer standardization, the same technique can be applied to GaN, since both material systems exhibit the three growth regimes and metal bilayer in the intermediate regime.

## 6.1 Growth and characterization conditions

Sapphire substrates were prepared for growth according to Appendix A. For these experiments the plasma was operated at 0.35 sccm before the aperture change, described in Appendix B. Following nitridation, the substrate temperature was raised to 800° C for the AlN experiments. First, two AlN samples, (a) and (b), were grown for an h each, below and above the droplet regime barrier, close in flux and without shutter modulation. Sample (a) was grown without modulation below the droplet barrier with an Al flux of $1.14 \times 10^{-7}$ Torr, BEP and exhibited no droplets. Sample (b) was grown without modulation above the droplet barrier with an Al flux of $1.39 \times 10^{-7}$ Torr, BEP and exhibited droplets. These two samples served as control samples for comparison to the MME experiments. Then, samples (c)–(e) were grown for an h each with the MME growth technique at increasing Al flux, beginning with the Al flux resulting in droplets for the unmodulated growth (sample b) and increasing up to where droplets were formed again. Using the results from the previous RHEED AlN transient experiment [25], the appropriate period was chosen for a 50% duty cycle of the MME technique, with 10 s of Al shutter open and 10 s of Al shutter closed. In Figure 27, most of the RHEED transients reach a steady-state after 10 s [25]. Sample (c) was grown using MME and the same growth conditions that yielded droplets in the unmodulated growth of sample (b), but resulted in no droplets. A subsequent MME growth, sample (d), was done with the identical conditions, but with a nearly 19% increase in Al flux to $1.69 \times 10^{-7}$ Torr, BEP, but also resulted in no droplets. Finally, the Al flux was increased to nearly 47% higher than the original unmodulated droplet-regime flux to $2.04 \times 10^{-7}$ Torr, BEP for sample (e) and droplets were formed with MME. RHEED intensity changes were recorded during

the growths, and data are shown in Figure 32 and Figure 33, which are representative of the entire growths. The characteristics of the MME grown samples were then compared to those of the unmodulated samples with $2 \times 2$ $\mu m^2$ scan area AFM, as outlined in appendix D.2, to correlate surface morphology characteristics, as shown in Figure 34. In the case of samples with droplets, AFM was done in areas to avoid drops on the surface. X-ray diffraction (XRD) was also done on the samples, as outlined in appendix D.3, for crystallography comparison and SIMS was done to determine the growth rate for each sample. Table 4 summarizes the results of the characterization techniques.

Table 4: Comparison of 50% MME and unmodulated growth techniques and characterization results.

| Technique | Unmodulated | | 50% metal modulated epitaxy (MME) | | |
|---|---|---|---|---|---|
| Sample | (a) | (b) | (c) | (d) | (e) |
| Al flux (Torr, BEP) | $1.1 \times 10^{-7}$ | $1.4 \times 10^{-7}$ | $1.4 \times 10^{-7}$ | $1.7 \times 10^{-7}$ | $2.0 \times 10^{-7}$ |
| Droplets? | No | Yes | No | No | Yes |
| Growth rate (μm/hr) | 0.26 | 0.22 | 0.12 | 0.14 | 0.41 |
| XRD 002 FWHM (arcsec) | 64.8 | 26.28 | 24.12 | 16.2 | 26.64 |
| XRD 102 FWHM (arcsec) | 970 | 1818 | 1306 | 1057 | 1450 |
| AFM rms roughness (nm) | 6.9 | 0.62 | 3.6 | 3.8 | 1.7 |
| Average grain size (nm) | 37.6 | 409 | 87.9 | 205 | 238 |
| Grain size std. dev. (nm) | 32.4 | 480 | 92.0 | 177 | 224 |

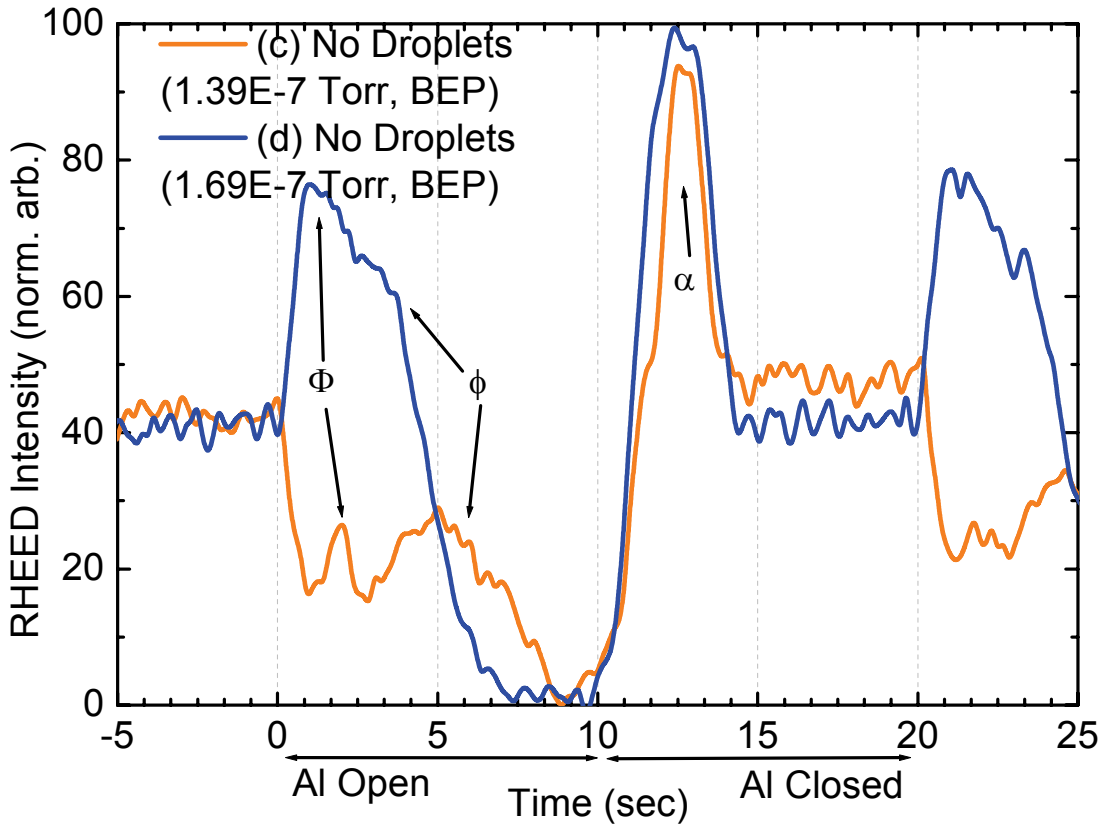


Figure 32: Normalized RHEED intensity response for shutter opening and closing during modulated growths of droplet-free MME samples (c) and (d). [Note: samples (a–d) were the unmodulated growths, not shown and sample (e) is shown in Figure 33.] Both plots exhibited three features: (Φ) an oscillation feature upon shutter opening, (ϕ) a shoulder peak attached to Φ and (α) an oscillation feature upon shutter closing/bilayer consumption (color online).

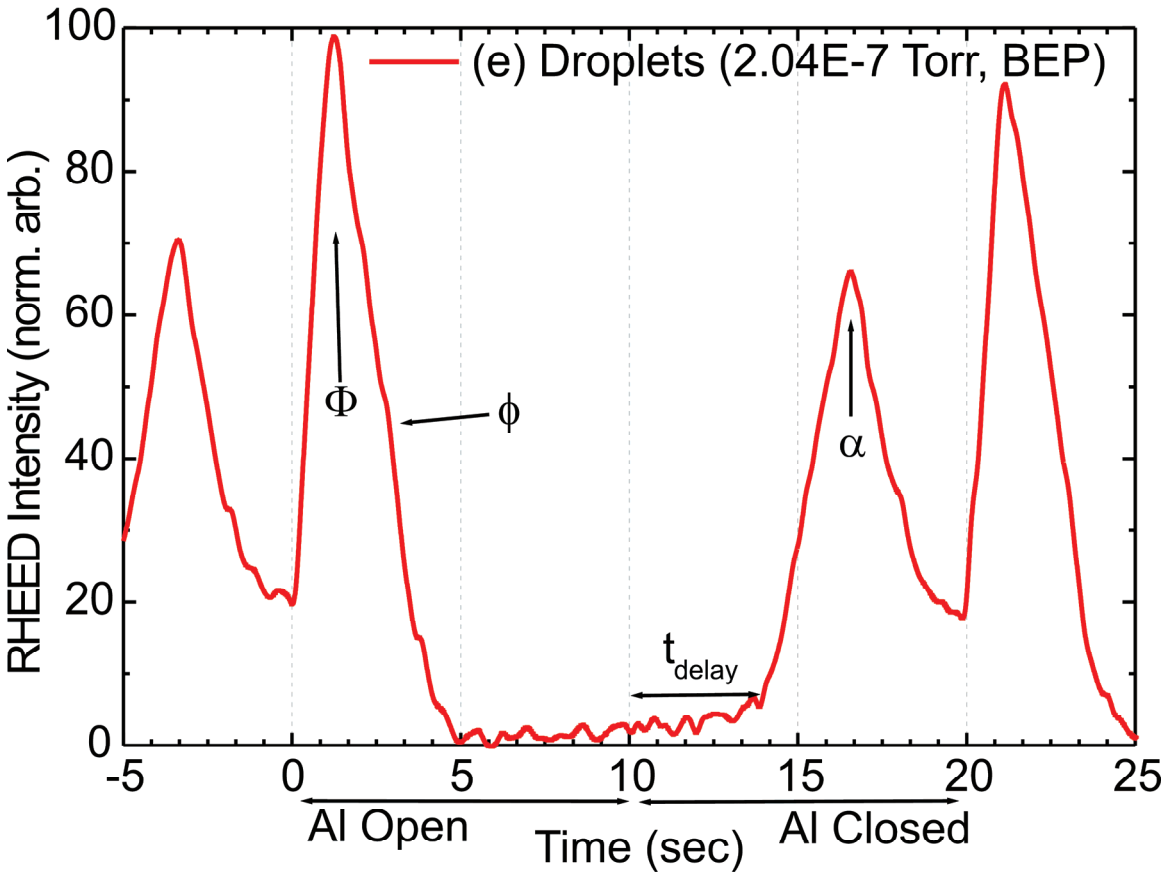


Figure 33: Normalized RHEED intensity response for shutter opening and closing during the MME growth of sample (e). This plot also exhibited the three features as seen in Figure 32: (Φ) the oscillation feature upon shutter opening, (ϕ) the shoulder peak attached to Φ and (α) the oscillation feature upon shutter closing/bilayer consumption. Additionally, the intensity response delay associated with droplet buildup is seen for this sample (color online).

## 6.2 RHEED intensity analysis

Figure 32 shows the RHEED intensity response to MME for samples (c) and (d) while Figure 33 shows the same for sample (e). Since the RHEED intensity depends on many factors, such as RHEED filament current and voltage, camera exposure time and aperture opening and screen coating, the RHEED intensity was normalized for each sample to allow shape comparison. The Al shutter was opened at $t = 0$ and closed at $t =$

10 s in the figures. Upon shutter opening, all three samples showed the oscillation feature, indicative of the droplet regime, first demonstrated in Figure 27 and denoted by Φ, but with the intensity of the feature increasing with Al flux. There was also a slower oscillation feature, φ, creating a shoulder for each primary feature, Φ. The origin of this slower feature is unknown at this time, but was also correlated with the Al flux. The feature φ was most independent of Φ for lower Al flux, forming a second peak with greater intensity than the primary peak for the lowest Al flux and was nearly indistinguishable from the primary peak for the sample with the highest Al flux. All three samples also had an oscillation feature upon shutter closing, or more specifically upon bilayer consumption as has been seen for GaN previously [53] and recently for AlN [25]. While no intensity trends were observed to correlate with Al flux, the sample with droplets had this feature time delayed compared to samples that showed no droplets. This delay, shown as $t_{delay}$ in the figure, depends on Al dose [25] and is a result of excess metal buildup on the sample surface, which is being consumed during the delay.

## 6.3 Sample morphology analysis

Figure 34 shows the AFM images of the comparative study of MME and unmodulated growth of GaN. Samples (a) and (b) were the unmodulated growths, with (a) grown below the droplet regime barrier and (b) above the droplet regime barrier. Sample (c) was grown with the same conditions as sample (b), but with MME as described previously. Sample (d) was a MME growth with the same growth conditions, but 18.78% more Al flux and still resulted in no droplets with essentially the same roughness. The results for samples c and d indicate a widening of the Al flux range required to obtain intermediate regime morphology results, compared to unmodulated

growth. Sample (e) was a MME growth with the same growth conditions, but with 46.54% more Al flux than the original unmodulated growth with droplets and had droplets at the end of the growth. The smoothest morphology came from the unmodulated sample in the droplet regime (0.622 nm root mean square (rms)), while the roughest came from the unmodulated sample grown below the droplet regime barrier (6.92 nm rms). However, using MME, the droplet-free samples had a greatly improved surface roughness over the unmodulated droplet-free sample, the lowest being 3.6 nm rms, or nearly half of the original droplet-free sample. This result shows how the MME technique expands the flux range resulting in intermediate regime morphologies, without the need to increase the substrate temperature. Because the fluxes used for the MME technique exceeded the unmodulated droplet barrier, it is thought that a complete bilayer is quickly formed upon shutter opening, with any excess Al accumulating in microscopic Al droplets. Furthermore, during the closed portion of the cycle, any excess Al in the form of droplets acts as a reservoir, feeding Al back to the bilayer and thus maintaining stable growth. Therefore, the MME technique is beneficial because Al surface migration is increased with increased Al flux and high substrate temperatures. Moreover, the improvement in roughness was not correlated to a decrease in thickness since the smoothest MME sample was also the thickest.

Grain size growth with Al flux can also be clearly seen with MME samples (d–e). While the unmodulated samples had average grain sizes of 37.6 nm below the droplet regime and 408.7 nm above the droplet regime, the droplet-free modulated samples had increasing average grain sizes from 87.9 to 205.4 nm and the MME sample with droplets had a larger average grain size of 237.7 nm. For droplet-free samples, the MME

technique yielded grains 2.3–5.4 times the size of the unmodulated sample. Table 4 and Figure 35 show a summary of the modulated growth experiment. These AFM results were consistent over the entire surface of the sample.

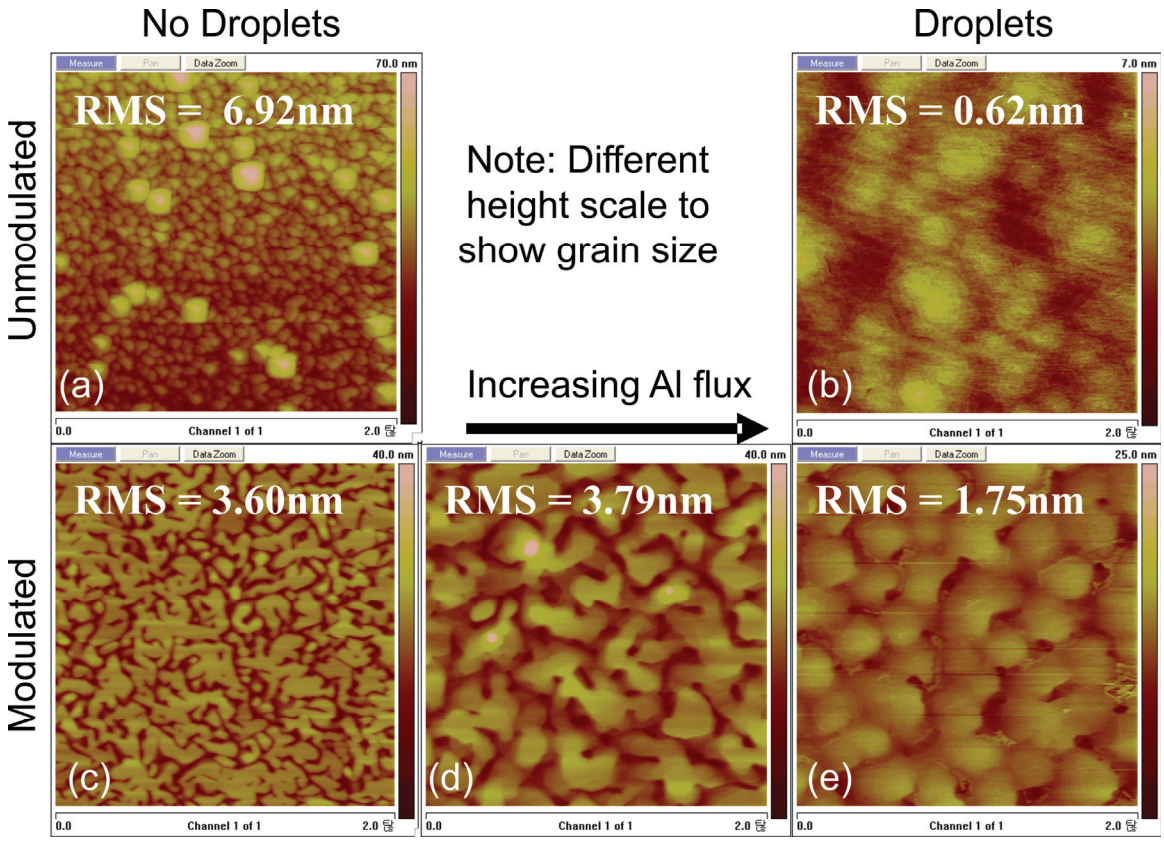


Figure 34: AFM images of AlN with rms roughness showing correlation with modulated and unmodulated growth techniques. Droplet regime scans were done in droplet-free areas (between droplets). Grain size increases with increasing Al flux for the modulated data. Other details can be seen in Table 4 (color online).

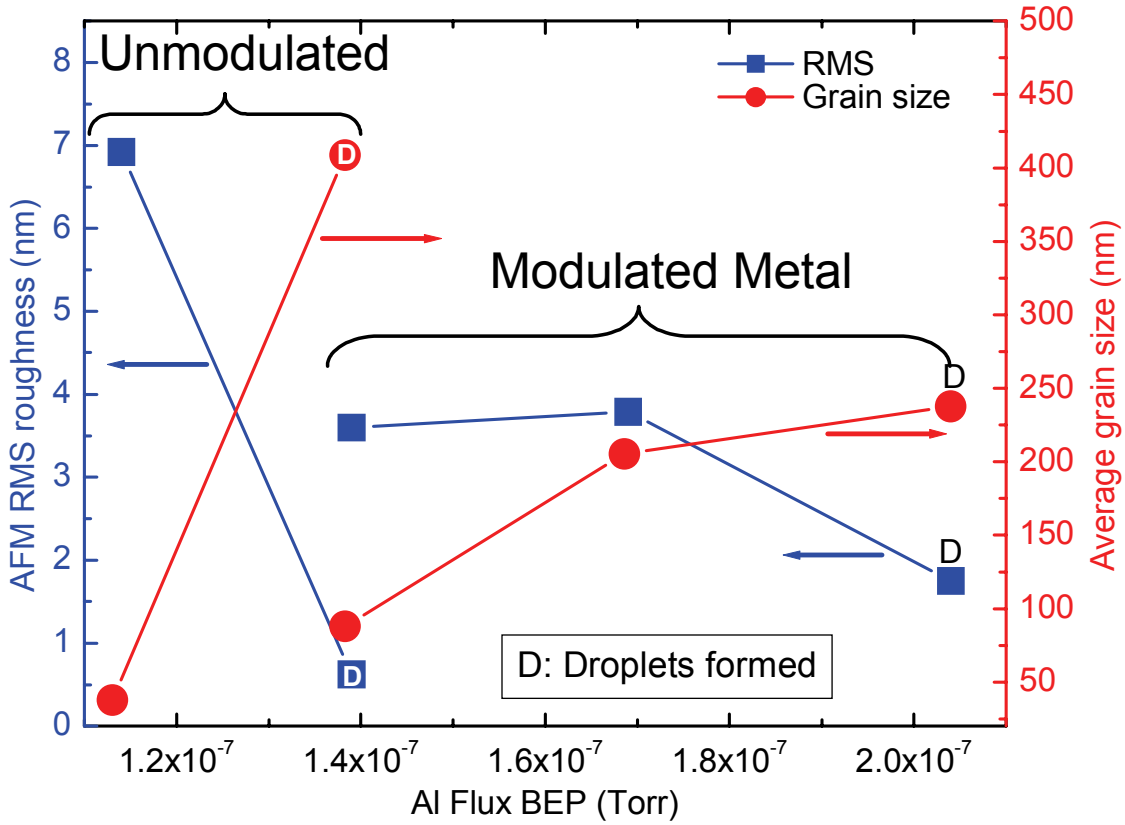


Figure 35: Plots of data summarized in Table 4 showing improved quality for MME. Droplet-free conditions were extended up to $6 \times 10^{-7}$ Torr using MME while improving roughness and grain size. Symbols with "D" indicate droplet conditions (color online).

## 6.4 MME compared to other techniques

With standard stochiometric growth, the cations impingent on the surface quickly react with the abundant anions and create small, isolated and immobile islands, resulting in a rough, three-dimensional growth. MEE was developed to increase surface mobility of metal atoms for low-temperature growth of GaAs or AlGaAs by exclusively opening either the cation (metal) or anion (As) source shutters [134]. Therefore, in the absence of the anion, the cations are free to find the lowest energy position for a layer-by-layer or two-dimensional growth. Alternatively, MME does not modulate the anion shutter but

does modulate the cation shutter. However, for MME, the flux for the cation is much higher than the anion for increased migration length of cations as a result of excessive Al-rich growth conditions, as with MEE. The increased migration length explains the improvement in roughness and grain size observed with MME. Furthermore, while there is a decreased growth rate with MEE as a result of exclusive source shuttering, MME should not suffer from a decreased growth rate as badly since growth still occurs after the metal shutter is closed by depleting the bilayer. Nevertheless, MEE has been successfully used with GaN [135], AlN [136] and InN [137].

## 6.5 Summary

The *in situ* growth regime characterization technique described previously [25] provides the ability to determine and control growth regime. With this ability, a shutter modulation technique called metal modulated epitaxy (MME) was used to move the growth conditions in the intermediate regime close to the droplet-regime barrier and enhance lateral growth, leading to improved surface morphology and wider growth window of conditions resulting in intermediate morphologies for more reproducible results. For droplet-free growth, the rms roughness was reduced to half the original value, from 6.92–3.29 nm, by using the modulation technique. Furthermore, the grain size of droplet-free growth grew by as much as 245%, from 150–520 nm.

# CHAPTER 7: SMART SHUTTERING: CLOSED-LOOP SHUTTER AUTOMATION WITH REAL-TIME FEEDBACK

Unintentional changes in growth condition can come from various sources in MBE, including inaccurate temperature measurements from varying thermocouple and pyrometer readings, and changing flux from varying effusion cell thermodynamics and changing plasma characteristics. Thermocouple and pyrometer measurements are not exact and may vary from growth to growth, resulting in inaccurate measurements of substrate temperature. For a thermocouple, the temperature variations may depend on the amount of contact, or distance from the substrate. For a pyrometer, temperature variations may depend on vacuum interface changes caused by buildup on a window, or sample emissivity changes caused by a changing film. Furthermore, there may be differences in the thickness of the backside metal coating of samples, with some samples exhibiting pinholes through the metal and resulting in a higher observed pyrometer temperature and a lower observed thermocouple temperature, both due to heat loss through the sample. Any case of an inaccurate temperature measurement can cause temperature controllers to unnecessarily compensate accordingly, leading to unstable and unreliable growth conditions.

Effusion cell flux can change as a result of changing thermodynamics. For example, when a shutter covers an effusion cell, it acts as a thermal reflector or insulator for the cell. However, when the shutter is opened and this thermal reflector is removed, the cell power requirements are changed, resulting in flux transitions that take a few seconds to stabilize. Other changes in system thermodynamics can cause similar flux

variations not only in the daily initial measured flux compared to the growth flux, but also in the intra-run and inter-run growth flux. Plasma flux can also change as a result of slight variations in molecular nitrogen flow, input plasma power and plasma efficiency. All of these plasma characteristics are subject to changes between and within runs, especially changes in plasma efficiency over time with PBN break down causing conduction through the residual boron.

Sophisticated growth control, such as a closed-loop control system, has largely eluded epitaxial growth systems. However, a closed-loop control system allows faster response to inputs, better disturbance and internal variation rejection, better tracking of input signal, lower sensitivity to system parameter errors, and lower sensitivity to changes in calibration errors [138]. Therefore, a closed-loop growth control system can be used to overcome the unintentional growth condition changes listed above. However, this increased performance comes with the tradeoff of increased cost and complexity, but a closed-loop control system is vital for MBE systems to be established as a more reliable growth process. Thus, it would be beneficial to exploit characteristics of the previously observed RHEED transients [25] to implement a low-cost and low-complexity closed-loop control system for MBE materials growth by automating the shutter modulations to make MBE more robust.

However, until recently, the RHEED data was limited to a narrow range of intensity because of camera detection limits. Most monochrome CCD cameras use 8 to 10 bits of data to represent the brightness of each pixel. Even with newer digital cameras with up to 12 bit resolution, the dynamic range between the darkest and brightest pixel is only 72 dB [139], compared to the human eye with a range of approximately 200 dB

[140], which is used for the qualitative control discussed in Chapter 5. The RHEED intensity range is often greater than 72 dB and the cameras are unable to detect changes. Recent advances in vision technology have resulted in digital cameras with a higher dynamic range of sensitivity, using up to 22 bits of information per pixel and a scaling exposure scheme to process images with a dynamic range of up to 132 dB [139]. Figure 36 shows a comparison between conventional camera images and an image from a high dynamic range (HDR) camera. The Basler A601f-HDR was used to overcome the intensity range limitation and to record RHEED intensity transient data which a computer program used to make adjustments to the shutter state, based on the growth characterization in Chapter 5 and implementation technique in Chapter 6 [24-27]. Since no software drivers were available for this new camera, custom drivers had to be implemented. Details of interfacing the A601f-HDR are given in Appendix E.

Figure 36: Left: Conventional underexposed image; Middle: Conventional overexposed image; Right: 22-bit high dynamic range camera image [139].

## 7.1 Smart shuttering approach

Though the duty cycle of the shutter modulation for the previous MME experiment was kept constant at 50%, it is also possible to use the RHEED growth regime characterization technique to determine the optimal duty cycle that may result in

smoother materials. Improvements to the MME technique are achieved through computer controlled shutter transitions based on feedback from RHEED transients [25], thus creating a closed-loop control system for MBE, the first of its kind. This new real-time closed-loop growth-feedback system is called "smart shuttering", and is an extension of the MME growth technique. "Smart shuttering" describes the ability to optimize the time of shutter opening and closing in attempt to precisely time the buildup and depletion of excess metal by limiting the time of steady-state RHEED intensity to a minimum [48-51], instead of implementing a fixed period and duty cycle, as before. This allows the efficient buildup and depletion of the metal bilayer, which should improve surface morphology and growth rate compared to the standard MME technique.

The optimization of the period and duty cycle of the MME growth technique was expected to achieve the following: increased growth rate compared to the fixed duty cycle MME technique, increased sample uniformity, increased repeatability, and improved surface morphology. Increased growth rate should be achieved by minimizing the time the film is not growing when the metal shutter is closed and no metal bilayer exists. Increased sample uniformity has already been proven using a similar technique by Poblenz, and is achieved by keeping the entire sample surface in the metal-rich regime when flooding the surface with a high metal flux [133]. However, further improvements to uniformity may be possible by using an even higher metal flux. Increased repeatability between growths should be achieved by expanding the intermediate regime growth conditions, as demonstrated with fixed-modulation MME [26, 27]. Improved surface morphology should be achieved by growing with droplet-regime conditions, but without

accumulating droplets, also as demonstrated with fixed-modulation MME [26, 27, 52, 54].

## 7.2 Growth and characterization conditions

To test these hypotheses, sapphire samples were prepared according to Appendix A, and GaN films were grown with both fixed-modulation MME, and smart shuttering MME. The substrate temperature was 550° C, and the Ga cell temperature was 990° C ($5.82\times10^{-7}$ Torr, BEP) for both growths. The nitrogen plasma source flow rate was kept constant at 1.3 sccm for both growths as well, according to Appendix B. Results were then analyzed using AFM and profilometry measurements, as outlined in Appendix D, and compared to previously grown unmodulated growths that did not exhibit droplets, but used Ga fluxes from $2.8\times10^{-7} – 3.4\times10^{-7}$ Torr, BEP.

## 7.3 Parameters of smart shuttering

The intelligence of smart shuttering comes from the ability to determine when a RHEED transient has reached steady-state, upon which a shutter transition is triggered. Figure 32 shows the RHEED transients for the fixed-modulation MME of AlN. The RHEED transient for sample (d) reaches steady state at about 8 seconds after shutter opening, and about 4 seconds after shutter closing. While the extra 2 seconds of shutter opening may be beneficial for a smoother surface, the extra 6 seconds of shutter closing only limits the growth rate, and exposes the surface to active nitrogen without a group III metal source available for growth, which may roughen the surface. On the other had, the transient in Figure 33 never reaches steady state with the metal shutter closed, and droplets remained on the surface of the sample after growth. Therefore, an algorithm was

needed to determine when the RHEED transient has reached steady state after an intensity transition in order to initiate a shutter transition.

A sliding-time window of samples from the RHEED intensity transient can be used to determine characteristics of the signal in real-time. However, due to the complexity of the RHEED responses [25], more than one characteristic of the transient must be monitored. For example, a simple and fast linear fit to the sliding time-window of samples gives the real-time slope of the signal. However, if the transient exhibits an oscillation which is fully contained within the sliding time-window, the extracted slope may be near zero, which would be a false indication of a steady state transient. Therefore, in addition to the slope, the standard deviation of the signal was also monitored. In this particular case, the RHEED intensity noise increased with the signal amplitude, and the higher intensity data was nosier than the lower intensity data. Therefore, the standard deviation was divided by the sample mean and the resulting value was used for the second monitored transient signal characteristic.

During growth, these two real-time signal characteristic values were compared to fixed values to determine if the signal was transient or in steady state. If the real-time value was above the limit, the signal was considered to be in transition, but if the real-time value was below the limit, the signal was considered to be in steady state. Shutter transitions were triggered when the signal changed from transient to steady state. Increased stability was achieved by defining different fixed-value limits of slope and standard deviation for the shutter open case and the shutter closed case. Further stability was achieved by also defining different fixed-value limits for the turning off and on of the transient condition. For example, a slope of -200 may be required to turn on the

transient condition while the shutter is opened, but a slope of -5 may be required to turn the transient condition off (indicating steady state). Likewise, a slope of 500 may be required to turn on the transient condition while the shutter is closed, but a slope of 200 may be required to turn the transient condition off (indicating steady state).

Smart-shuttering MME is therefore accomplished by determining what values of slope and standard deviation should be used to define the transient condition. More aggressive smart-shuttering MME uses conditional parameter values that result in a higher shutter open to shutter closed time ratio. Figure 37 compares representative RHEED intensity transients for fixed-modulation MME, standard smart-shuttering MME, more aggressive smart-shuttering MME, and most aggressive smart-shuttering MME. Table 5 lists the parameters used for each of the MME techniques. The results of the normal smart-shuttering MME are very similar to the fixed-modulation MME, with only an increase to 1.06 for the ratio of shutter open to shutter closed time. The more aggressive smart-shuttering MME used stricter conditions for closing the shutter once opened, and allowed the shutter to be opened much easier upon closing. This resulted in a shutter open to closed time ratio of approximately 1.53, a significant improvement over the standard smart-shuttering MME. Finally, the most aggressive smart-shuttering used even stricter criteria for closing the shutter once opened, and much easier conditions for opening the shutter upon closing. To accomplish this second behavior, a higher slope and standard deviation value was used to turn off the transient condition once it was on when the shutter was closed, as shown in Table 5. This resulted in an instantaneous shutter opening once the transient condition was met. The resulting shutter open to closed time ratio was over 3.5 for this method. However, such aggressive parameters did not allow

the excess metal to be consumed from the surface, and thus droplets remained on the surface at the end of this growth. It is also interesting that the intensity levels of the aggressive smart-shuttering MME growths were much lower than the others. However, the most aggressive smart-shuttering MME intensity had the lowest intensity and never reached the higher intensity level of the less aggressive method. The intensity signal was not allowed to fully recover for the most aggressive smart-shuttering MME growth, and therefore never reached steady state or the higher intensity level. Thus, the moderately aggressive smart-shuttering MME parameters were determined to be the best of the possibilities tested.

## 7.4 Improved growth rate

The shutter open to closed time ratio is relative to the metal flux, and a better measure of effectiveness would be the time spent at steady state with the shutter closed. Compared to the fixed-modulation MME, the moderately aggressive smart-shuttering MME method had a longer shutter open time, a shorter shutter closed time, and a subsequent shorter time at steady state with the shutter closed. The closed shutter steady state time was improved from approximately 6 – 7 seconds, or 60 – 70% of the total time the shutter was closed, to approximately 1 – 2 seconds, or 13 – 26% of shutter closed time, using smart shuttering. The additional time gained during shutter opening and reduced closed shutter steady state time resulted in an increase in growth rate compared to fixed-modulation MME. According to profilometry measurements, as outlined in appendix D.4, the growth rate increased from 0.54 μm per hour with fixed-modulation MME, to 0.86 μm per hour with smart-shuttering MME, an increase of nearly 60%, supporting the hypothesis of a faster growth rate with smart-shuttered MME.

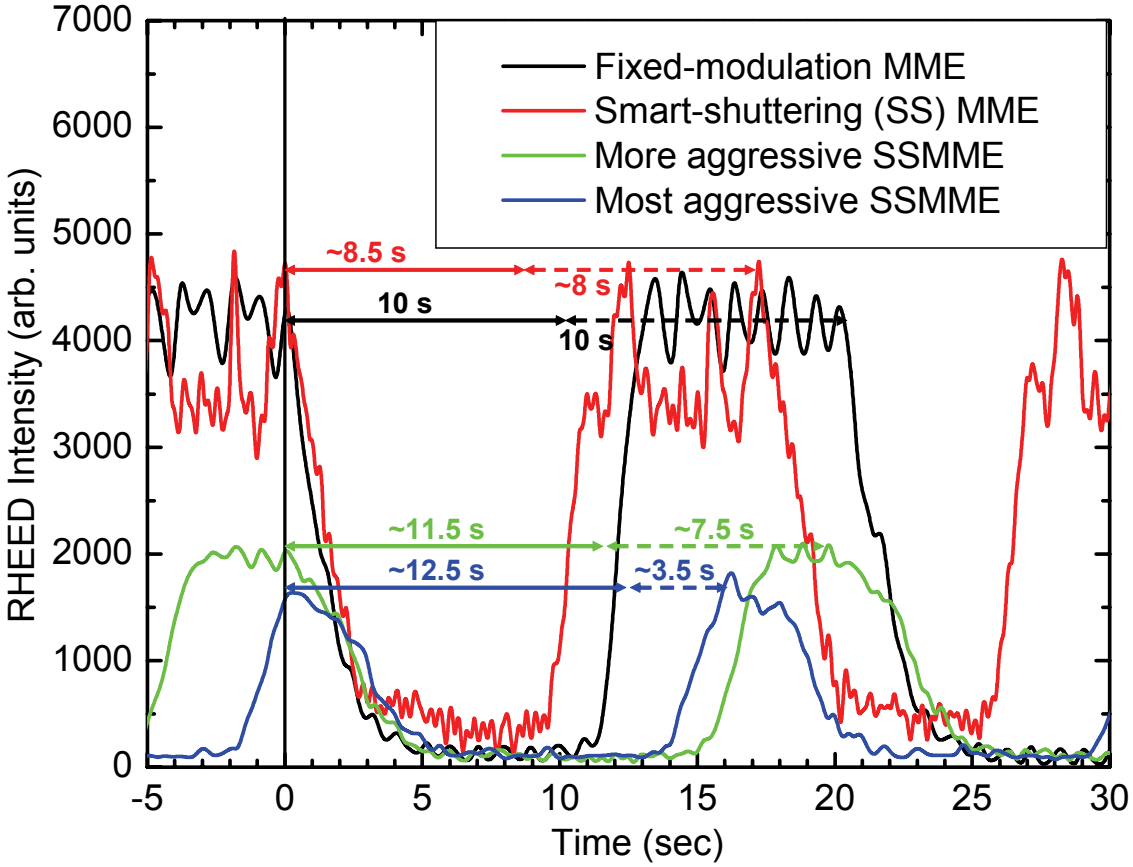


Figure 37: RHEED intensity transient data recorded for fixed-modulated MME (black), normal smart-shuttering MME (red), more aggressive smart-shuttering MME (green), and most aggressive smart-shuttering MME (blue). Shutter open times are shown by the solid double-arrow lines, and shutter closed times are shown by the dashed double-arrow lines, and values are shown for each case in the given color (color online).

Table 5: Parameters used for each of the MME growth techniques.

| Technique | Fixed-modulation MME | Smart-shuttering MME | More aggressive smart-shuttering MME | Most aggressive smart-shuttering MME |
|---|---|---|---|---|
| Shutter Open | | | | |
| Turn on slope limit | | -20 | -100 | -100 |
| Turn off slope limit | | | -20 | -10 |
| Turn on SD limit | | 0.15 | 20 | 15 |
| Turn off SD limit | | | 5 | 5 |
| Shutter Closed | | | | |
| Turn on slope limit | | 20 | 1000 | 50 |
| Turn off slope limit | | | 1000 | 1000 |
| Turn on SD limit | | 0.2 | 30 | 5 |
| Turn off SD limit | | | 30 | 100 |
| Avg. open time (sec) | 10 | 8.5 | 11.5 | 12.5 |
| Avg. closed time (sec) | 10 | 8 | 7.5 | 3.5 |
| Ratio | 1 | 1.06 | 1.53 | 3.57 |
| Droplets? | No | No | No | Yes |

## 7.5 Automatic growth regime determination

Additionally, with the increased camera intensity range, exponential curves were fit to the falling RHEED intensity upon shutter opening for a real-time definition of the current growth regime, based on previous growth results. The exponential curve fit was started upon shutter opening after any oscillations subsided, and ended when the shutter was closed. The time constant of the exponential curve was then compared to historical values that define each growth regime, and the growth regime was displayed. For example, if a time constant of 2.6 sec was extracted from the exponential fit, and it is known that the droplet-regime barrier exists at an exponential time constant around 4 sec, then the program would report that the current growth is taking place in the droplet regime since the current time constant is less than 4. All of the programming was done

using National Instruments LabVIEW, with custom written camera interfacing details given in Appendix E. A screen shot of the smart shuttering program is shown in Figure 38.

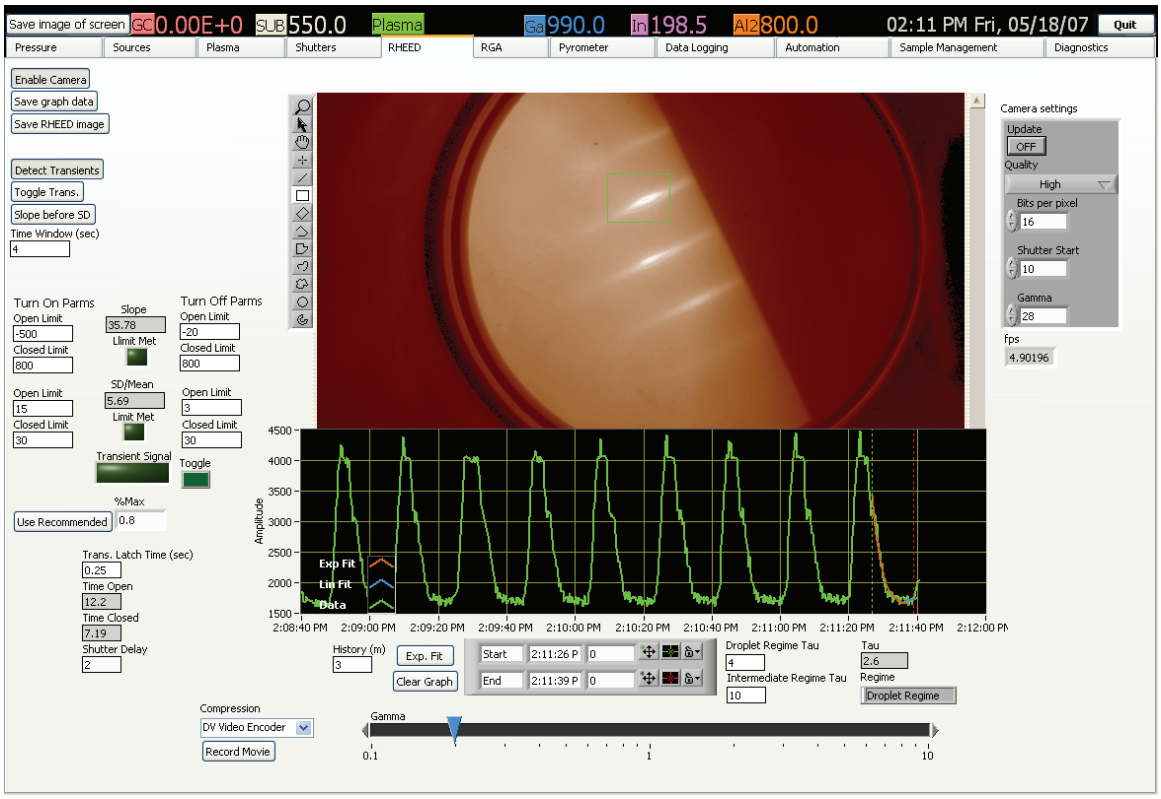


Figure 38: Screen shot of smart shuttering MME program, showing transient indicator limit controls, RHEED image, and RHEED intensity response (color online).

## 7.6 Improved surface morphology

To test the hypotheses of improved surface morphology and improved repeatability, AFM measurements were done on the GaN samples according to appendix D.2, and are shown in Figure 39. Table 6 shows the characterization values for the samples shown in Figure 39. Surface rms roughness is decreased using fixed-modulated MME, as shown previously [27]. In this case, surface roughness was reduced from an

average of 21.2 nm for an unmodulated, droplet-free growth to an average of 6.08 nm for fixed-modulated MME growth, or a reduction by a factor of nearly 3.5. However, grain size was not highly affected by the use of fixed-modulation MME with GaN, as it was with AlN, and was even reduced in the case of sample (Fb). This is likely due to grain size being determined in the underlying AlN buffer layer and not sensitive to the GaN growth conditions. Nevertheless, this is consistent with the previous observations [27], since grain size did not significantly increase until the metal flux was significantly increased. When using smart-shuttering MME, however, the surface rms roughness was reduced to an average of 0.825 nm, a factor of 7.4 improvement over fixed-modulation MME, and a factor of 25.7 improvement over unmodulated growths. Furthermore, the grain size was significantly increased to an average of 189.5 nm for smart-shuttering MME, an average increase of 324 – 346% from the other growth techniques, supporting the hypothesis that smart-shuttering MME results in smoother morphologies.

## 7.7 Improved repeatability

Table 6 also shows the percent variation between the characterization values of samples grown with each technique. Due to the open-loop nature of the unmodulated and fixed-modulated MME growth techniques, growth rate varied by 21 – 24.5% as a result of high sensitivity to slight variations in the growth conditions. These same growth condition changes contributed to large variations in surface rms roughness (17 – 44%) and grain size (8 – 39%). However, using the closed-loop control technique of smart-shuttering MME, growth rate varied by less than 1%, surface rms roughness varied by less than 19%, and grain size varied by less than 1.6%, supporting the hypothesis of improved repeatability with smart-shuttering MME.

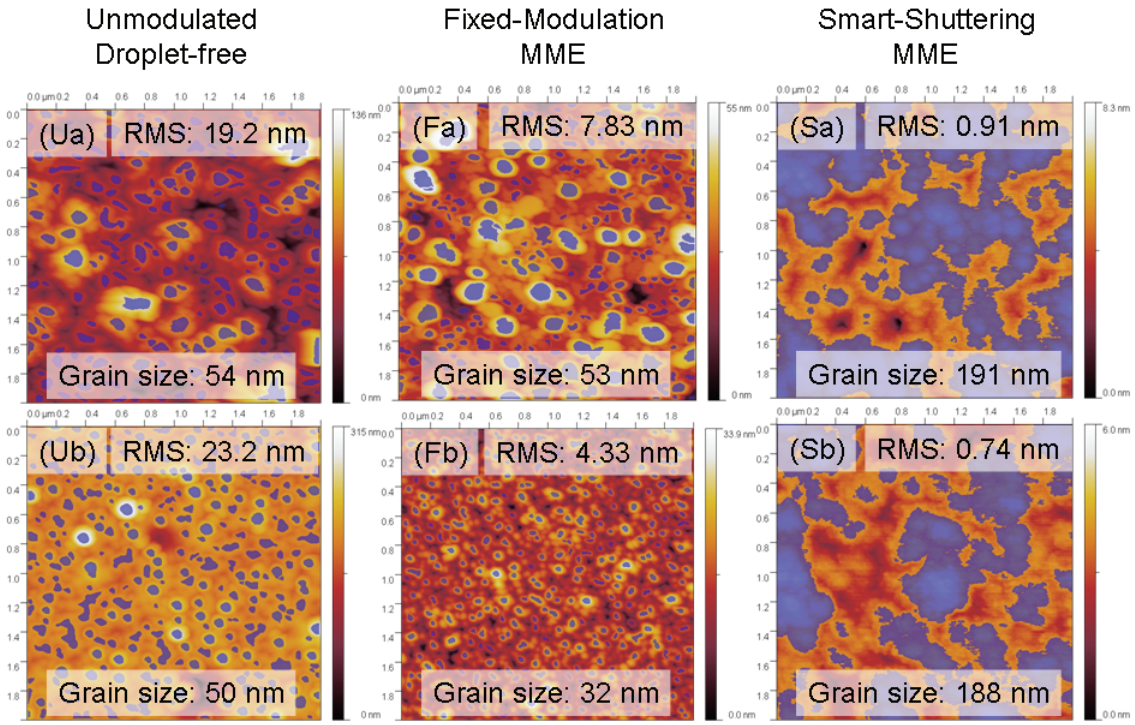


Figure 39: AFM images of unmodulated droplet-free samples (Ua, Ub), fixed-modulated MME samples (Fa, Fb) and smart-shuttering MME samples (Sa, Sb) with average surface rms roughness and average grain size shown. Grains are highlighted in blue (color online).

Table 6: Summary of characterization values for samples presented in Figure 39.

| Growth Condition | Unmodulated, droplet-free | | | Fixed-modulation MME | | | Smart-shuttering MME | | |
|---|---|---|---|---|---|---|---|---|---|
| Sample | Ua (N2268) | Ub (N2120) | % Var. | Fa (N2256) | Fb (N2362) | % Var. | Sa (N2379) | Sb (N2381) | % Var. |
| Growth rate (um/hr.) | 0.64 | 0.52 | 24.50 | 0.45 | 0.54 | 20.94 | 0.863 | 0.855 | 0.901 |
| AFM rms roughness (nm) | 19.20 | 23.20 | 17.24 | 7.83 | 4.33 | 44.70 | 0.91 | 0.74 | 18.68 |
| Average grain size (nm) | 54.00 | 50.00 | 8.00 | 53.00 | 32.00 | 39.62 | 191.00 | 188.00 | 1.57 |
| Grain size std. dev. (nm) | 11.40 | 9.08 | 25.55 | 13.70 | 3.10 | 77.37 | 166.00 | 111.00 | 33.13 |

## 7.8 Summary

Smart shuttering has proven to be a low-cost and low-complexity closed-loop real-time control system for MBE. Such a solution is necessary to increase the robustness of the epitaxial growth system. Smart shuttering is low-cost because it mainly uses existing MBE components such as RHEED feedback through a camera and motorized shutter controllers. The technique is easily implemented by monitoring two characteristics of the RHEED intensity signal: slope and standard deviation, making it a low-complexity solution as well. However, while it may be a low-cost and low-complexity solution, it yields powerful results. Significant improvements were observed for growth rate, surface roughness and grain size by using the smart-shuttering MME growth technique. Furthermore, these improvements were repeatable within a very low percentage compared to open-loop growth techniques. Future implementations could expand this approach to include PID control of the substrate or cell temperature to result

in consistent exponential time constants during growth, offering total control of the growing film. The robustness, improvements, low-cost and low-complexity of the technique make it an eventual indispensable part of MBE growth, as demand grows for MBE to meet requirements in each of these areas.

# CHAPTER 8: SMART-SHUTTERING MME APPLIED TO GAN WITH SI, MG AND IN

Incorporation of electrically active Mg acceptors into GaN or single phase In alloys into InGaN is sensitive to growth conditions, including substrate temperature and III – V flux ratio [21, 95, 141, 142]. Therefore, when growth conditions unintentionally change during growth or between growths, there is a corresponding unintentional change in the Mg doping of GaN or In composition of InGaN. Because of the narrow window of growth conditions needed for electrically active Mg-doped GaN, as described in Chapter 2, much of the problem with growing consistent material lies in growth condition variation. Likewise, inconsistent In composition of InGaN is a result of these same varying growth conditions. However, fixed-modulation MME offers some resistance to these variations by assuring growth is taking place in the droplet regime, and small variations within a regime should not be as drastic as variations between regimes. Smart-shuttering MME goes a step further by adjusting the shutter transitions based on the current flux, and is thus even more resistant to growth condition variation, which leads to more consistent growths. Therefore, these improvements should lead to subsequent incorporation improvements when growing GaN with Si, Mg and In. However, the shutter modulation technique may affect the way these atoms are incorporated into the GaN film, so it is important to experimentally test this hypothesis.

## 8.1 GaN with Si

Although Si-doped GaN is not as sensitive to variations in growth conditions, as is Mg or In, it is nonetheless important to determine the affect MME has on Si

incorporation. Samples were prepared for growth according to Appendix A. The substrate temperature was set to 550° C, and nitrogen plasma source flow rate was kept constant at 1.3 sccm for all growths, according to Appendix B. The Ga cell temperature was set to 990° C ($8.71\times10^{-7}$ Torr, BEP) for the smart-shuttering MME growths. The effects of smart-shuttering MME on Si doping were tested by growing a series of samples with the same growth conditions, but the Si effusion cell temperature was increased systematically from 1050° C to 1150° C. Figure 40 shows the results from the electrical characterization of Si-doped GaN samples grown with smart-shuttering MME using the standard parameters listed in Table 5. The lowest electron concentration attempted was with a Si cell temperature of 1050° C, which was $9.91\times10^{18}$ $cm^{-3}$, with a mobility of 13.15 $cm^2/Vs$, and a resistivity of 0.048 Ω·cm. The highest electron concentration achieved was with a Si cell temperature of 1150° C, which was $1.64\times10^{20}$ $cm^{-3}$, with a mobility of 20.78 $cm^2/Vs$, and a resistivity of 0.0018 Ω·cm. The electron concentrations achieved with smart shuttering are approximately an order of magnitude higher than previous recent Si-doping calibrations for the same growth system, shown in Figure 41, albeit on different substrates [143]. Therefore, it was concluded that smart-shuttering MME does not impede the efficiency of Si-doped GaN.

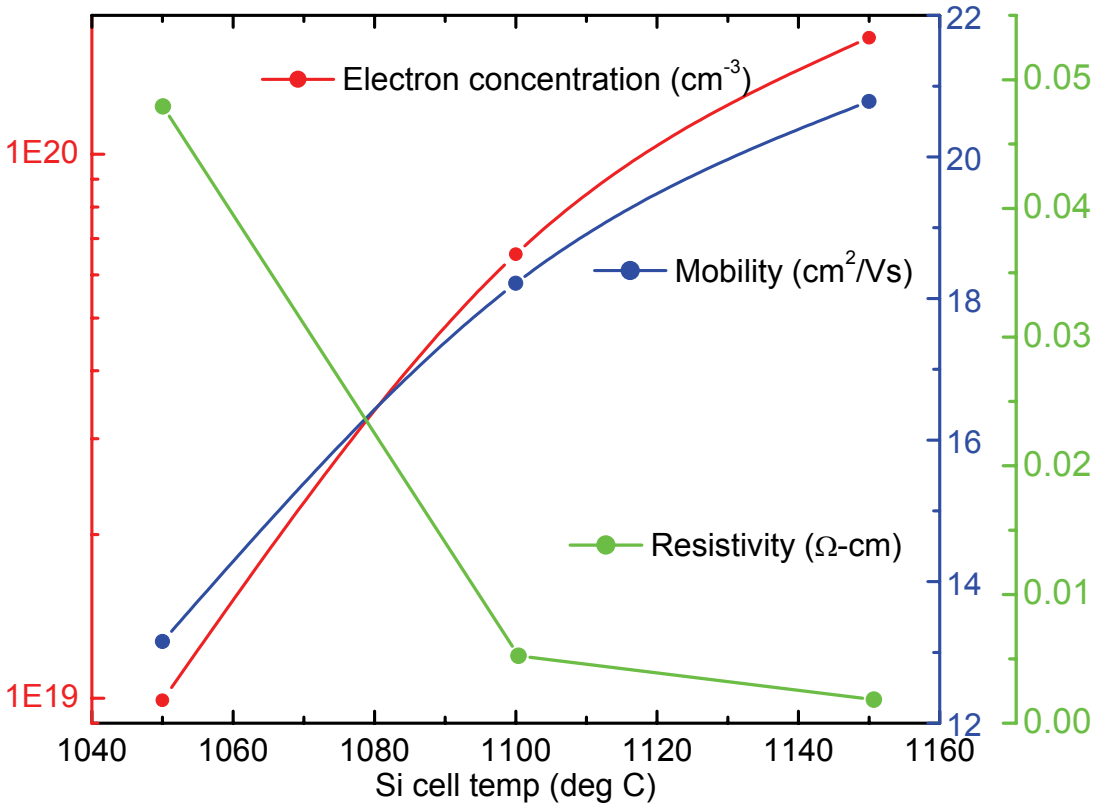


Figure 40: Electrical characteristics of Si-doped GaN using MME for different Si cell temperatures. The highest electron concentration was $1.64\times10^{20}$ $cm^{-3}$ (color online).

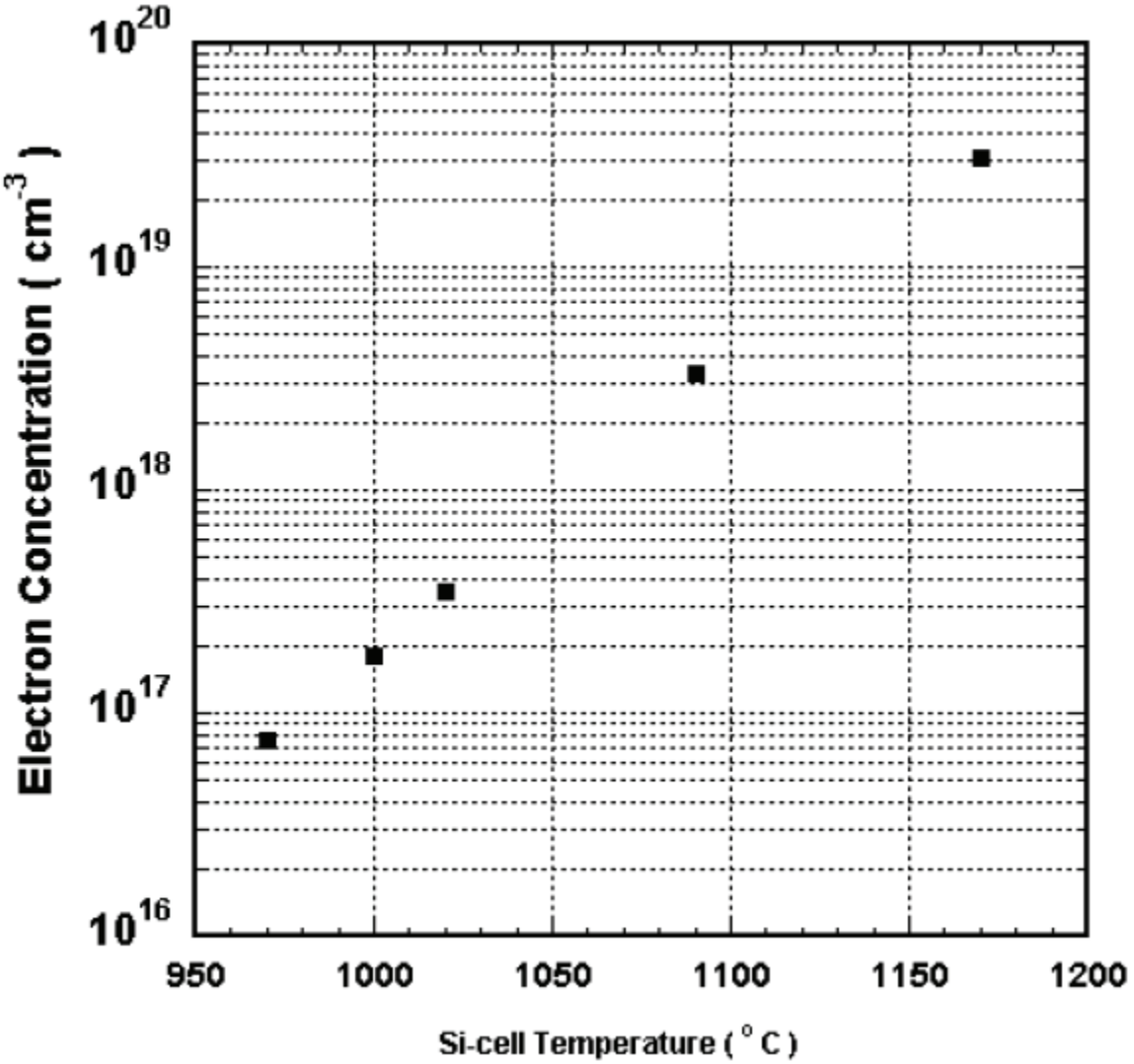

Figure 41: Electron concentration of Si-doped GaN grown on LGO as a function of Si cell temperature for unmodulated growths [143].

## 8.2 GaN with Mg

### *8.2.1 Growth and characterization conditions*

To observe the effects of MME on Mg-doped GaN, step profiles of Mg-doped GaN between layers of undoped GaN were grown, similar to that of Figure 24, for unmodulated Mg-doped GaN without droplets and smart-shuttering MME. The substrate temperature was set to 550° C, and nitrogen plasma source flow rate was kept constant at

1.3 sccm for all growths, according to Appendix B. The Ga cell temperature was set to 977° C ($4.43\times10^{-7}$ Torr, BEP) for the unmodulated growth, and to 990° C ($8.71\times10^{-7}$ Torr, BEP) for the MME growth. The Mg source with valved thermal tip was used, as described in Chapter 3. The Mg bulk temperature was set to 360° C, and the thermal tip was set to 900° C for both growths. The Mg valve was opened to positions of 20, 40, 60, 80, and 100 mils for the unmodulated growth, and to positions of 30, 60, 100, 150, 210, and 280 mils for the MME growth. The higher valve positions were used with the MME growth in anticipation of a lower Mg incorporation with a higher Ga flux [20]. These samples were then analyzed using SIMS according to appendix D.1, and the results are shown in Figure 42. A bulk Mg-doped GaN sample was then grown using MME to observe the uniformity of Mg doping with MME. All growth conditions were the same as the MME step-profile growth, with the exception of the Mg bulk temperature, which was at 330° C, and the Mg valve position, which was held constant at 100 mils. The SIMS depth profile for this sample is shown in Figure 43. Finally, a series of step-profile Mg-doped GaN samples were grown to narrow down the range of Mg doping that resulted in electrically active p-type GaN, according to the process outlined in Chapter 4. Then several bulk Mg-doped GaN samples were grown for electrical characterization using van der Pauw Hall measurements, as outlined in appendix C.1. The bulk samples that resulted in successful p-type doping used the same growth conditions as the step-profile MME sample, with the exception of the Mg bulk temperature, which was set to 290 – 300° C. The Mg valve position was then adjusted to obtain differing levels of Mg doping.

*8.2.2 Mg step-profile comparison and theoretical analysis*

For sample Mg1 in Figure 42, the Mg saturation limit [29] is exceeded above a valve position of 60 mils. Although it is well known that Mg incorporation decreases with increasing Ga flux [21, 95], the Mg saturation limit is exceeded above the same valve position for the MME growth (sample Mg2), which has a higher Ga flux. This may be a result of such a small change in Ga flux from sample Mg1 to Mg2. However, the peak concentration at the valve position of 60 mils is very different for the two growths. The peak Mg concentration is approximately $1.77\times10^{20}$ $cm^{-3}$ for sample Mg1, and approximately $7.55\times10^{20}$ $cm^{-3}$ for sample Mg2, an increase of over 320%. The peak concentration for Mg2 is approaching 2 atomic percent of GaN. However, Mg incorporation of this order of magnitude has not previously been sustainable throughout a film and has only been reported for a short depth [29]. This previous finding was supported by the subsequently higher Mg valve positions resulting in eventual lower Mg incorporations shown in Chapter 4. The delta-doping effect of the large Mg incorporation peak at valve position 60 could be a result of exceeding the 1.2 monolayer limit, causing the depletion of surface Mg through the formation of defects [65]. In that case, the defects would have changed the film polarity from Ga-polar to N-polar [66], which would cause subsequently lower Mg incorporation [18].

Furthermore, beyond the Mg saturation limit, both samples tend toward a saturated value of approximately $2\times10^{19}$ $cm^{-3}$, which has been previously reported for Mg doping above the saturation limit [29, 144]. However, the two samples approach the saturated value from different directions. Sample Mg1 drops from $1.77\times10^{19}$, to $8.08\times10^{19}$, to $2.54\times10^{19}$ $cm^{-3}$, while sample Mg2 rises from $1.44\times10^{19}$, to $1.56\times10^{19}$, to

$1.91\times10^{19}$ $cm^{-3}$. This difference is thought to be a result of an immediate and complete change in polarity for sample Mg2 following the delta-doping of Mg. Conversely, Mg1 is not thought to exhibit a complete polarity change after a valve position of 60 mils, but instead a gradual polarity change leading to a gradual shifting energy distribution of secondary ions [28], which thus leads to a gradual decrease in the measured Mg incorporation. Furthermore, the brief peak to the right of sample Mg2-peaks, at 100 and 210 mils, could also be a result of the depletion of Mg through defects [65], or could be the result of a brief buildup and then blocking of Mg by enhanced GaN growth through the Mg surfactant effect [29]. Finally, the second delta-doping of Mg for sample Mg2 at valve position 280 mils may be a result of reaching surface Mg concentrations so high that the Mg incorporation in the N-polar material nearly matches that of the previous delta doping peak in the Ga-polar material.

### *8.2.3 Higher incorporation with MME*

Below the saturation limit, the level of Mg doping is consistent between unmodulated and MME growths, and it is believed that all deposited Mg is either consumed or desorbed between MME cycles. However, at the saturation limit and above, there are drastic differences between the unmodulated and MME growths. It has been shown that Mg can form a stable structure on GaN at high Mg fluxes [64]. Therefore, if a Mg adatom is able to remain on the surface beyond the period of MME, the concentration of Mg will continue to build up to higher levels as MME proceeds. Eventually approximately 1.2 monolayers are built up on the surface, and the Mg is depleted from the surface through defects, similar to unmodulated growth [65]. However, with MME, this buildup and depletion can occur in the absence of Ga during the closed shutter

portion of MME. Therefore, with the source shutters closed and after Ga is consumed, the Mg is able to incorporate into the film through defects at much higher concentrations than if Ga were also being incorporated at the same time, and at much higher concentrations compared to Mg. This theoretical model, based on surface segregation and a desorption-limited mechanism, may also explain why Mg incorporation is not initially increased with higher Mg flux in Figure 24, since Ga flux is never interrupted and Ga adatoms are constantly saturating the surface, not allowing Mg to exclusively occupy the surface.

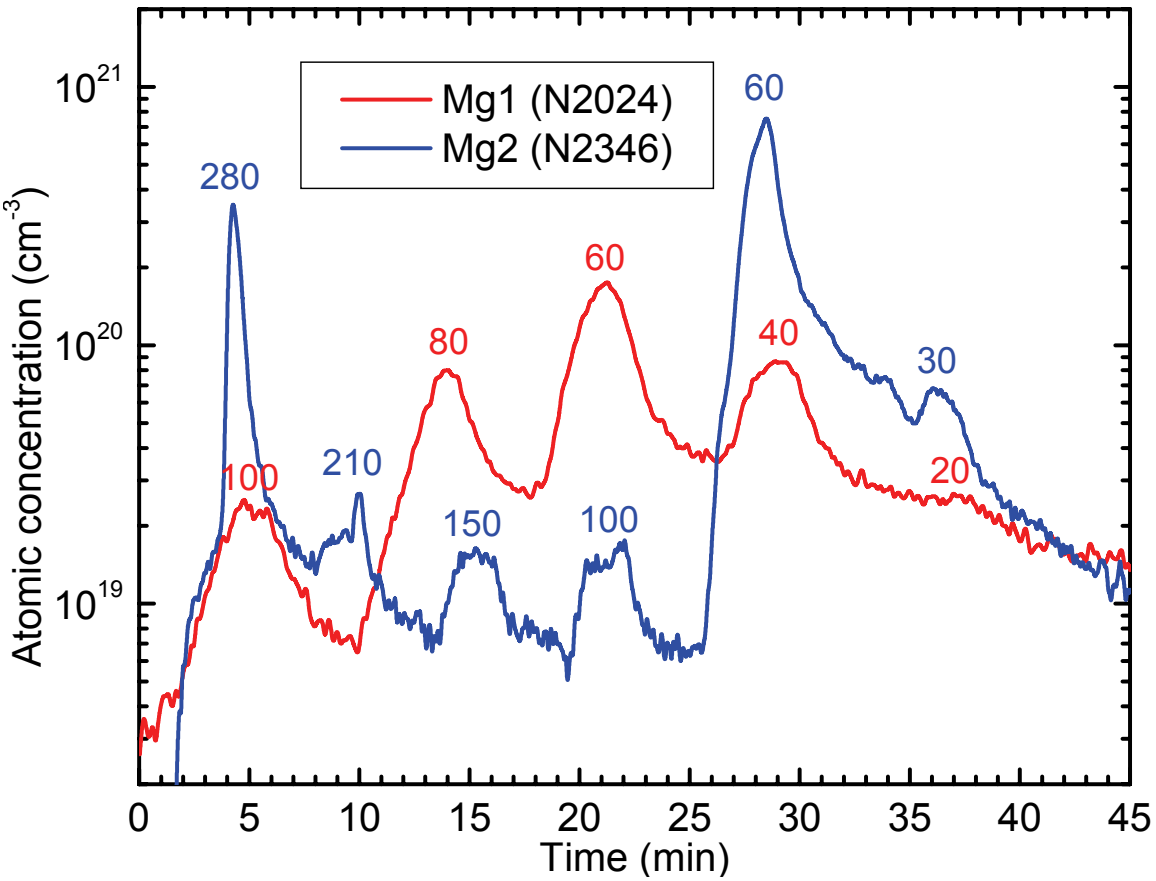


Figure 42: SIMS data for Mg-doped GaN step profiles for an unmodulated, droplet-free growth (Mg1), and a smart-shuttering MME growth (Mg2) with similar growth conditions. Note the much higher delta doping of Mg possible with MME, approaching two atomic percent (color online).

### *8.2.4 Mg incorporation consistency*

As stated, high Mg concentrations such as those for the delta-doping portions of sample Mg2 have not been previously sustainable [29]. However, Figure 43 shows a bulk Mg-doped GaN sample with a consistent Mg incorporation level of approximately $7\times10^{20}$ cm$^{-3}$. Unfortunately but as expected, the sample had a high resistivity of 7.77 Ω·cm and low mobility, which limited further electrical characterization of the sample. In the figure, the deviations at the extremities are due to non-steady-state surface effects

[119], and the mixing of secondary ion species at the matrix change (substrate interface) at approximately 0.4 μm due to a non-flat crater bottom. This sample serves to show the consistency of Mg doping when using the smart-shuttering MME technique, despite the non-steady-state nature of the shutter modulation approach.

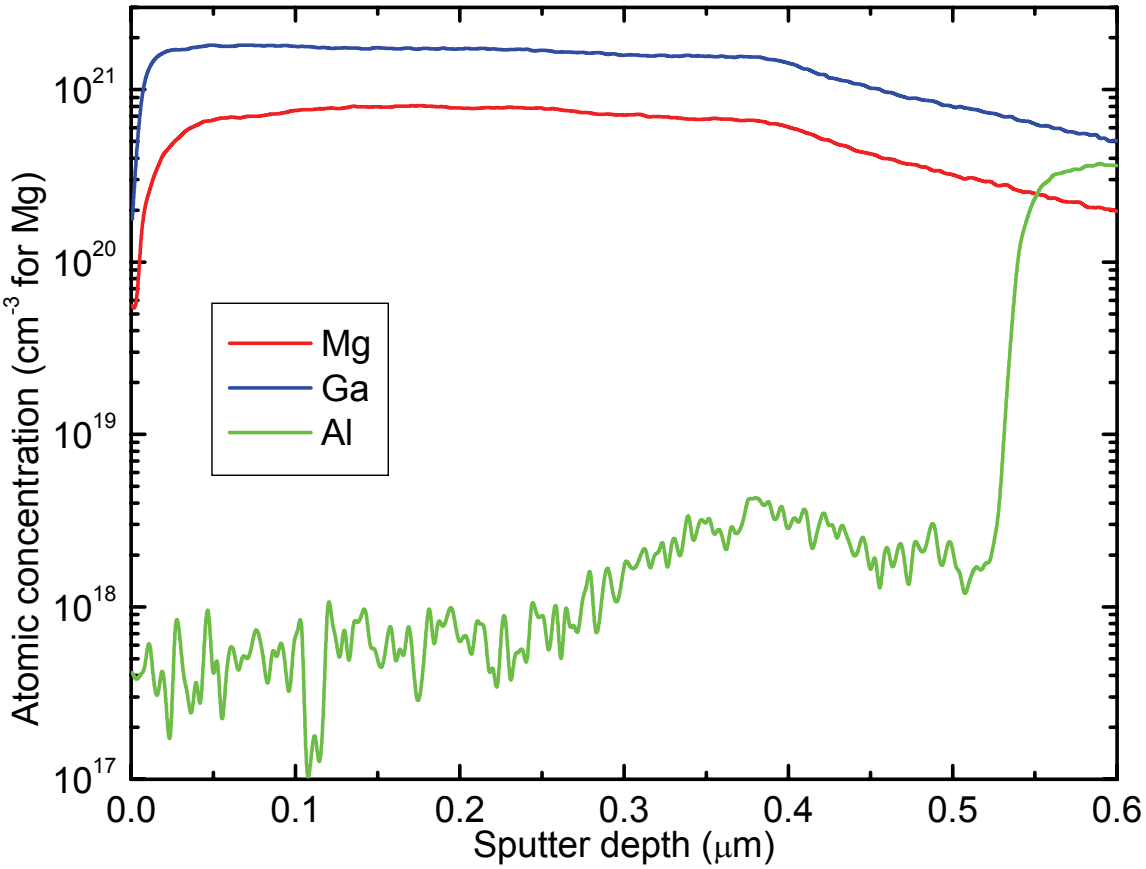


Figure 43: SIMS data for Mg-doped GaN sample with constant doping to illustrate uniform doping using the smart-shuttering MME growth technique with a high Mg incorporation. The average incorporation level of Mg is $7\times10^{20}$ $cm^{-3}$. Mg, Ga and Al signals mix at a depth of approximately 0.4 μm because of crater rounding at film interface (color online).

### *8.2.5 Electrical characterization*

Further optimization of the Mg-doped GaN MME growth process was done, and consistently electrically active p-type GaN was achieved, as shown in Table 7. Hole concentrations were obtained from $2.21\times10^{17}$ to $4.74\times10^{18}$ $cm^{-3}$. The lower concentration samples were grown with a Mg bulk temperature of 290 °C, with a valve position of 100 mils and exhibited a mobility of 9.73 $cm^2/Vs$, resistivity of 2.91 Ω·cm, and F factor of 0.85. The higher concentration sample was grown with a Mg bulk temperature of 300° C, a valve position of 100 mils and a substrate temperature of 500° C with an average mobility of 1.01 $cm^2/Vs$, resistivity of 1.31 Ω·cm, and F factor of 0.99. A strength of smart-shuttering MME lies in repeatability, thus the percent variation was found for two samples grown with the same target electrical characteristics. The percent variation for these two samples was 7.74% for hole concentration, 23.63% for mobility, 21.41% for resistivity, and 14.85% for the F factor.

Table 7: Values of lower and upper Mg-doped GaN carrier concentrations, with percent variation given for repeated samples.

| | Lower | Upper | % Variation |
|---|---|---|---|
| Hole concentration ($cm^{-3}$) | $2.21\times10^{17}$ | $4.74\times10^{18}$ | 7.74 |
| Mobility ($cm^2/Vs$) | 9.73 | 1.01 | 23.63 |
| Resistivity (Ω·cm) | 2.91 | 1.31 | 21.41 |
| F factor | 0.85 | 0.99 | 14.85 |

## 8.3 GaN with In

### *8.3.1 Growth and characterization conditions*

To observe the effect of MME growths on InGaN, sapphire samples were prepared as outlined in Appendix A, and growth conditions were systematically found that yielded unmodulated droplet conditions with approximately 1.3% In InGaN. These conditions included a substrate temperature of 550° C, a Ga cell temperature of 980° C ($6.76\times10^{-7}$ Torr, BEP), and an In cell temperature of 805° C ($2.65\times10^{-7}$ Torr, BEP). Smart-shuttering MME was then used with the same growth conditions, but with an increasing In flux for each subsequent sample, including 805° C ($2.65\times10^{-7}$ Torr, BEP) for sample In2, 822° C ($3.51\times10^{-7}$ Torr, BEP) for sample In3, and 835° C ($4.53\times10^{-7}$ Torr, BEP) for sample In4. Unmodulated, droplet-free growths were then grown to match the In composition of the initial droplet regime growth. This was accomplished with a Ga cell temperature of 960° C ($5.38\times10^{-7}$ Torr, BEP), and In cell temperatures of 780° C ($1.63\times10^{-7}$ Torr, BEP) for sample In5, and 750° C ($7.63\times10^{-8}$ Torr, BEP) for sample In6. The nitrogen plasma source flow rate was kept constant at 1.3 sccm for all growths, according to Appendix B. XRD was done on these samples, as outlined in appendix D.3, for comparison of In composition and the data is shown in Figure 44.

### *8.3.2 In composition*

Sample In1 was grown unmodulated within the droplet regime for an In composition of 1.28%. However, when using smart-shuttering MME with the same conditions, the In composition dropped to nearly 0% In, as seen for sample In2. Raising the In flux to nearly double the initial level had no consistent effect on the In composition when using MME, as seen for samples In3 and In4. To obtain droplet-free InGaN with

the same, or higher, In composition, the metal fluxes had to be reduced significantly. Samples In5 and In6 were grown unmodulated and without droplets for In compositions ranging from 1.3 – 5.5% In. Therefore, while MME may be beneficial for growth condition variance rejection, it was not possible to grow a significant In composition of InGaN using the technique since it uses metal rich conditions.

### *8.3.3 Theoretical analysis*

The explanation of this observation may be the opposite of why Mg is able to incorporate at such high levels with MME, and is related to a competition between In and Ga adsorbed atoms (adatoms) for available group-III sites. These experimental observations show Ga adatoms have a higher probability of occupying available group-III sites when in competition with In. However, sample In1 proves that when significant Ga and In are present, In is still able to incorporate, albeit at low concentrations. In other words, although enough Ga flux is present in this growth to occupy all available group-III sites, Ga does not always win the competition, and thus In is able to incorporate into the film. Nevertheless, when the abundant Ga and In are deposited in layers between equal periods of no metal deposition, as with MME, Ga nearly always wins the competition and occupies nearly all of the group-III sites. Because MME uses metal rich fluxes, the growth conditions effectively give the Ga atoms more time to displace In atoms during the shutter closed period. Furthermore, the residence time of In is exponentially shorter than Ga due to desorption rate differences, resulting in a nearly 100% Ga incorporation and correspondingly, nearly 0% In incorporation.

Indium has a high desorption rate at 550° C [141, 142], which makes incorporation near this temperature almost impossible with MBE [141]. However, since

a small In incorporation was achieved at this substrate temperature for samples In1, In5 and In6, the high desorption rate cannot be the only reason for the lack of In incorporation with MME, though it is probably significant. Therefore, it is believed that at steady state with an unmodulated growth with these growth conditions, the majority of In will desorb, but since In is constantly being supplied to the surface from the effusion cell, a small fraction of In is incorporated into the film. On the other hand, when using MME to create a period of no metal flux, steady state is never maintained, and nearly all of the deposited In is quickly desorbed upon shutter closing, while the excess Ga remains on the surface longer and is incorporated into the film. Thus, the result of growing with shutter modulation is a film with nearly 0% In, as observed with all MME samples. Nevertheless, shutter modulation within the N-rich regime may be beneficial for InGaN, and is suggested as a future research direction. Furthermore, the film color became brown and darker with increasing In flux when growing with MME. This may be a result of the increasing number of In adatoms blocking available group-III sites from the available Ga adatoms before the In adatoms eventually desorb from the surface, resulting in Ga-vacancies in the material [145].

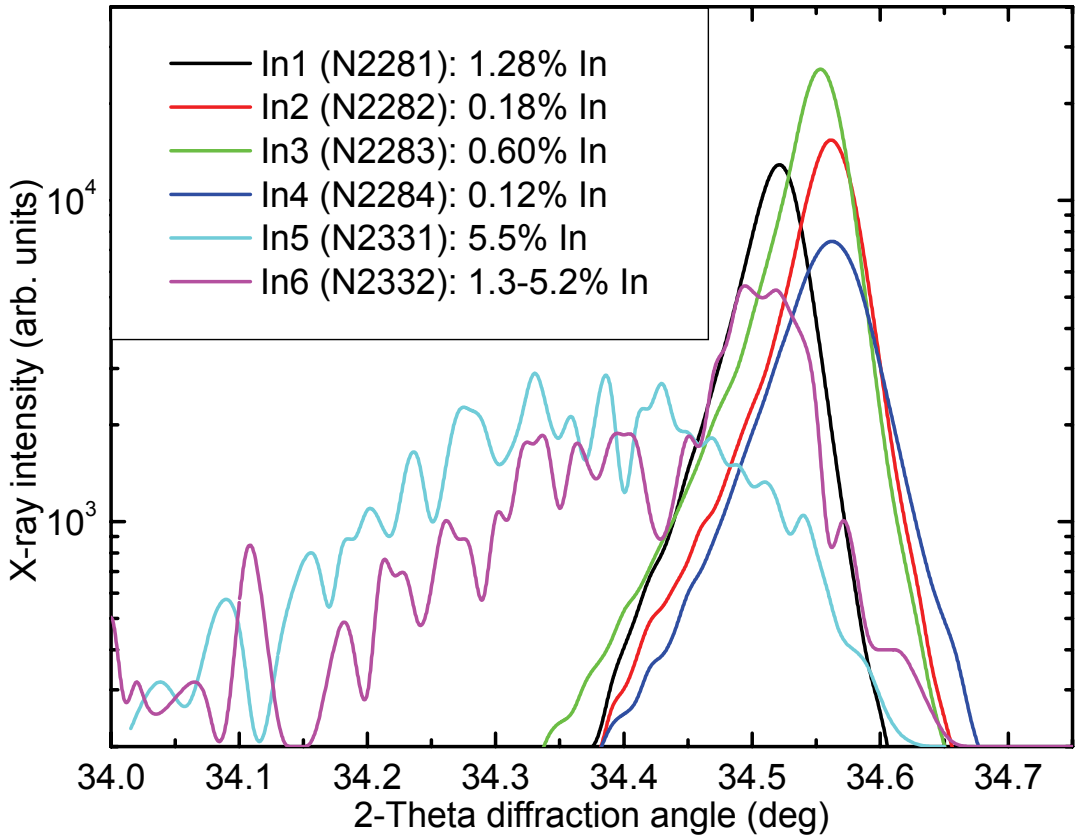


Figure 44: X-ray diffraction data for unmodulated InGaN with droplets (In1), MME grown InGaN (In2 – In4), and unmodulated InGaN without droplets (In5, In6). MME samples were grown with same conditions as In1, but with increasing In flux. Note the lack of response to the increased In flux for the MME samples. In5 and In6 were grown with lower Ga and In to avoid droplets, but to match the composition of In1 (color online).

## 8.4 Summary

Since MME offers the ability to grow droplet-free with metal-rich growth conditions, the effect of adding Si, Mg and In to the droplet regime growths was observed. Consistent Si-doped GaN was achieved with smart-shuttering MME, as high as $1.64\times10^{20}$ $cm^{-3}$. A substantially higher sustained concentration of Mg, approaching two atomic percent, was achieved using the MME technique versus other techniques, though the material was highly resistive. However, repeatable electrically active p-type

GaN was grown using smart-shuttering MME with lower Mg concentrations and hole concentrations from $2.30\times10^{17}$ to $4.74\times10^{18}$ $cm^{-3}$. The hole carrier concentrations were repeatable within 8% for identical growths using smart-shuttering MME, which is a significant improvement over traditional unmodulated reproducibility. While a significant amount of In composition was achieved in the droplet regime without shutter modulation, In incorporation was negligible when using MME. The high desorption rate of In coupled with the inherent transient surface adatom concentration was determined to be the cause of Ga overwhelmingly dominating the available group-III sites. Therefore, InGaN is not suitable for MME at these growth temperatures. While MME may not be suitable for InGaN, it has proven to be reliable for Si-doped GaN, and a significant improvement for Mg-doped GaN.

# CHAPTER 9: FUTURE WORK

The implementation of a closed-loop growth control system for MBE can be extended even further than smart-shuttering MME using other available inputs and outputs already on the systems. The available inputs of DMS and pyrometric interferometry, covered in Appendix F, could be used to complement the RHEED data for even better growth characterization. The outputs of source cell temperature (which controls the metal flux), nitrogen flow rate (which controls the nitrogen rf plasma flux), and substrate temperature could all be controlled using PID controllers for even better growth condition control. For example, using the exponential time constant extracted from the MME techniques, the source cell temperatures could be adjusted to maintain III – V ratios, and thus maintain consistent exponential time constant responses.

The issues of negligible In incorporation using MME can be addressed by attempting a few alternatives. First, since the desorption of In is a large contributor to the low In incorporation of GaN when using MME, this problem may be overcome simply by lowering the substrate temperature. Alternatively, growing thin layers of InN independent of GaN growth may allow for an aggregate InGaN composition. However, the thickness of these InN and GaN alternating layers must be thin enough to keep the carriers behaving as if the material were homogeneous. To accomplish this, the thickness of the layers must be low enough to satisfy superlattice properties. Fortunately, the MME technique has a native ability to grow alternating thin layers due to the shutter modulation approach.

Shutter modulation of the nitrogen source should also be explored. Because surface adatom migration was significantly improved by flooding the surface with the group-III metal, it is possible to further improve surface migration by removing the group-V source altogether when depositing the group-III source, much like the MEE technique. However, unlike MEE or MME, it may be beneficial to modulate only the nitrogen source in order to increase mobility. This alternative approach would be a Nitrogen Modulated Epitaxy (NME), rather than Metal Modulated Epitaxy (MME) technique. Thus, using the NME technique, the problems with growing InGaN may be overcome since the In source flux is never removed, and metal concentration on the surface can reach and maintain a steady state.

However, the current success of smart-shuttering MME can be used now to answer other unknowns of Mg-doped GaN. The nemesis of electrically active Mg-doped GaN is the compensating deep-level defects that act as recombination-generation (R-G) centers, trapping free hole carriers generated by the acceptors. The detection of these defects can be difficult, since the defect concentration can be as low as $1 \times 10^{14}$ impurities per $cm^3$ [146]. Figure 45 shows the sensitivity of various popular defect detection techniques. Of the techniques shown in the figure, the only technique that can detect the necessary low levels for analysis of defects in GaN doped with Mg, as well as the defect energy position in the band gap and the defect capture cross section [147] is deep-level transient spectroscopy (DLTS). Details of DLTS are covered in appendix C.2. Therefore, DLTS can be used to detect the deep-level defects that form as a result of Mg doping by analyzing films with increased Mg doping and observing which defects are correlated with the increase.

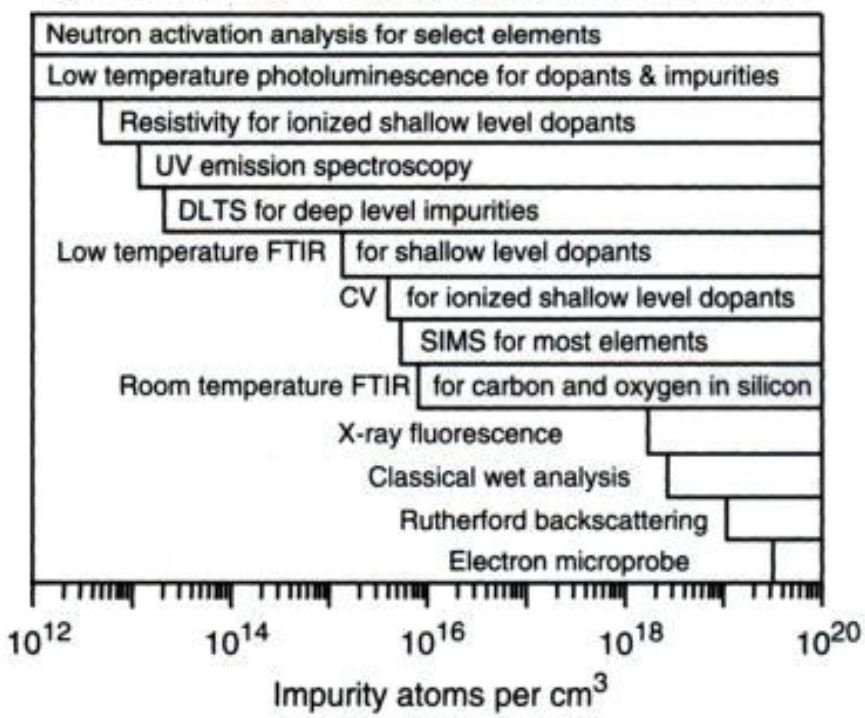

Figure 45: Summary of typical sensitivities of various impurity measuring methods [148].

Although DLTS on Mg-doped GaN has previously been performed by others [146, 147, 149-154], some studies only identified the activation energy of the Mg acceptors [150, 153], while others used only one level of Mg doping to identify various traps [146, 147, 149], which were not conclusively linked to Mg doping and could have been a result of other growth conditions, such as the use of hydrogen or oxygen [147]. Others went a step further to study the effects of different annealing or activation temperatures on Mg-doped GaN [151, 154]. No study has shown the development of the deep-level traps as a function of Mg doping to determine correlation and definitively assign responsibility to the Mg doping and not to other variables. The closest study to this idea included low Mg doping levels in *n-type* GaN to determine the effect on trap

levels near the *conduction* band [152] and was only done for two levels of Mg doping, thus is considered a largely unrelated study. Furthermore, none of these studies were done using a traditional MBE system and suffered from unintentional dopants from precursors and carrier gases. Therefore, it would be beneficial to conduct an experiment of DLTS measurements on MBE grown GaN pn diodes with increasing Mg dopant concentration to correlate trap levels with increasing Mg concentration. This experiment would for, the first time, allow the measurement of the dominant, electrically active, deep-level defects formed by increased Mg doping in GaN using DLTS. However, since consistent Mg-doped GaN was a limiting factor, this can now be overcome by using smart-shuttering MME and the experiment is now possible.

To prepare samples for the DLTS experiments, a series of GaN $pn^+$ diode structures should be grown with the same growth conditions, but with varying Mg concentrations. Before MME, the ability to grow Mg-doped GaN with tightly controlled Mg concentrations was not feasible. However, these samples can now be grown in an MBE chamber, where previously covered growth [22, 112], optimization [20, 23] and characterization techniques could be used to minimize unintentional variation. However, in order for the DLTS experiment to extract data only from the p-type side of the pn diode, pn junction depletion width calculations must be done. The equations for the n- and p-side depletion widths are given as [43]

$$X_n = \sqrt{\frac{2K_s\varepsilon_0}{q}\frac{N_a}{N_d\left(N_a+N_d\right)}\left(V_{bi}-V_a\right)} \tag{26}$$

and

$$X_p = \sqrt{\frac{2K_s\varepsilon_0}{q}\frac{N_d}{N_a\left(N_a+N_d\right)}\left(V_{bi}-V_a\right)}, \tag{27}$$

where $X_n$ and $X_p$ are the depletion width on the n- and p-side, respectively, $K_s$ is the semiconductor dielectric constant, $\varepsilon_0$ is the permittivity of free space, q is the charge of an electron, $N_a$ is the concentration of free hole carriers, $N_d$ is the concentration of free electron carriers, $V_{bi}$ is the built-in potential of the junction, and $V_a$ is the applied voltage to the junction. Figure 46 shows solutions to these equations for a fixed $V_a$ of -7 V with varying carrier concentrations, and also for fixed carrier concentrations with varying $V_a$. Using smart-shuttering MME, the highest hole carrier concentration was approximately $1\times10^{18}$ $cm^{-3}$, and the highest electron carrier concentration was over $1\times10^{20}$ $cm^{-3}$. Therefore, these values were used to determine the depletion width of the p-side at various applied voltages, as seen with the red curve in Figure 46. From this data, a Mg-doped GaN film with a hole concentration of $1\times10^{18}$ $cm^{-3}$ can be fully depleted at a reversed bias potential of -7V if the film is less than or equal to 0.1 μm, which defines the target thickness of the Mg-doped GaN film grown on a Si-doped GaN layer.

The blue and green curves in Figure 46 show the behavior of the n- and p-side depletion widths as a function of carrier concentration with a fixed applied bias voltage of -7 V. The green curves show data for varying $N_d$, and $N_a$ fixed at $1\times10^{18}$ $cm^{-3}$. At the target level of $N_d = 1\times10^{20}$ $cm^{-3}$, it is clear that the n-side depletion width is negligible compared to the p-side depletion width. Furthermore, the blue curves, which show data for varying $N_a$ with $N_d$ fixed at $1\times10^{20}$ $cm^{-3}$, verify that the p-side will completely deplete a 0.1 μm Mg-doped GaN film for hole carrier concentrations less than $1\times10^{18}$ $cm^{-3}$, with a negligible depletion width on the n-side. Therefore, by using the tools presented in this dissertation, it is possible to perform this experiment using DLTS.

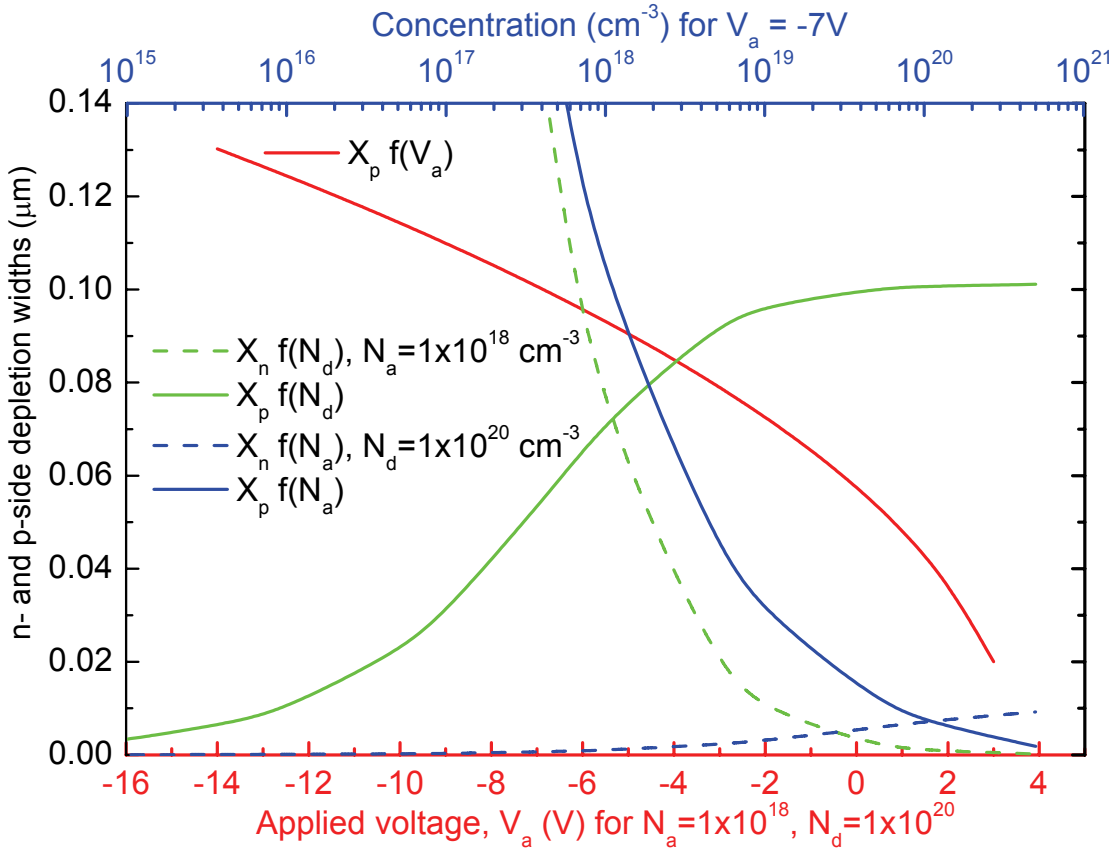


Figure 46: n- and p-side depletion width calculations for varying applied voltage, $V_a$, and varying dopant concentration, Na and Nd. Target doping concentrations for the pn diodes to be used in the DLTS experiment can be obtained with this figure (color online).

# CHAPTER 10: CONCLUSIONS

By increasing the understanding of Mg-doped GaN through an exhaustive review of current limitations, increased control over the material was achieved by addressing several of these issues. The review of Mg-doped GaN found that the material suffered from a low solubility of Mg into GaN [11], a tendency of Mg to accumulate and segregate at surfaces [18], a memory effect of Mg in a growth chamber [16, 17], a high vapor pressure of Mg at low temperatures [15], a low sticking coefficient of Mg on GaN, a deep ionization energy of Mg acceptors in GaN [19], unintentional hydrogen and oxygen doping [86, 88], a significant compensation of Mg acceptors at high dopant concentrations [11], and a drastic dependence upon the growth regime or III – V ratio [21]. As these issues were addressed, repeatable and reliable Mg-doped GaN became a reality using the tools and techniques developed as a result.

To address the memory effect [16, 17], low sticking coefficient and high vapor pressure of Mg [15], a new Mg dopant source was characterized and modeled for p-type doping of GaN with PAMBE [20-23]. The device, which was much like a traditional effusion cell with a valved thermal tip, enhanced the sticking coefficient by energizing the outgoing Mg flux. The first reported demonstration of an abrupt junction between two non-zero Mg-doped GaN films, and first reported demonstration of a graded Mg-doped GaN film were also achieved using this new Mg-dopant source.

The significant compensation of Mg acceptors at high dopant concentrations [11] was used advantageously to develop a new *ex situ* resistivity analysis technique using SIMS to characterize doping of buried layers [28]. The new technique works by

monitoring changes in the energy distribution of host atom secondary ions during a SIMS depth profile. By analyzing a film with increased Mg doping, the barrier between conductive Mg doping and resistive Mg doping was identified, and Mg-doped GaN could be optimized.

Because Mg doping exhibits a drastic dependence upon the growth regime or III – V ratio [21], a new growth and regime characterization technique was developed using RHEED [24, 25]. The technique uses specific RHEED intensity responses to metal source shutter transitions to define each growth regime. These intensity responses include exponential drops and oscillations upon shutter opening, and delay periods upon shutter closing. The time constant of the exponential drops can be used to repeat growth conditions, and the delay period can be used to determine the existence of droplet buildup. These new in situ growth indicators can be used to assure III – V ratio or growth regime for Mg-doped GaN for repeatable growths. During the development this technique, a new surface kinetics growth model for III-nitrides based on DMS observations was discovered [155]. This model suggests a cation-anion exchange process initially upon metal shutter opening and a preferential buildup of the metal bilayer before growth begins, and may apply to all III-nitrides that exhibit a bilayer, which is important for Mg-doped GaN because of surface segregation issues [18].

Using the new RHEED growth and regime characterization technique, a new growth technique called metal modulated epitaxy (MME) was developed [26, 27]. MME was determined to increase repeatability, uniformity and smoothness of PAMBE grown films. This was accomplished by growing with conditions that would normally lead to droplets, but modulating the shutter to allow enhanced migration of the metal adatoms for

improved lateral growth. As a result the window of growth conditions which lead to intermediate-like morphologies was expanded (allowing more error toleration), rms roughness was halved, and grain size grew by as much as 245%. Because several reports indicate successful Mg-doped GaN for Ga-rich growths [18, 82], this new technique offers the certainty to grow smooth films in the Ga-rich regime for more successful Mg-doped GaN.

The MME technique was enhanced with a closed-loop control using real-time feedback from RHEED transients to control shutter transitions. This enhancement, called "smart shuttering," is a low-cost and low-complexity closed-loop solution with powerful results. Growth rate was improved over the standard MME technique by nearly 60% by reducing the shutter-closed time to a minimum. Surface roughness was reduced to less than 1 nm rms, an improvement factor of up to 25.7 over unmodulated growth. Grain size was increased by over 300% using smart-shuttering MME to an average diameter of nearly 200 nm compared to unmodulated growth. Moreover, values were repeatable within 1% for growth rate, 19% for roughness, and 2% for grain size. The smart shuttering extension to MME allows the repeatable growth of high surface quality Mg-doped GaN.

Effects of MME were observed with Si, Mg and In during GaN growths. GaN was successfully doped with Si for a range of electron carrier concentration from $9.91\times10^{18}$ – $1.64\times10^{20}$ $cm^{-3}$, with low resistivities, from 0.048 – 0.0018 Ω·cm. Repeatable Mg-doped GaN was achieved with a variation of less than 8%, and a peak hole carrier concentration of $4.74\times10^{18}$. However, no appreciable amount of In was

incorporated when attempting to grow InGaN using MME. This was thought to be a result of a high desorption rate of In at the substrate temperature.

In summary, by understanding the limitations of Mg-doped GaN, tools and techniques for increased control were developed to address these issues. These tools and techniques culminated with the achievement of reproducible Mg-doped GaN, which substantiated their importance. However, with many GaN applications not being developed further due to inconsistent Mg-doped GaN, this achievement is only the beginning. The applications that will most notably benefit from this achievement include all those based on the pn junction, such as LEDs or other photo emitters, and solar cells or other photo detectors. The consistency offered by the presented techniques may be all that is necessary to push the development of GaN-based applications further.

# APPENDIX A: PRELIMINARY GROWTH PROCEDURES

## A.1 Substrate cleaning and preparation

To maintain high purity in the growth environment and minimize contamination, all samples were chemically cleaned to remove organics before entering the vacuum system. Initially, this process was a degreasing step involving soaking the samples a minimum of five min each in trichloroethylene (TCE), acetone and methanol while in an ultrasonic bath. However, when MOCVD or HVPE GaN templates were used other cleaning methods were explored. Figure 47 clearly shows advantages of other cleaning methods over a simple degrease cleaning [156]. Since the removal of carbon was the goal of the cleaning, the level of surface carbon contamination was used to evaluate the cleaning methods. The best results were found for GaN cleaned with a hot piranha etch, which consists of a 4:1 mixture of $H_2SO_4$:$H_2O_2$ heated to approximately 90° C, followed by a vacuum anneal [157]. Initially, dirty photo-resist-coated samples were chemically cleaned for 30 minutes in the hot piranha etch. However, after this initial one-time cleaning step, the samples could be vacuum-ready by another etch in the hot piranha etch in as little as 10 min [157, 158]. The samples were then treated as they would have been with the previous degreasing cleaning. They were rinsed with de-ionized (DI) water, dried with a nitrogen spray gun and mounted onto a Veeco UNI-block sample holder with custom-made molybdenum (Mo) retaining rings and spring plates.

To further clean the samples they were then loaded into the high-vacuum introduction chamber, where they were outgassed. The previous degreasing cleaning used an outgassing step at 700° C for one h. However, in the studies by Liu and

Machuca, only a 10 min outgassing step was required to remove surface carbon contamination [157, 158]. Furthermore, it has been suggested that ammonia may help in the cleaning during anneal. In contrast, The study by Machuca shows that a vacuum anneal without ammonia yields better results [158]. Table 8 shows the effect of annealing the samples in both ammonia and vacuum at various temperatures. As shown, the best results were observed for a vacuum anneal at 700° C for 10 min [158]. Figure 48 shows the different electronic structures of the surface near the carbon 1*s* energy by synchrotron radiation. The reduction of carbon can clearly be seen in this image as the sample is chemically cleaned and then vacuum annealed, reducing the carbon to background levels. Furthermore, Figure 49 shows similar data for the Ga 3*d* and N 1*s* energies, which show an improved GaN surface using the cleaning and annealing technique by more narrow and higher intensity peaks.

To verify the result of the chemical cleaning, Energy-dispersive x-ray spectroscopy (EDS) measurements were done on three pieces of the same sample coated with photoresist. The first piece still had photoresist coated on the surface. The second sample was cleaned using the degreasing method. The third sample was cleaned using the hot piranha etch for 10 minutes. Figure 50 and Table 9 show the result from the EDS scans, and verifies the superiority of the hot piranha etch to traditional degreasing cleaning. Appendix D.5 gives more information on the EDS system and process used in this experiment. Thus, the 10 min hot piranha etch followed by a 10 min anneal in vacuum was adapted as the cleaning method for subsequent growths in the presented experiments. The only caveat of this method is that the hot piranha etch is known to etch many metals, such as Mo, which is commonly used as a backside metal for sapphire.

However, the surface cleaning technique had no affect on Ta, so it was used as the backside metal in the experiments.

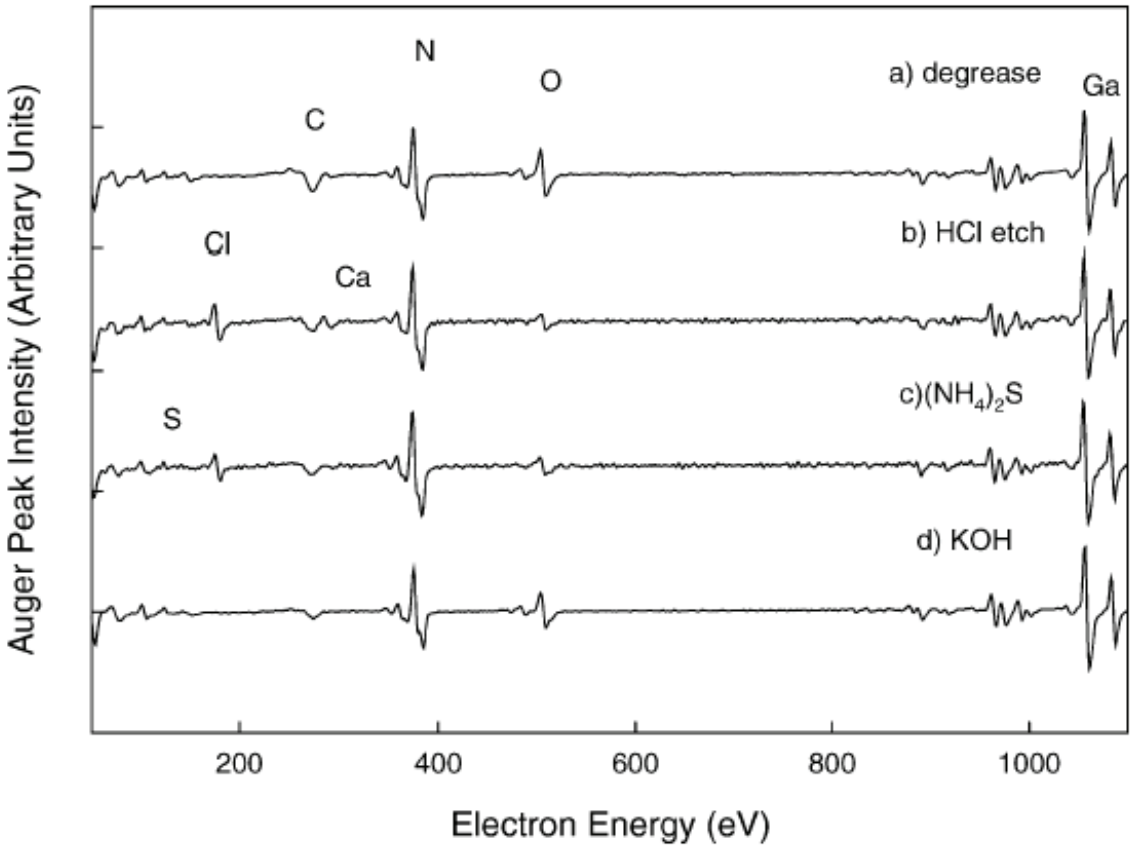


Figure 47: AES surface scans of GaN cleaned as indicated [156].

Table 8: Concentrations of oxygen and carbon, expressed in monolayers, on the surface of GaN following immersion in a mixture of 4:1 sulfuric acid to hydrogen peroxide and annealing at 10 min at the temperature indicated. The ammonia pressure was 2 μTorr. Note the effectiveness of the vacuum anneal for reducing the concentration of oxygen and carbon [158].

| Temperature° C | | 25 | 590 | 636 | 700 | 740 |
|---|---|---|---|---|---|---|
| Ammonia anneal | [O] | 1.51 | 0.47 | 0.39 | 0.48 | 0.37 |
| | [C] | 0.32 | 0.23 | 0.13 | 0.01 | 0.01 |
| Vacuum anneal | [O] | 0.91 | 0.34 | 0.27 | 0.08 | 0.11 |
| | [C] | 0.74 | 0.14 | 0.05 | 0.01 | 0.01 |

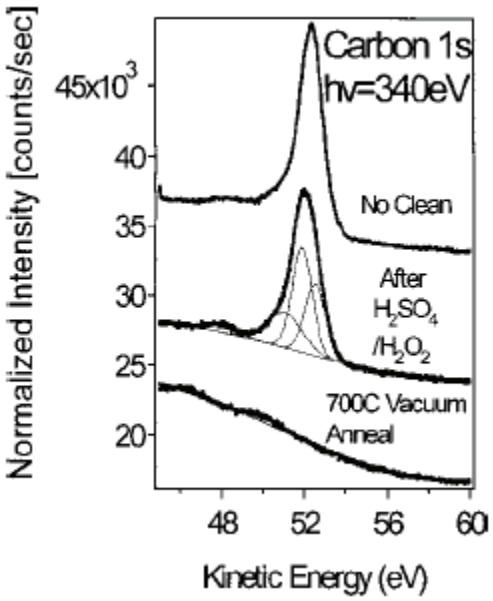


Figure 48: Electronic structure of surface using synchrotron radiation. Surface before the clean is seen in the top curve, the corresponding coverage is one monolayer approximately. The middle curve shows four chemical states of the carbon 1*s* feature after the 4:1 sulfuric acid to hydrogen peroxide solution, $CO_3$, $CO_2$, CO, and $CH_x$ species, from lowest to highest kinetic energy, respectively. The starting carbon content is 70% oxides of carbon (middle curve). Then after the 700° C anneal in vacuum (bottom curve), the total carbon content is reduced near the background, estimated at the sensitivity of the measurement, ≈ 1% of a monolayer [158].

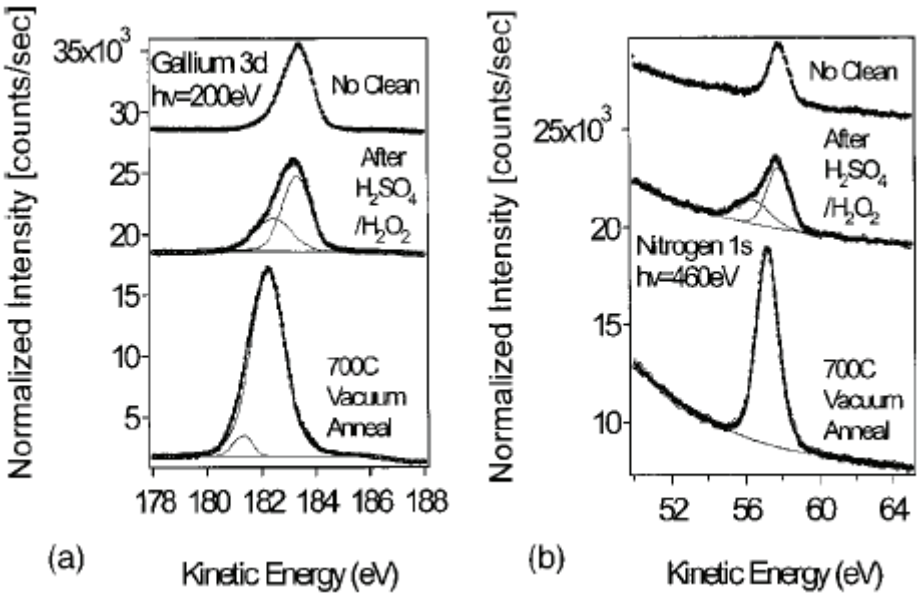


Figure 49: (a) Ga 3*d* core level before the immersion in 4:1 sulfuric acid to hydrogen peroxide (top curve), after immersion in the cleaning solution (middle curve), and after the thermal anneal at 700° C (bottom curve). The middle curve shows the chemical shift of the gallium oxide component by 0.8 eV toward lower kinetic energy with respect to the bulk GaN peak. The bottom curve shows the cleanest Ga 3*d* spectrum, with a minor low kinetic energy feature corresponding to the residual oxygen on the surface, estimated to be less than 10% of a monolayer. (b) N 1*s* core level is similarly shown before (top curve) and after (middle curve) the 4:1 sulfuric acid to hydrogen peroxide, and after the 700° C thermal anneal in vacuum (bottom curve). There is a low kinetic energy feature after immersion in the solution (middle curve), suggesting chemisorption of oxygen onto nitrogen sites, removed by a 600° C anneal.

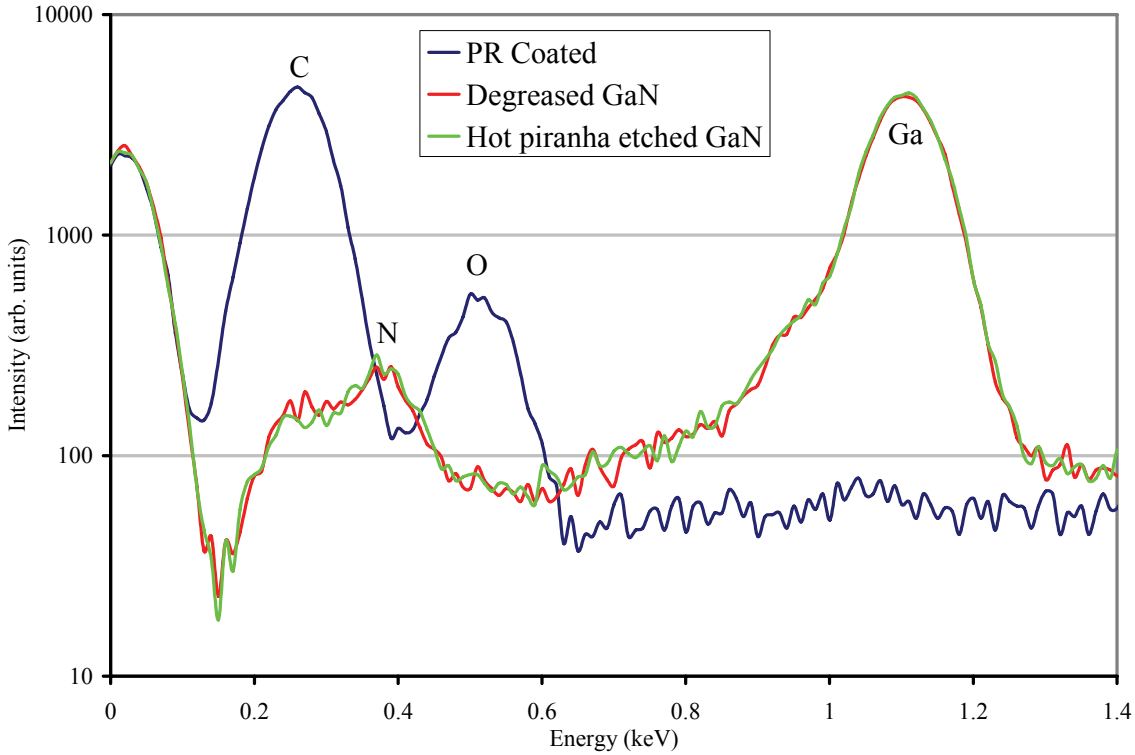


Figure 50: EDS results for GaN coated with photoresist, cleaned with degreasing method, and cleaned with hot piranha etch (color online).

Table 9: EDS results from Figure 50 for GaN coated with photoresist, cleaned with degreasing method, and cleaned with hot piranha etch. Note the superiority of the hot piranha etch over the traditional degreasing cleaning method.

| Atomic Percent | % C | % O | %Ga | %N | Ga/N Ratio |
|---|---|---|---|---|---|
| PR-Coated GaN | 82.28 | 16.77 | 0 | 0 | N/A |
| Degreased GaN | 47.65 | 0 | 35.04 | 15.47 | 2.26 |
| Piranha GaN | 28.29 | 0 | 23.12 | 47.78 | 0.48 |

## A.2 Buffer layer growth

To minimize the adverse effects of mismatch, low-temperature nitridation and high-temperature AlN buffer layers were grown before growing the GaN films [35]. Nitridation of the sapphire substrates was done at 200° C and a nitrogen flow rate of 0.35

sccm (sccm denotes cubic centimeters per min at standard temperature and pressure) for one h. The AlN buffer layer was grown at 800° C with the same nitrogen flow rate for 20 min for a relatively thin, approximately 100 nm, film.

The low-temperature nitridation and high-temperature AlN buffer layer were initially modeled after the work by Namkoong et al. [35]. However, after the development of MME, described in Chapter 6, the AlN was grown using this new technique for better surface smoothness. The new technique used a higher Al flux, with a Al cell temperature of 1150° C ($3.85\times10^{-7}$ Torr, BEP), and a fixed modulation of 10 seconds for the shutter closed and open time. All other growth conditions were the same, with the exception of the nitrogen flow rate upon plasma aperture change, as described in Appendix B. This resulted in a growth rate of approximately 0.521 μm per h. Therefore, for a target thickness of 100 nm, the AlN film was grown for approximately 12 minutes.

# APPENDIX B: PLASMA APERTURE

The plasma aperture was originally a standard 253 hole PBN plate. However, the uniformity was quite poor due to the relatively short source-to-substrate distance and the normal angle of the drilled holes, as seen in Figure 51, Figure 52, and Figure 53. According to these estimates, the total non-uniformity across at two-inch wafer was 77.7% [159]. Therefore, calculations were done by Rich Bresnahan of Veeco Instruments, Inc. to suggest alternate aperture designs for improved uniformity. The discussion of the plasma aperture design is included in this appendix for completion and since the result highly affected the growth conditions of the experiments in the text.

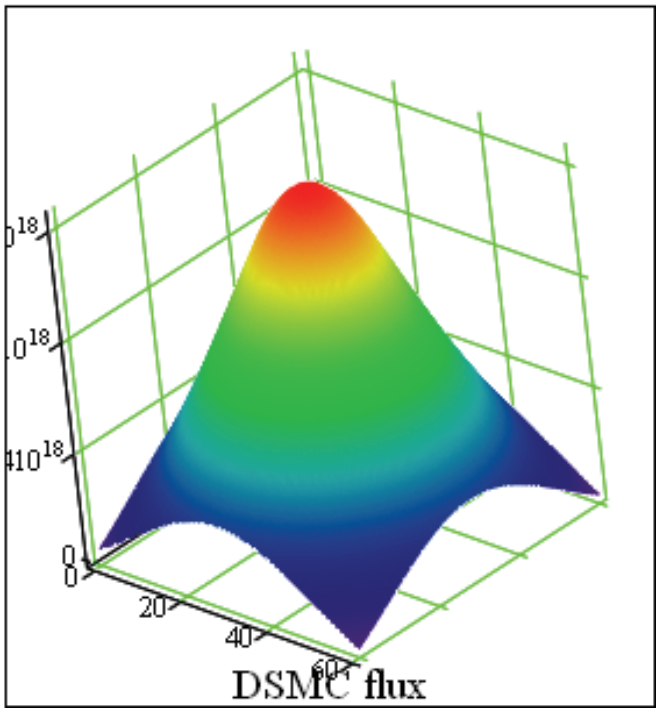


Figure 51: 3D Plot of Flux in Substrate Plane (x and y axis are arbitrary units equating to +/- 1" in the substrate plate: 30,30 = Center of the wafer) (color online) [159].

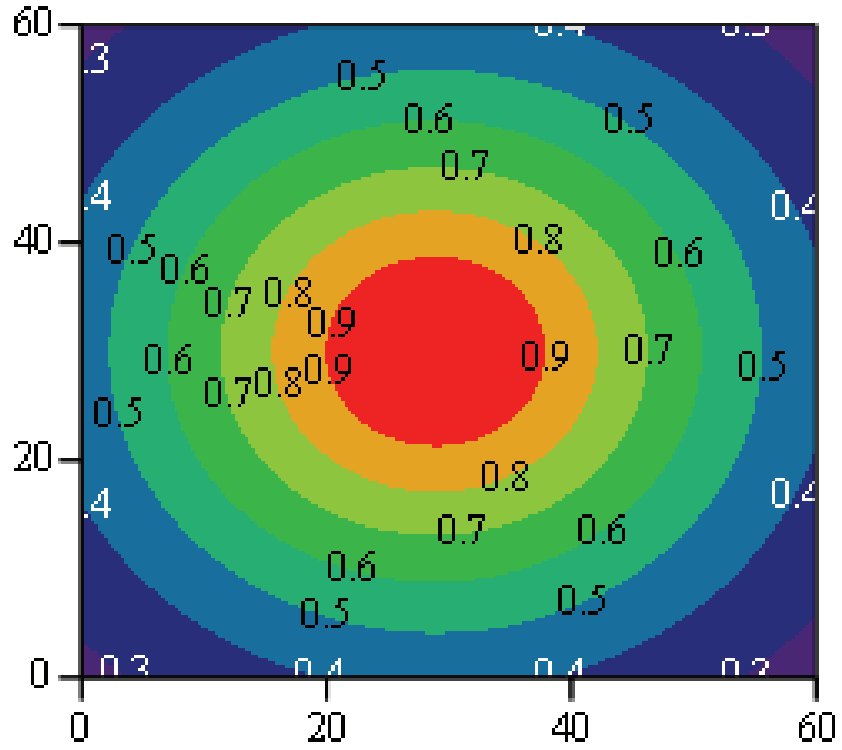


Figure 52: 2D Plot of Flux in Substrate Plane (x and y axis are arbitrary units equating to +/- 1" in the substrate plate: 30,30 = Center of the wafer) (color online) [159].

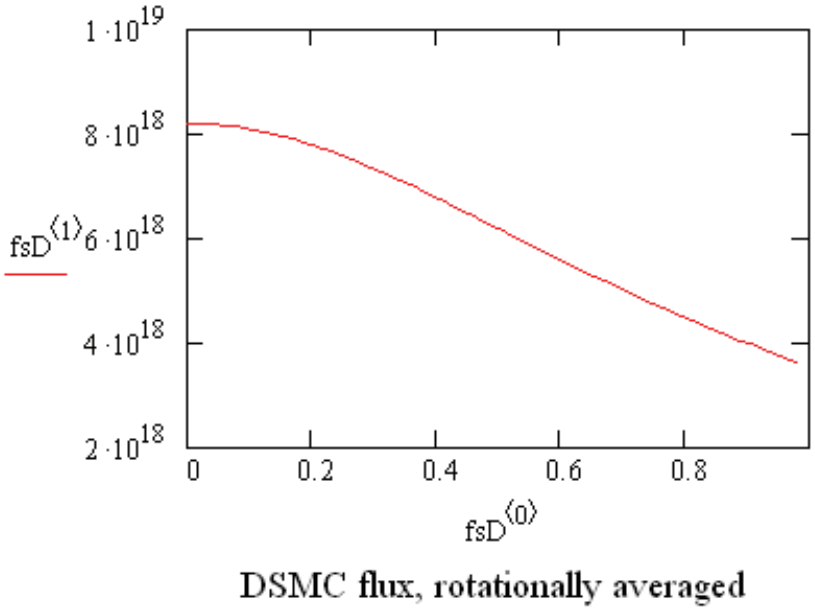


Figure 53: Rotationally Averaged Flux in Substrate Plane (x axis in radial inches) (color online) [159].

However, a more uniform growth was desired, and a new aperture plate was designed by Veeco Instruments. The new aperture plate featured holes drilled at an angle, rather than normal to the surface. The number of holes was increased from 253 to 712 to maintain the original nitrogen flux per square and maintain the same growth rate over the entire sample. This required a flow increase by a factor of 2.8, or from 0.5 to approximately 1.4 sccm. In practice, the necessary flow rate was determined to be 1.3 sccm. As shown in Figure 54, Figure 55, and Figure 56, the total non-uniformity over a 2" wafer for this design is 5.2% [159]. The new plasma aperture was used for the smart shuttering, Mg, and In MME studies.

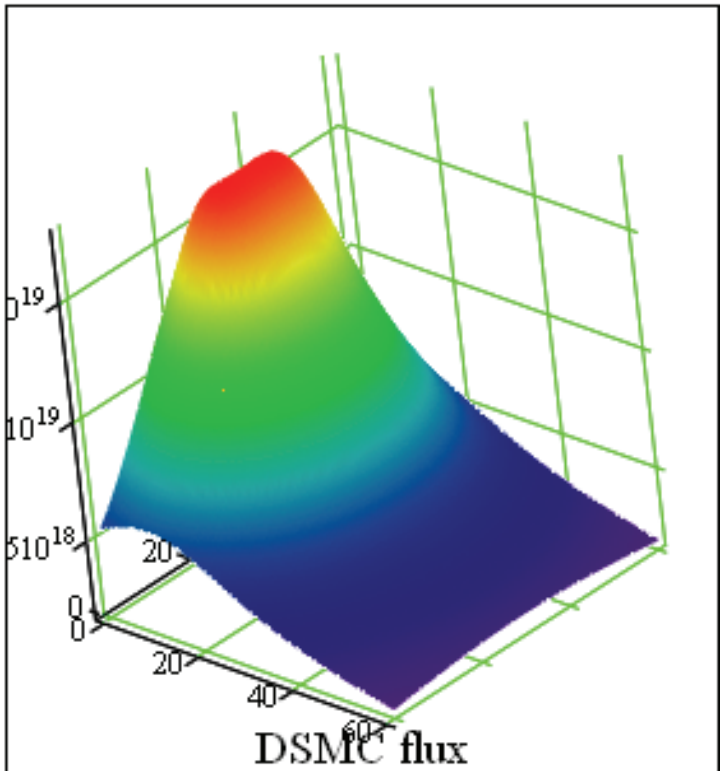

Figure 54: 3D Plot of Flux in Substrate Plane (x and y axis are arbitrary units equating to +/- 1.5” in the substrate plane: 30,30 = Center of the wafer) (color online) [159].

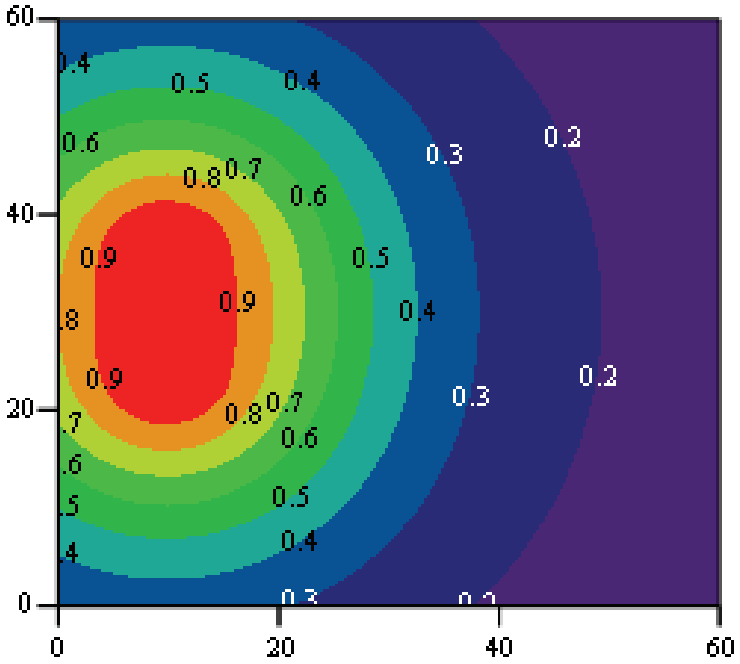


Figure 55: 2D Plot of Flux in Substrate Plane (x and y axis are arbitrary units equating to +/- 1.5" in the substrate plane: 30,30 = Center of the wafer) (color online) [159].

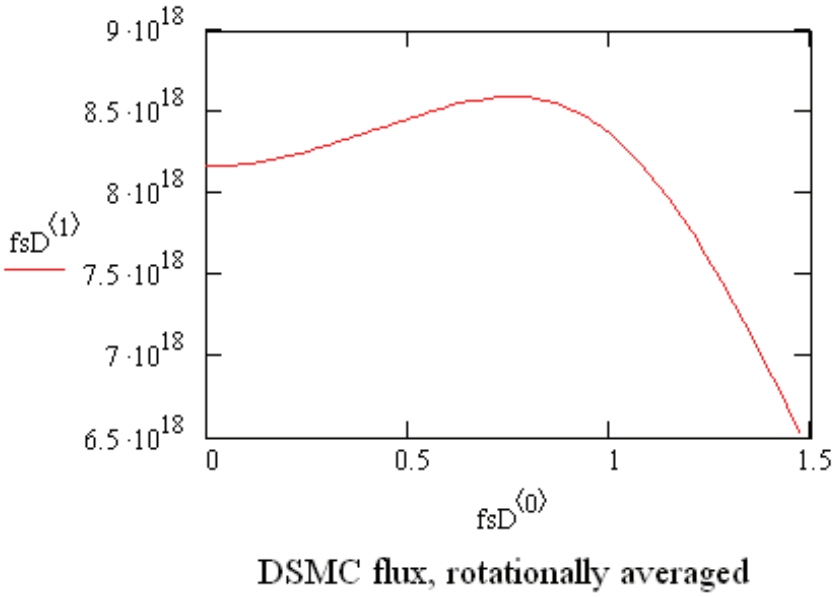


Figure 56: Rotationally Averaged Flux in Substrate Plane (x axis in radial inches) (color online) [159].

# APPENDIX C: ELECTRICAL CHARACTERIZATION

## C.1 van der Pauw method for resistivity and Hall coefficient measurements

The ability to measure resistivity and Hall coefficients for samples of irregular shape was developed by van der Pauw [160, 161]. He proved that the resistivity of a film can be measured without knowing the current pattern if the following are true:

1. Contacts are located on the sample periphery
2. Contacts are sufficiently small [162]
3. The film is uniformly thick
4. The film does not contain any isolated holes

Figure 57 shows an arbitrarily shaped sample with four numbered contacts. Using this figure, the value $R_{12,34}$ is defined as

$$R_{12,34} = \frac{V_{34}}{I_{12}}, \tag{28}$$

where $V_{34}$ is the voltage between contacts 3 and 4 (i.e. $V_{34} = V_3 - V_4$), and $I_{12}$ is the current from contact 1 to 2 (i.e. into 1, out of 2). If $R_{23,41}$ is defined similarly, the resistivity is given by [160, 161]

$$\rho = \frac{\pi}{\ln(2)} t \frac{R_{12,34} + R_{23,41}}{2} F, \tag{29}$$

where t is the thickness, F is called the F factor, used to satisfy the relationship

$$\frac{R_r - 1}{R_r + 1} = \frac{F}{\ln(2)} \operatorname{arcosh}\left( \frac{\exp[\ln(2)/\mathrm{F}]}{2} \right), \tag{30}$$

with

$$R_r = \frac{R_{12,34}}{R_{23,41}}. \tag{31}$$

When $R_r = 1$, F = 1, and the sample is considered to be a symmetrical sample.

When a magnetic field, B, is applied to the sample, the measured resistance will also change. For example, $R_{14,23}$ will change by $\Delta R_{14,23}$, and the Hall mobility can be found with this change with the equation

$$\mu_H = \frac{d\Delta R_{14,23}}{B\rho}, \tag{32}$$

where d is the film thickness. Therefore, several measurements can be made to determine the average resistances to determine resistivity and mobility. From these values, the Hall coefficient can be found using

$$\left|R_H\right| = \rho\mu_H. \tag{33}$$

Finally, the carrier concentration can be found using the Hall coefficient,

$$p = \frac{1}{qR_H} \text{ and } n = -\frac{1}{qR_H}. \tag{34}$$

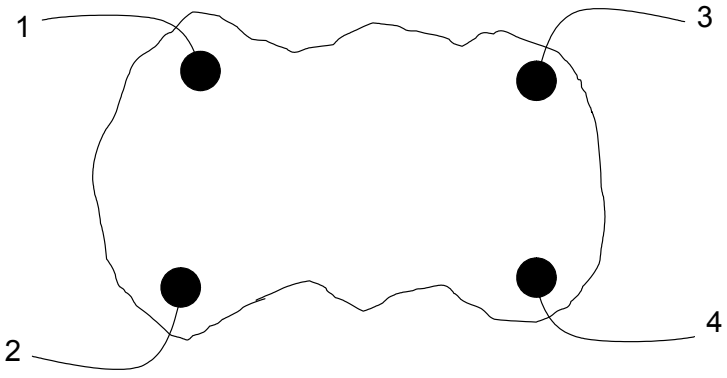


Figure 57: Irregularly shaped sample with four contacts, used to describe the van der Pauw method.

This theory was used to update and develop a resistivity and Hall coefficient measurement system using a fixed 3020 G magnet. The programming was done in

LabVIEW, and screen shots are shown in Figure 58 and Figure 59. Samples were mounted onto the stage with no magnet present. Probes were landed onto the four contacts, and information about the measurement was entered into the system, such as sample thickness, magnetic field, number of measurements to take before checking for tolerance, and tolerance of the measurement. Since voltages were much smaller for the Hall coefficient measurements than for resistivity measurements, different tolerances were used in each case. The measurement was then started with a relatively high current of approximately $1\times10^{-4}$ A, and the measured voltage was monitored. If the measured voltage was ever above 0.5 V, the current was reduced, and the measurement was restarted. Once an acceptable current was found, the measurement was allowed to proceed.

The sensitivity of the system was improved to measure Mg-doped GaN samples by adjusting the algorithm to determine resistances. Instead of using a difference in an average or instantaneous resistance value, statistical calculations were done to determine when resistances had stabilized. A sliding window of measurements was monitored, and the standard deviation of the measurements within the window was calculated. If the standard deviation was below a certain threshold, the value was accepted. If the standard deviation was above the threshold, the measurement continued, and the window of analyzed measurements moved on. This improvement allowed the successful measurement of the Mg-doped GaN samples with relatively low hole carrier concentration.

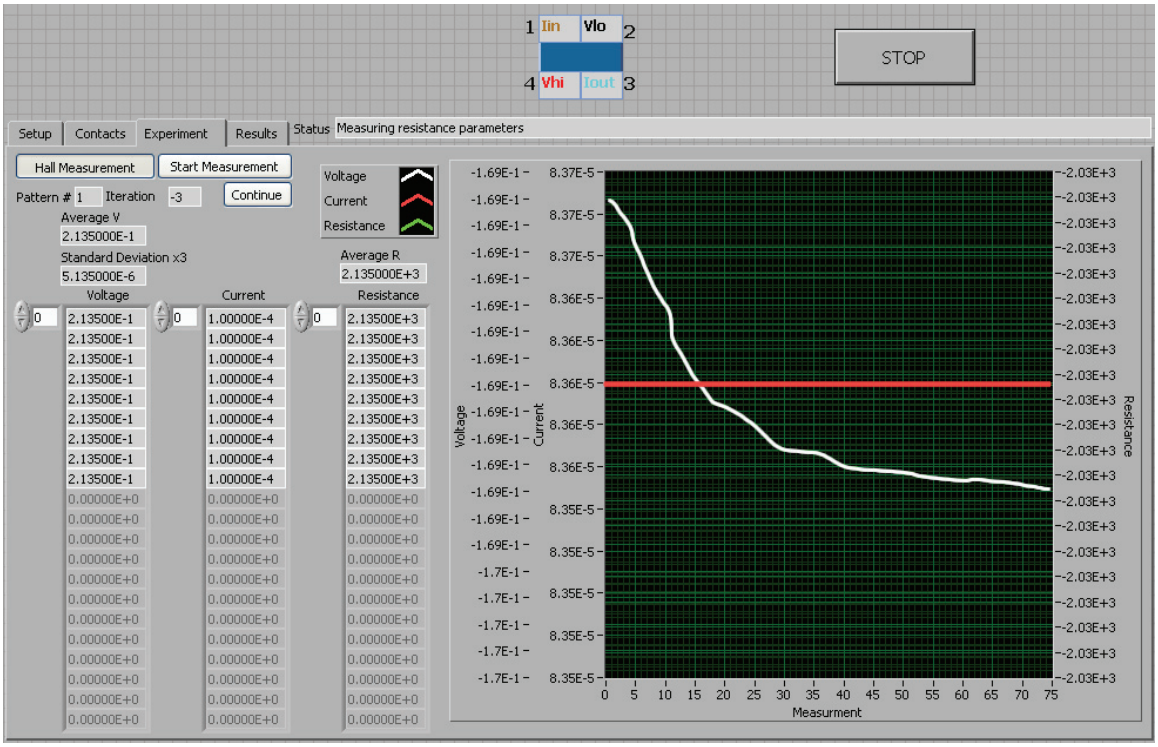


Figure 58: Screen shot of resistivity and Hall measurement LabVIEW program during a measurement (color online).

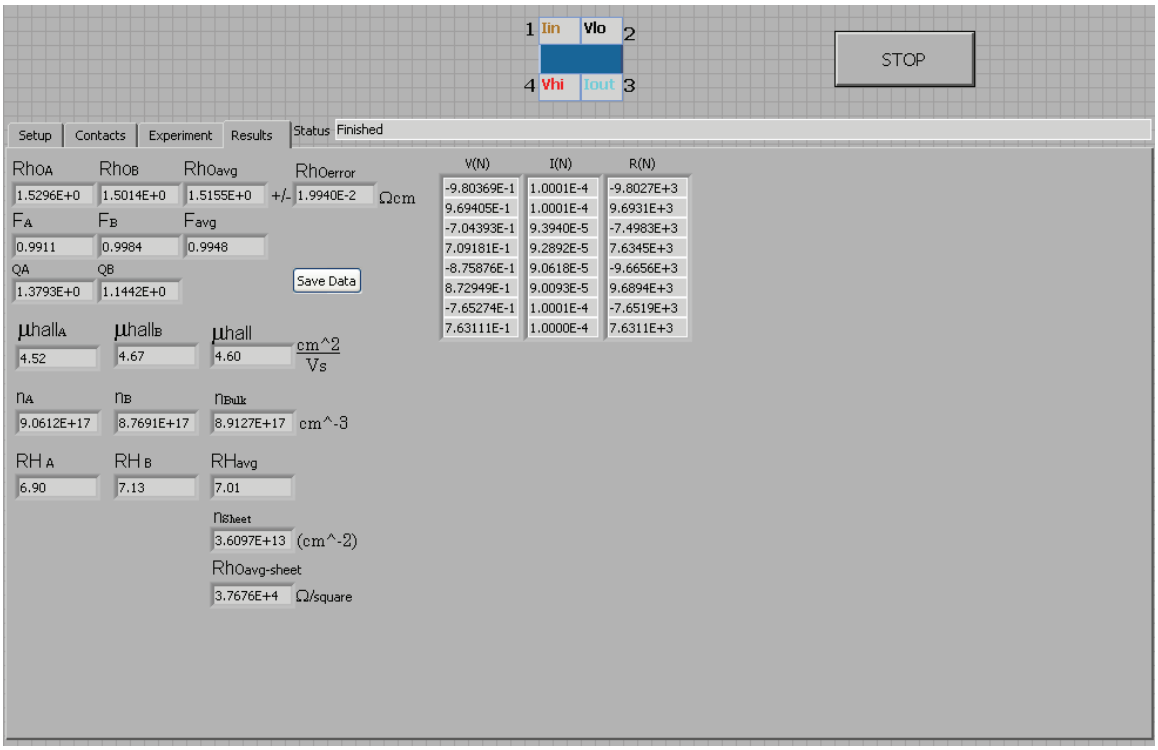

Figure 59: Screen shot of the resistivity and Hall measurement LabVIEW program after reporting the final values (color online).

## C.2 Deep level transient spectroscopy

The capture cross section of a trap indicates the ability to capture a carrier and characterizes the behavior of a trap. Figure 60 shows the potential well models for electrons in three different categories of capture cross sections [163]. With the potential well model, defects act to perturb the local electrostatic field and create a potential well shape with energy depth of $E_T$. When a defect has a high cross section ($10^{-14}$ to $10^{-8}$ $cm^2$), it has the opposite charge of a carrier when not filled and is therefore considered coulombic attractive, represented in Figure 60a. This results in capture for the free carrier of opposite charge within a distance of $R_C$. Once the defect is filled with a carrier, it becomes either coulombic repulsive, as in Figure 60b, or neutral, as in Figure 60c. When the defect has a low capture cross section ($10^{-22}$ to $10^{-18}$ $cm^2$), the charge of the defect is the same as the free carrier and considered to be coulombic repulsive, represented in Figure 60b. The defect is thought to be surrounded by a potential barrier of $q\Delta V$ which carriers must overcome to enter the trap. Traps with cross sections between coulombic attractive and repulsive ($10^{-18}$ to $10^{-14}$ $cm^2$) are considered neutral traps, represented in Figure 60c and are usually deep.

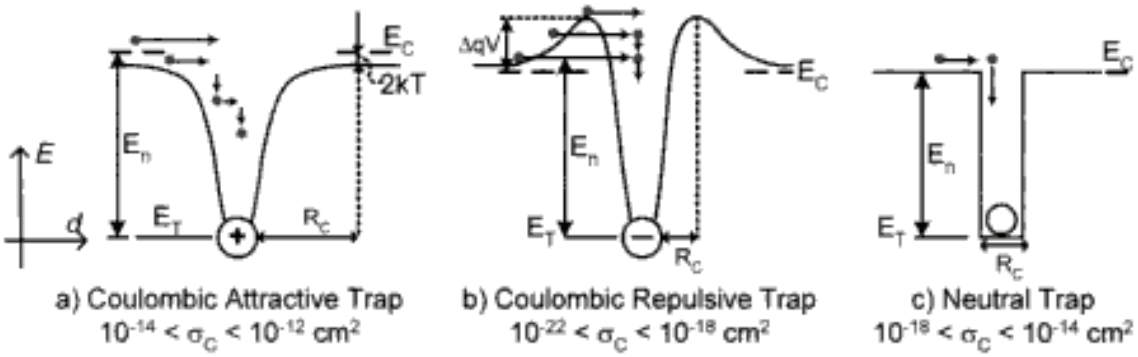


Figure 60: An illustration of different trap cross sections using the potential well model, showing a) a coulombic electron-attractive trap for large cross sections, b) a coulombic electron-repulsive trap for small cross sections and c) a neutral trap for cross sections falling in between the previous two [163].

DLTS is the name given to the characterization technique which determines the time constant in an exponentially decaying waveform of capacitance, current, or charge transients when transiently reverse biasing a rectifying junction, such as a Schottky diode or pn junction. Figure 61 illustrates the process by which the capacitance transient is formed for a $pn^+$ junction, with the focus on the p-type layer. The effects on the n-type layer are ignored for simplicity, though this is not unreasonable if the n-type layer is doped much higher than the p-type layer. The junction is initially reverse biased in Figure 61(a), with voltage $-V_0$ and capacitance $C_0$ and a depletion width of $W = x_n+x_p$ ($x_n<<x_p$). Since there are an abundance of free holes in the p-type layer, the traps outside of the depletion region are filled with holes (i.e., capture dominates emission) and the initial stead-state trap density is $p_T(0)$. At $t = 0$, the junction is pulsed with a reduced negative bias, $-V_1 > -V_0$, for time $t_f$. In response, the depletion width decreases and capacitance rises significantly. When $x_p$ is reduced, the empty traps that were previously in the depletion region are filled with holes as shown in Figure 61(b). This carrier

capture happens at an exponentially decaying rate and the capacitance is reduced likewise, as shown by the capture portion of Figure 62(a). At $t = t_f$, the bias is returned to the original reverse bias voltage, $-V_0$ and the depletion width increases beyond the original value as a result of the trapped charge, causing the capacitance to drop sharply, below the original $C_0$ value. The traps in the p-type layer are initially still filled with holes from the previous capture, as shown in Figure 61(c), but emission dominates capture for $t > t_f$ because emitted holes are quickly swept out of the depletion region by the electric field, so they are not able to be recaptured and the traps are eventually emptied. The emission portion of the curve in Figure 62(a) and the curves in Figure 62(b) illustrate the capacitance response during $t > t_f$.

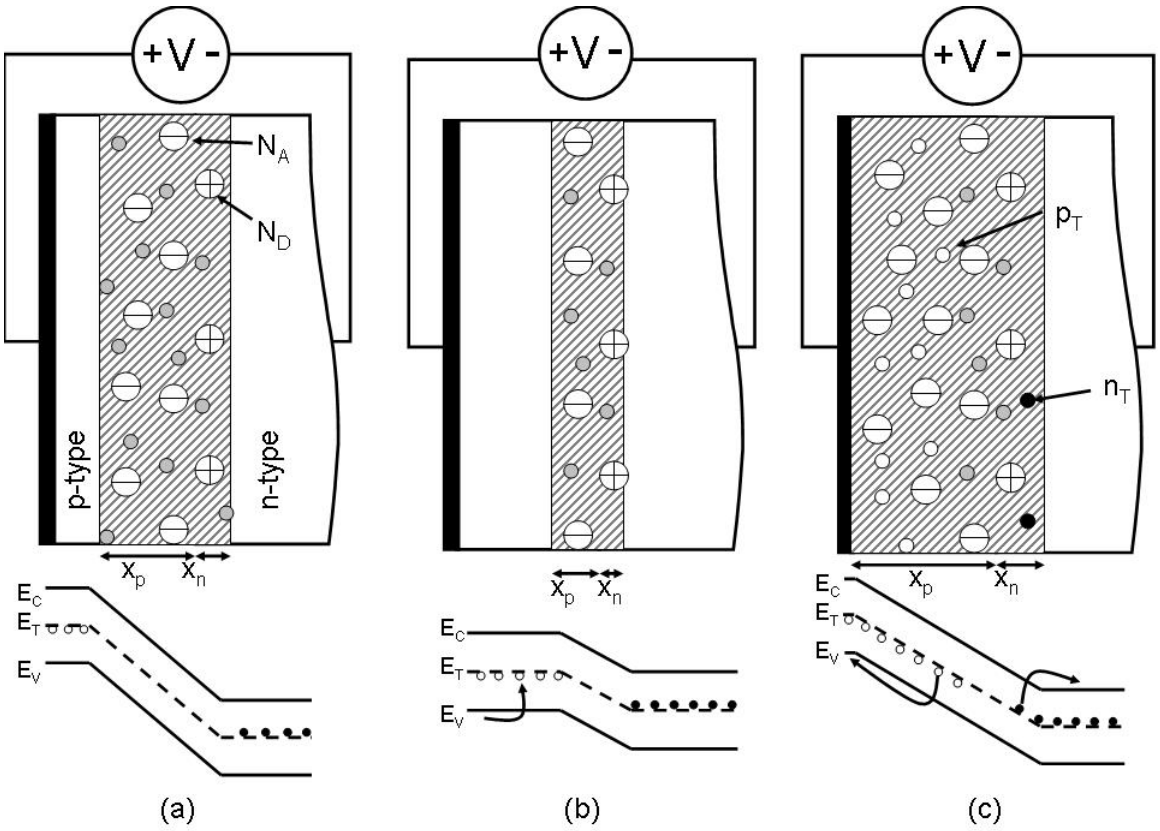


Figure 61: A demonstration of the changes in trap states for a pn diode at (a) initial reverse bias, (b) reduced reverse bias at $t = 0$ and (c) return to original reverse bias at $t = t_f$ and the respective effects upon the band structure.

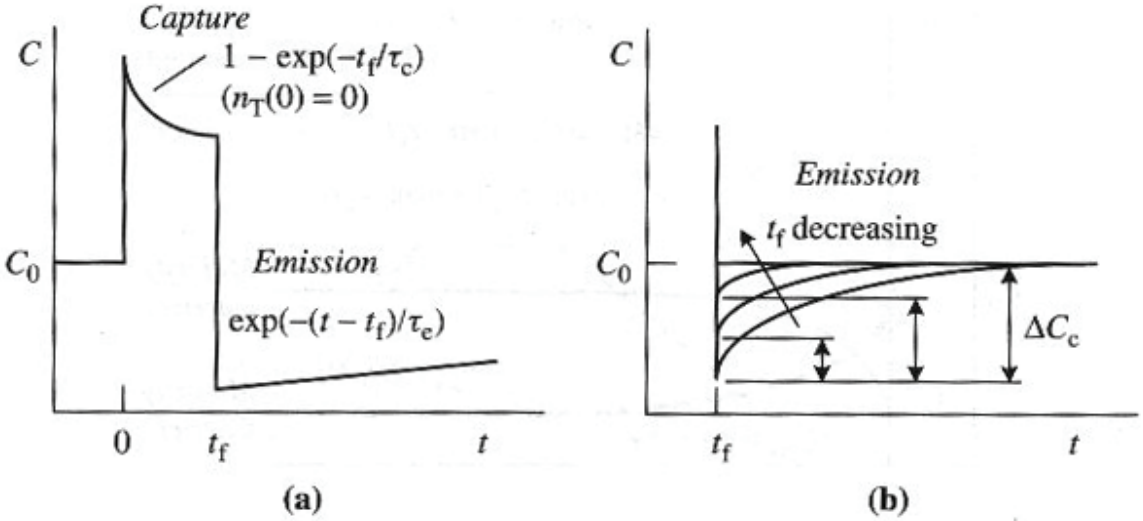


Figure 62: (a) Capacitance response to DLTS measurement, beginning with capture upon initial decrease in reverse bias at $t = 0$, followed by emission upon a return to the initial

reverse bias at $t = t_f$. (b) Changes in the capacitance response of the emission section as a function of changing the capture pulse width, $t_f$ [164].

The equation for the capacitance response is [164]

$$C(t) = C_0\left(1 - \frac{N_T - \left[N_T - p_T(0)\right]\exp\left(\frac{-t_f}{\tau_C}\right)}{2N_A}\exp\left(-\frac{t - t_f}{\tau_e}\right)\right), \tag{35}$$

for $N_T << N_A$, where $C_0$ is the initial reversed bias capacitance at steady-state (i.e., device with no deep-level impurities), $N_T$ is the concentration of defects, $p_T(0)$ is the concentration of filled traps at $t = 0$ (assumed zero), $t_f$ is the width of the lowered reversed bias pulse, $\tau_c$ is the capture time constant, NA is the concentration of acceptors and $\tau_e$ is the emission time constant. As $t \rightarrow \infty$ or $t_f \rightarrow \infty$, $C(t) = C_0$ and the deviation of capacitance from $C_0$ at $t = t_f$, as shown in Figure 62(b) as $\Delta C_C$, is [164]

$$\Delta C_C = C(t_f) - C(t \text{ or } t_f \rightarrow \infty) = \frac{N_T}{2N_A} C_0 \exp\left(-\frac{t_f}{\tau_c}\right) \tag{36}$$

when reverse-bias is re-established. Therefore, the defect concentration can be found by measuring $\Delta C_C$ and $(t_f/\tau_c)$ and using the equation [164]

$$N_T = 2N_A \frac{\Delta C_C}{C_0}\exp\left(\frac{t_f}{\tau_c}\right). \tag{37}$$

In theory, either the capture and emission curves could be used to extract energy level and cross section. However, in practice the capture process is more complicated since not all traps will initially be empty [165]. Therefore, the emission portion of the

capacitance transient will be used to extract the necessary parameters, with time offset to zero at $t_f$. As time progresses during emission, the capacitance transient follows the exponential time dependence as [164]

$$C(t) = C_0\left[1 - \frac{p_T(0)}{2N_A}\exp\left(-\frac{t}{\tau_e}\right)\right]. \tag{38}$$

Assuming that the emission coefficient remains constant from equilibrium to non-equilibrium conditions, the time constant of capacitance transient during emission ,$\tau_e$, can be written as [164]

$$\tau_e = \frac{\exp\left(\frac{E_T - E_V}{kT}\right)}{\gamma_p \sigma_p T^2}, \tag{39}$$

where $E_T$ is the trap energy level, $E_V$ is the valance band energy level, k is Boltzmann's constant, $t$ is the temperature, $\sigma_p$ is the hole capture cross-section of the trap and $\gamma_p = 3.25 \times 10^{21}(m_p/m_o)$ $cm^{-2}s^{-1}K^{-2}$, where $m_p$ is the hole density-of-state effective mass. Since $\tau_e$ decreases with increasing temperature, C-t measurements can be taken at various temperatures to find $\tau_e$, $t$ pairs. Once a sufficient number of ($\tau_e$, T) pairs are generated, the function $\ln(\tau_e T^2)$ can be plotted versus 1/T, resulting in a slope of $(E_T-E_V)/k$ and an intercept of $\ln[1/(\gamma_p\sigma_p)]$ on the $\ln(\tau_e T^2)$ axis. Using this method, the trap energy position ($E_T$-$E_V$) and capture cross section ($\sigma_p$) can be found.

Therefore, the role of DLTS is the determination of $\tau_c$ and $\tau_e$ at various temperatures for extraction of $N_T$, $\sigma_p$ and ($E_T$-$E_V$). However, many times there are several different time constants associated with multiple traps. Most DLTS systems use analog techniques to extract time constants, such as the double boxcar integrator example shown in Figure 63, but others use more modern digital analysis for distinguishing

between traps [166]. Some of these systems have demonstrated $\Delta C_C / C_0$ as low as $10^{-6}$ [166, 167], allowing measurements of trap densities as low as $10^{-6}N_A$. For highly doped GaN with Mg with hole concentrations of $7 \times 10^{18}$ $cm^{-3}$ [91] and assuming a 1% activation for Mg acceptors, this technique allows the detection of trap concentrations as low as $7 \times 10^{14}$ $cm^{-3}$. At lower doping levels, the sensitivity is decreased because of a capacitance noise floor and often raises the lower detection limit to $10^{-4}N_A$.

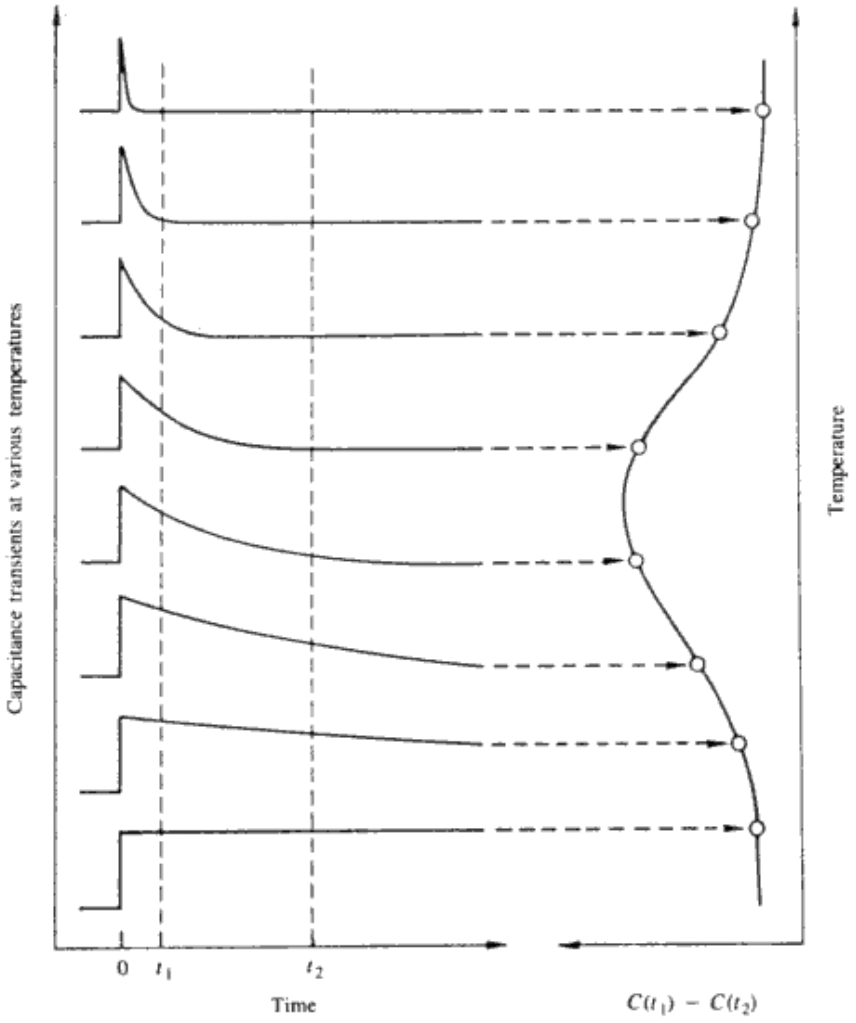


Figure 63: Illustration of the rate window concept with a double boxcar integrator, corresponding to the average difference of capacitance amplitude at the sampling times $t_1$ and $t_2$ [168].

# APPENDIX D: STRUCTURAL CHARACTERIZATION

## D.1 Secondary ion mass spectroscopy

The SIMS instrument used was an Atomika Ion microprobe A-DIDA 3000-30, with a typical analytical chamber base pressure of $3 \times 10^{-9}$ Torr. The ion guns were mass filtered and neutral trapped using $O_2^+$ and $Cs^+$ projectile ions as the primary ion beam. It was operated at an oxygen beam potential of +15keV at normal incidence to the surface and energy of approximately +15keV at a 45° angle to the surface for cesium. The secondary ion detector consisted of a quadrupole mass spectrometer and an electron multiplier. The secondary ion current signal was electronically gated for 30% of a square rastered area to minimize crater edge effects. Beam current was adjusted from 50 – 100 nA and scan size was adjusted from $100 \times 100$ to $200 \times 200$ $\mu m^2$ to achieve the highest possible signal for the desired secondary ion, without exceeding $1 \times 10^6$ counts per second, and to keep the sputter rate low enough for good depth resolution. For oxygen beam analysis, the settings listed in Table 10 were used as a starting point for optimizing results. Starting parameters were only slightly different for cesium beam analysis.

Table 10: Initial settings used for oxygen-beam SIMS

| Control | Setting | Control | Setting | Control | Setting |
|---|---|---|---|---|---|
| Scan Control | | | | | |
| X | -1.88 | Y | 3.02 | Width | 1 |
| Time | 04 s/Frame | Gate | 5 × 10% = 50% Cont. | | |
| Beam Align | | | | | |
| X | 1.9 | Y | 6.49 | Beam | 4.55 |
| Sample Parameters | | | | | |
| Tau | OFF | Current | +50 nA | Bias | 5, Ext. |
| Source | Ar/Ox | | | | |
| Top Controls | | | | | |
| Filament | 0.1 | Discharge | 0.51,0.74 | Magnet | 0.525 |
| Extraction | 0.49 | Oxygen Src | 0.5 bar | Ion Gun | $1.9\times10^{-6}$ Torr |
| Multiplier HV | 2.75 | Focus | 9.94 kV (6.66) | Ion Energy | 14.99 kV (10.65) |
| Secondary Ion Control | | | | | |
| ΔM | 6.48 | Resolution | 6.68 | Accel. | 10 |
| ΔE | 5.3 | Focus | 5.94 | | |
| Electron Gun | | | | | |
| X | -0.465 | Y | 2.875 | Energy | 2.5kV (2.515) |
| Filament | 2.4kV (7.17) | Focus | 9.7 | Wehnelt | 0.2 |

## D.2 Atomic force microscopy

Atomic force microscopy was done on a Veeco Metrology Group/Digital Instruments Dimension 3100 scanning probe microscope (SPM). Tapping mode scanning, as shown in Figure 64, was exclusively done for AFM scans. Because GaN and GaN alloys are hard materials, stiff AFM tapping mode probes were also exclusively used. The MikroMasch NSC16 cantilever-style tapping mode AFM probes are shown in Figure 65, with specifications given in Table 11. These probes offered a high force constant that allowed excellent imaging of GaN and GaN alloy surfaces.

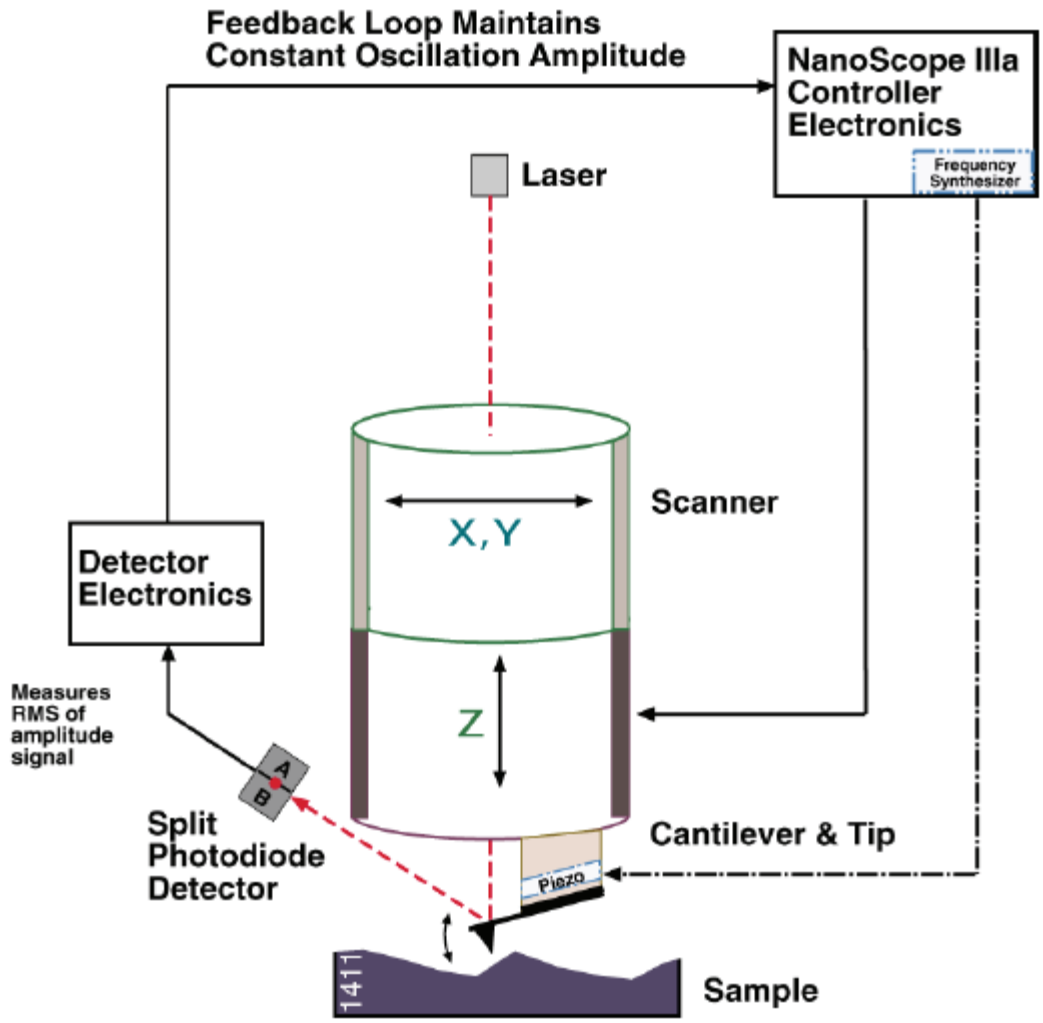


Figure 64: Cartoon of AFM tapping mode operation (color online) [169].

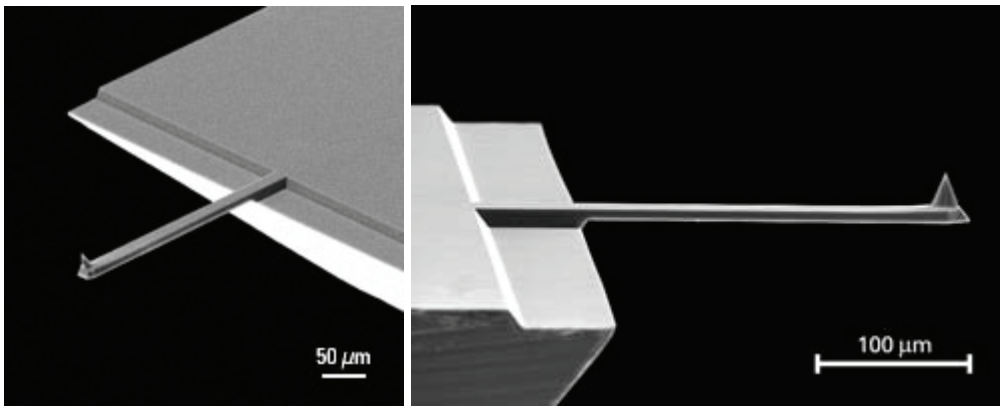


Figure 65: SEM images of a MikroMasch NSC16 cantilever style AFM probe, made of silicon [170].

Table 11: Specifications of the MikroMasch NSC16 cantilever style AFM probes [170].

| Cantilever Length, l ± 5, µm | Cantilever Width, w ± 3, µm | Cantilever Thickness, µm | | | Resonant Frequency, kHz | | | Force Constant, N/m | | |
|---|---|---|---|---|---|---|---|---|---|---|
| | | min | typical | max | min | typical | max | min | typical | max |
| 230 | 40 | 6.5 | 7 | 7.5 | 150 | 170 | 190 | 25 | 40 | 60 |

The SPM power supplies were turned on, and the software was started. The NSC16 probe was loaded onto the probe holder. The tip of the cantilever was found using the laser for a sum of approximately 2 at the photo detector. The photo detector was then centered on the reflected laser. The !Tapping AFM profile was selected in the SPM software, and the microscope was centered and focused onto the cantilever tip. After focusing the microscope on the sample surface, auto tuning was done for the tapping mode probe and the values were recorded and compared to Table 11 to track degradation of the probe tip. The auto tune control used a start frequency of 50 kHz, an end frequency of 400 kHz, target amplitude of 1.5 V, and a peak offset of 5%. Initial values were then entered into the SPM software, according to Table 12 and Table 13. Finally, the AFM scans were then done by optimizing the images with slight adjustments to the initial settings. These optimizations were done by disabling the slow axis scan, and monitoring the scope trace. The amplitude setpoint was adjusted down to press harder on the surface, if necessary, but the integral and proportional gain were rarely adjusted. Scans were usually done for widths of 10, 5, 2, and 1 µm. Analysis of the AFM data was

then done using either the Veeco software, n-Surf software [171], or Gwyddion open source software [172].

Table 12: Initial settings for tapping mode AFM.

| Scan Controls | | Feedback Controls | | Other Controls | |
|---|---|---|---|---|---|
| Scan Size | 1.00 μm | Integral gain | 0.2 | Microscope mode | Tapping |
| Aspect ratio | 1:1 | Proportional gain | 0.2 | Z limit | 6.116 um |
| X offset | 0.00 nm | Amplitude setpoint | 1 V | Illumination | 100 |
| Y offset | 0.00 nm | | | Unit | Metric |
| Scan angle | 0.00 ° | | | Color table | 12 |
| Scan rate | 1.00 Hz | | | Engage Setpoint | 1 |
| Tip velocity | 2.00 μm/s | | | | |
| Samples/line | 512 | | | | |
| Lines | 256 | | | | |
| Slow scan axis | Enabled | | | | |

Table 13: Initial input channel settings for tapping mode AFM.

| Channel 1 | | Channel 2 | | Channel 3 | |
|---|---|---|---|---|---|
| Data type | Height | Data type | Amplitude | Data type | Phase |
| Data scale | 100 nm | Data scale | 100 mV | Data scale | 100 ° |
| Data center | 0 nm | Data center | 0 mV | Data center | 0 ° |
| Line direction | Retrace | Line direction | Retrace | Line direction | Retrace |
| Realtime planefit | Line | Realtime planefit | Line | Realtime planefit | Line |
| Offline planefit | Full | Offline planefit | Full | Offline planefit | Full |

## D.3 X-ray diffraction

X-ray diffraction (XRD) was performed on a Phillips X'Pert system. The following procedure was used when taking x-ray diffraction data. The sample was loaded into the machine, and all slits and masks were removed. The Triple Axis optics were used exclusively for all XRD scans, so no slits were necessary. Upon opening the software, any offsets were cleared, and power was ramped up, if necessary. The detector

was aligned to the source by adjusting the 2-Theta angle, and cut in half by the sample by adjusting the z-axis. The primary peak of the substrate (i.e. sapphire 0 0 6) was optimized through a series of Omega, 2-Theta-Omega, Psi, and Phi scans. After substrate alignment, various peaks of the grown film were scanned according to Table 14.

Table 14: Typical scan settings for manual XRD measurements

| | 2 Theta-Omega | | Omega | | | Phi |
|---|---|---|---|---|---|---|
| | GaN (0 0 2) | InGaN (0 0 2) | GaN (0 0 2) | InGaN (0 0 2) | GaN (1 0 2) | GaN (1 0 2) |
| Range | 9 | 12 | 4 | 6 | 4 | 360 |
| Step size | 0.004 | 0.004 | 0.003 | 0.003 | 0.003 | 0.5 |
| Time per step | 0.25 | 0.25 | 0.25 | 0.25 | 0.25 | 0.25 |
| Unit cell | GaN | GaN | GaN | GaN | GaN | GaN |
| Miller indices | 0 0 2 | 0 0 2 | 0 0 2 | 0 0 2 | 1 0 2 | 1 0 2 |
| Psi | 0 | 0 | 0 | 0 | | |
| Phi | 0 | 0 | 0 | 0 | | |
| 2 Theta | 37.5 | 36 | 34.5658 | 36 | | |
| Offset | 0 | 0 | 0 | 0 | | |
| Omega | 18.75 | 18 | 17.2829 | 19 | | |
| Total time (sec) | 562.5 | 750 | 333.33 | 500 | 333.33 | 180 |

## D.4 Profilometry

Profilometry was done using a Tencor KLA P15 OF Profilometer. Since GaN and GaN alloys are very hard materials, the stylus force was set to 50 mg, and scan speed was set to at most 50 μm per sec to achieve high resolution scans. Sample thickness was found by scanning approximately 1.5 mm from an area of bare sapphire to the film surface. These areas of bare sapphire exist because the retaining clips of the spring plates used when growing blocked growth in these areas. Sufficient scan length was used on the bare sapphire to obtain a leveling calculation for the profile scan. This measurement

was done on all available step edges, which were usually four from the four mounting clips. These measurements were then averaged for an average film thickness. From the average film thickness, the growth rate could be calculated using the total growth time.

### D.5 Scanning electron microscope and Energy-dispersive x-ray spectroscopy

Scanning electron microscopy was done in a Hitachi 3500H scanning electron microscope (SEM). However, since GaN and GaN alloys are wide band gap materials, sample charging created a problem with imaging with the SEM. Minimizing sample charging by using a lower accelerating voltage resulted in noisy images. Nevertheless, some successful imaging was accomplished.

The Energy-dispersive x-ray spectroscopy (EDS) system used was a Noran EDS and was attached to the SEM. Once an area of interest was found with the SEM, the EDS PHA status was monitored for the count rate of detects per second, and deadtime. Target values of 1800 detects per second and 14 – 18% dead time were achieved by adjusting the working distance (WD), current, and voltage on the SEM. The EDS preset time was set to 60 sec, and the time constant was set to Classic for the measurements. After the measurement, elements were assigned to the peaks using a combination of automatic and manual identification. The data was then quantified to find the weight and atomic percent of each element detected.

# APPENDIX E: INTERFACING 22-BIT CAMERA WITH LABVIEW

## E.1 Camera properties

The Basler A601f-HDR camera, shown in Figure 66, was used for the RHEED transient feedback for closed-loop control of MBE growth, as described in Chapter 7. This camera was chosen for the high dynamic range of intensities it can detect and distinguish. This was necessary for RHEED imaging because of the drastic intensity changes RHEED can exhibit during surface changes. Before using a high dynamic range camera, the exposure time had to be dynamically and manually adjusted to avoid clipping of the RHEED image at high intensities, or underexposure of the image at low intensities. The specifications of the A601f-HDR are given in Table 15, which shows the video output mode capable of delivering high dynamic range response with 22 bits per pixel. Since this camera would be used to image RHEED patterns and detect RHEED intensity transients, it was paramount that the RHEED luminescence color was well within the spectral response of the camera. Figure 67 shows the spectral response for the A601f-HDR, and because the RHEED luminescence color was green (500 – 565 nm), the camera met the criterion.

Figure 66: Basler A601f-HRD camera (color online) [173].

Table 15: Specifications for the Basler A601-HDR camera [173].

| Category | Specification |
|---|---|
| Sensor type | Micron MT9V403 – ½ inch, CMOS, Global Shutter |
| Pixels | 656 (H) x 491 (V) |
| Pixel size | 9.9 µm (H) x 9.9 µm (V) |
| Max. frame rate<br>(at full resolution) | 60 fps in 8 bit output modes<br>30 fps in 16 bit output modes<br>(frame rate is lower when the HDR feature is used) |
| Video output formats | Mono 8 (8 bits/pixel)<br>Mono 16 (16 bits/pixel – up to 16 bits effective)<br>Vendor Specific 0 (up to 22 bits/pixel) |

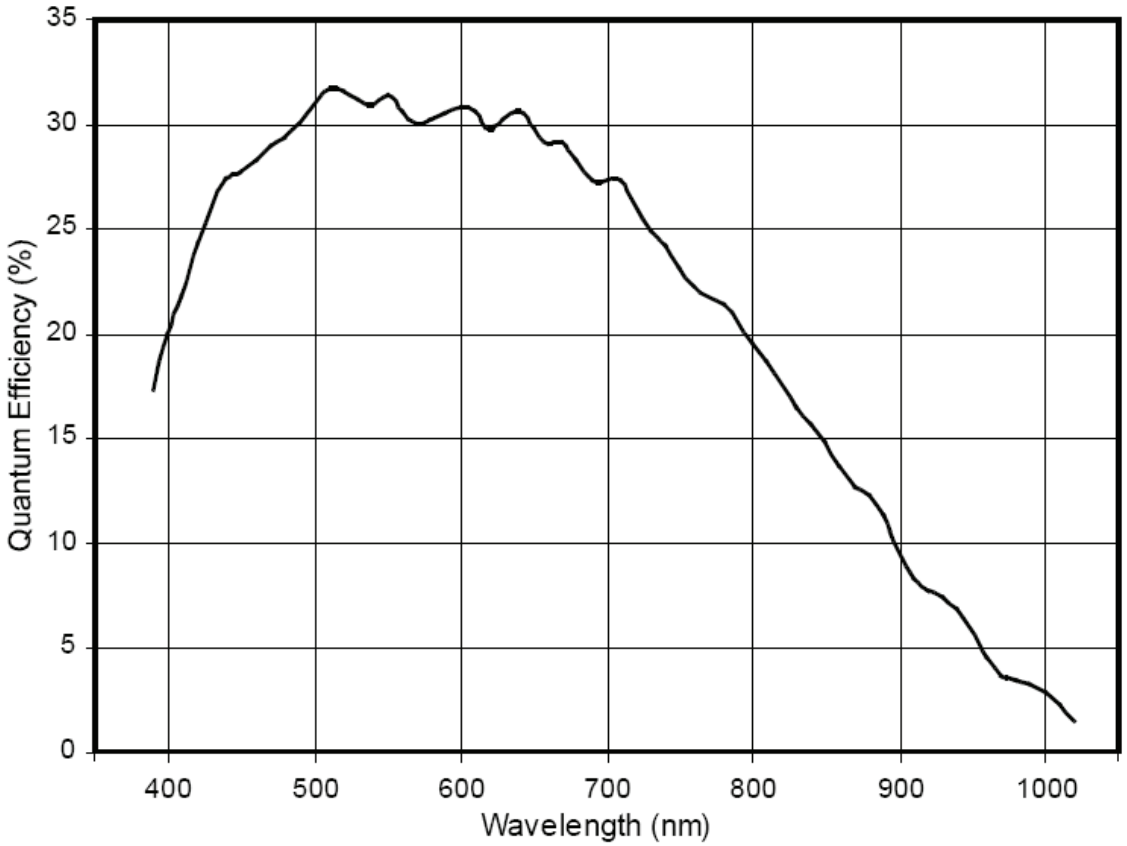

Figure 67: Spectral response for the Basler A601f-HDR [173]. Note the excellent response in the green region from 500 – 565 nm.

The high range of the A601f-HDR is achieved by capturing several complete images at progressively longer exposure times, then combining the data into one image. For the shortest exposure times, the brightest areas will be sharp but the dark areas will be underexposed. For the longest exposure times, the dark areas will be sharp, but the bright areas will be overexposed. The internal HDR algorithm of the camera analyzes each pixel of the collected images, and chooses the pixel that best represents the image without over- or underexposing the pixel. These representative pixels are then merged and represented on an output range of up to 22 bits. Therefore, while the camera captures several images internally, it behaves as though it is capturing a single image.

The main parameters of the HDR feature are quality, dynamic bits, and start shutter. The quality parameter setting specifies how many internal images will be captured and combined into the final output image. There are four quality settings including high, normal, medium and low, with higher quality indicating greater number of internal images used to create the output image. The practical implication in the output as a result of changing the quality parameter is lower noise versus higher frame rate. Noise is obviously reduced with an increased number of internal images, but frame rate is also reduced. Figure 68 shows the signal-to-noise ratio for different quality settings at 20 bits per pixel. The dynamic bits parameter setting specifies the bit depth of the output image generated by the camera, and this can be as high as 22 bits. However, this parameter is limited by the start shutter parameter. As the start shutter value is increased, the maximum allowed dynamic bits parameter is decreased. The start shutter parameter setting represents the variable n in the equation

$$\text{Start Shutter Time} = (n \times 20\ \mu s). \tag{40}$$

Since the A601f-HDR captures several internal images at progressively longer exposure times, this setting determines the exposure time for the first image in the series. Other exposure times are calculated by the camera based on the start shutter value. Increasing this parameter will increase the brightness of the output image, but will also reduce frame rate. For the presented experiments, the best HDR parameters found were high quality, 16 bits per pixel, and a start shutter of 10 (200 μs starting shutter time). This resulted in bright output images with intensity levels in the 5,000 range, with a frame rate near 5 frames per second. Figure 38 shows a typical HDR image and intensity response.

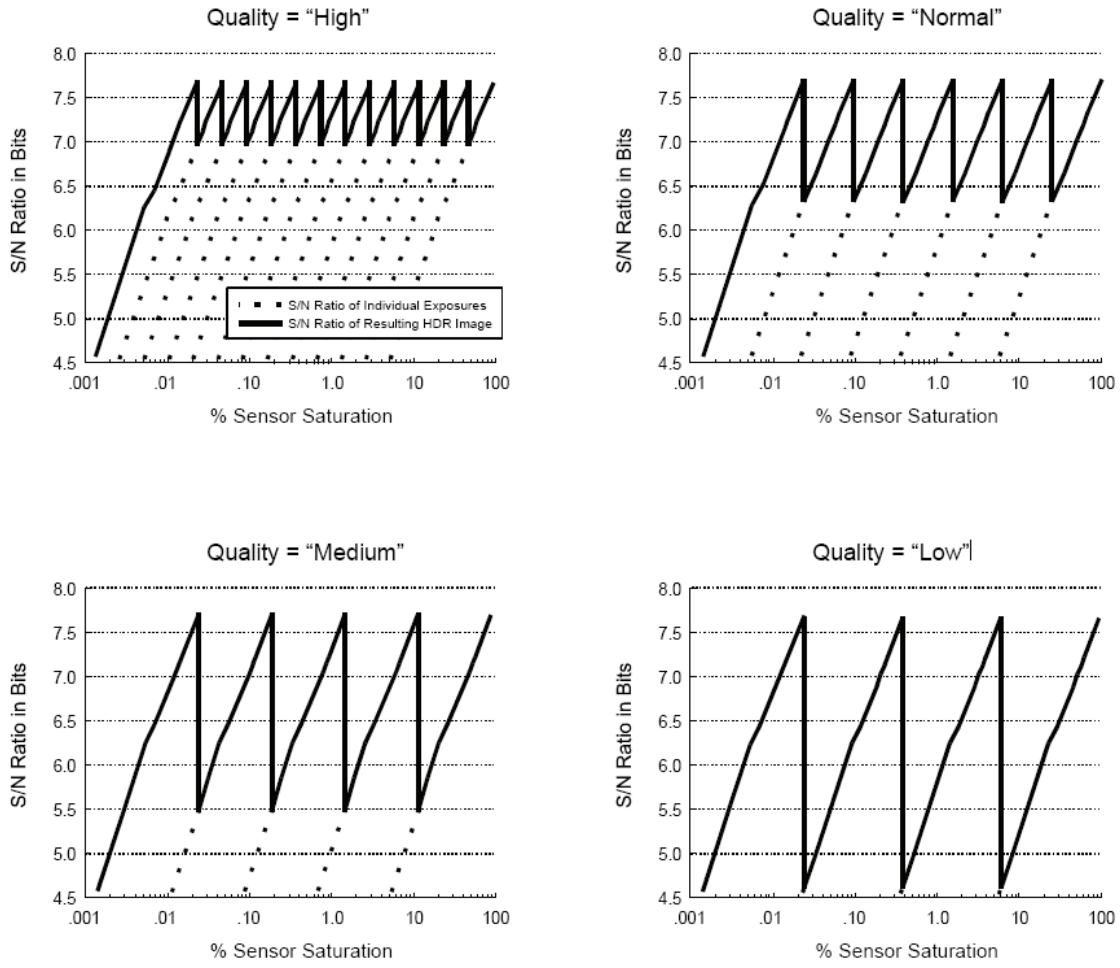


Figure 68: Signal-to-noise ratios for Basler A601f-HDR camera images with a 20 bit depth at different quality parameter settings [173].

## E.2 Camera and computer communication

The Basler A601f-HDR uses an IEEE-1394a 2000 compliant physical layer device to transmit data [174]. The camera has a 6-pin connector for a standard IEEE-1394 socket. Camera parameters are set by the IEEE-1394 interface, including the HDR parameters of quality, dynamic bits, and start shutter. However, other parameters must be set before the HDR feature is available. These parameters include the video format, the video mode, and the color coding. The video format must be set to video format 7,

the mode must be set to mode 2, and the color coding must be set to Vendor Specific 0. With these settings, the camera actually outputs a 16 bit image. However, with the Vendor Specific 0 color coding, the least significant byte of the 16 bits per pixel represents an unsigned base, and the most significant byte represents an exponent, for an actual value of

$$\text{Actual Pixel Value} = \text{Base} \times 2^{\text{exponent}}. \quad (41)$$

Therefore, if a value of 0x0DC3h is output, the base would be 195d and the exponent would be 13d for an actual value of

$$\text{Actual Pixel Value} = 195 \times 2^{13} = 1597440\text{d}. \quad (42)$$

Using this method, the A601f-HDR can output pixel values of up to 22 bits without modifying the IEEE-1394 standard which limits pixel values to 16 bits. Built-in LabVIEW IEEE-1394 drivers were used to set the video format and video mode, but the color coding was a non-standard setting. Therefore, the specific color coding setting was read from an inquiry register at address 0xFFFF F1F0 0224, and written to the control register at address 0xFFFF F1F0 0210.

To modify the HDR parameters in the A601f-HDR, a globally unique identifier (GUID) or universal unique identifier (UUID) was needed for the control or status register (CSR). The GUID was then used to find the address of the IEEE-1394 register for that feature. The GUID consists of one 32 bit number, two 16 bit numbers, and a sequence of 8 bytes, such as CA8A916A – 14A4 – 4D84 – BBC9 – 93DF50495C16, for example. The GUID was divided into sections as (D1) – (D2) – (D3) – (D4[0] – D4[1]) – (D4[2] – D4[7]) and written to an inquiry register laid out as shown by Table 16 at address 0xFFFF F2F0 0000. If the camera recognizes the GUID as a valid CSR for the

camera's smart features (SF), an address for the CSR is written by the camera to the SF address register at addresses 0xFFFF F2F0 0020 and 0xFFFF F2F0 0024 in the format shown by Table 17. However, if the camera doesn't recognize the GUID, it will return 0x0.

Table 16: Basler A601f-HDR smart feature inquiry register layout [173].

| | Bit | | | |
|---|---|---|---|---|
| Offset | 0 – 7 | 8 – 15 | 16 – 23 | 24 – 31 |
| 10h | D1 | | | |
| 14h | D3 | | D2 | |
| 18h | D4[3] | D4[2] | D4[1] | D4[0] |
| 1ch | D4[7] | D4[6] | D4[5] | D4[4] |

Table 17: Basler A601f-HDR smart feature address register layout [173].

| | Bit | | | |
|---|---|---|---|---|
| Offset | 0 – 7 | 8 – 15 | 16 – 23 | 24 – 31 |
| 20h | Address Low | | | |
| 24h | Address High | | | |

The CSR GUID for the HDR features was 93F1F19D – 5761 – 4260 – A9D787F7BE722129, which returned a CSR address of 0xFFFF F2F0 00D0. This register had a layout indicated by Table 18. Thus, values of the quality, dynamic bits, and start shutter parameters could be set using IEEE-1394 register communication provided by LabVIEW. However, when images were collected from the camera, they had to be converted from 16-bit, according to equation 41. Furthermore, while the data was being recorded and analyzed on a higher bit level, the image had to be adjusted for

monochrome 8-bit display. A simple gamma function was used to accomplish this, as shown by

$$P_8 = 255 \times \left( \frac{P_{HDR}}{P_{HDRMax}} \right)^{\gamma} . \tag{43}$$

Where $P_8$ is a resulting 8 bit pixel value, $P_{HDR}$ is the original pixel value of the HDR image, $P_{HDRMax}$ is the maximum pixel value of the entire HDR image, and $\gamma$ is the gamma setting to adjust sensitivity. This allowed visual display of images as high as 22-bits per pixel on a standard monochrome 8-bit display. Figure 38 shows a clear RHEED image with this gamma function adjustment.

Table 18: Basler A601f-HDR HDR CSR layout [173].

| Position | Field | Bit | Description |
|---|---|---|---|
| 0 | Presence_Inq (Read only) | [0] | Presence of this feature<br>0: Not available, 1: Available |
| | | [1] | Reserved |
| | One_Push_Auto (Read / write) | [2] | One push automatic parameter adjustment. Setting the bit to 1 will initiate the automatic adjustment routine. The bit will reset to zero when the routine is complete. |
| | | [3] | Reserved |
| | Quality (Read / write) | [4 … 5] | Determines the number of exposures that will be captured to create the final image. Higher quality requires more exposures.<br>0: High quality<br>1: Normal quality<br>2: Medium quality<br>3: Low quality |
| | | [6 … 7] | Reserved |
| | Min_Dynamic_Bits (Read only) | [8 … 15] | Minimum allowed value for the dynamic bits setting |
| | Max_Dynamic_Bits (Read only) | [16 … 23] | Maximum allowed value for the dynamic bits setting |
| | Dynamic_Bits (Read / write) | [24 … 31] | Sets the depth of the HDR image |
| 4 | Min_Start_Shutter (Read only) | [0 … 31] | Minimum allowed value for the starting shutter setting |
| 8 | Max_Start_Shutter (Read only) | [0 … 31] | Maximum allowed value for the starting shutter setting |
| 12 | Start_Shutter (Read / write) | [0 … 31] | Start shutter time = (start_shutter register value x 20 µs) |

# APPENDIX F: IN SITU GROWTH RATE ANALYSIS TECHNIQUE

Growth rate determination is crucial for controlling MBE growth and achieving consistent results. The growth rate is commonly extracted either *in situ* from RHEED oscillations [121, 123, 126], or *ex situ* by thickness measurements. While *in situ* growth rate determination is ideal and preferred over *ex situ* techniques, RHEED growth oscillations are not always observed for all MBE machines and material systems [25]. Though not as widely used as the previous techniques, pyrometric interferometry (PI) was developed on the GaAs material system and is another *in situ* technique that can be used to determine growth rate [175, 176]. Furthermore, the application of PI on the GaN material system has been successful [177-179].

For MBE growth on sapphire, heat is coupled into the substrate by the heater filaments heating the backside metallization. The heat is then transferred through the sample by conduction, and then emitted at the substrate surface. If there is a heterointerface near the surface, multiple internal reflections can occur for wavelengths that are not attenuated, before they exit the film, as shown in Figure 69. The combination of these reflections cause constructive and destructive interference. Moreover, for any given wavelength ($\lambda$), there will be a maximum in the intensity for each increment of optical path of $\lambda/(2\eta)$. For a film growing in thickness, this will cause oscillations with a period (T), which is related to the growth rate (G) and refractive index of the material ($\eta$) through the equation [175, 176]

$$T = \frac{1}{G}\frac{\lambda}{2\eta}. \tag{44}$$

Therefore, by fitting the measured temperature oscillation data to the equation

$$Temp = A_0 e^{A_1 t} \sin\left(A_2 t + A_3\right) + A_4 , \tag{45}$$

where t is the time and $A_0 - A_4$ are fitting parameters, the period can be extracted from the $A_2$ fitting parameter as $T = 2\pi/B$. Rearranging equation 44, the growth rate can be determined using the wavelength of the pyrometer, 940 nm, and the index of refraction of GaN, which is 2.33 [180]. Finally, the thickness can be extracted from the growth rate by multiplying by the total growth time.

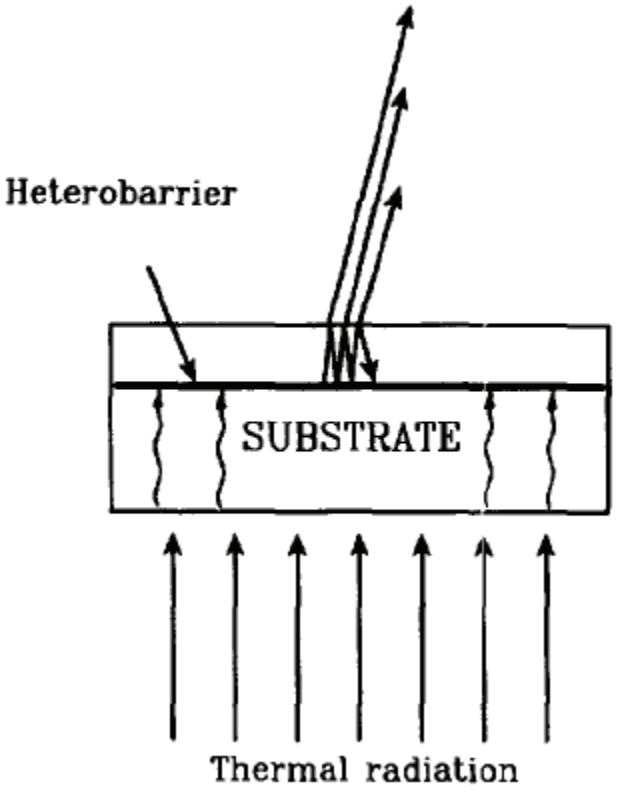


Figure 69: Schematic of basis of pyrometric interferometry: heat flows through substrate, resulting in multiple reflections in film, which create interference effects depending on thickness of film.

An IRCON pyrometer was used to sample the temperature of a 3 mm diameter area at the center of the substrate by monitoring emitted radiation in a narrow range of wavelengths (0.94 ± 0.03 μm). The analog output signal of the pyrometer was recorded using a LabVIEW program as growth proceeded. The data was then fit to equation 45 to extract the growth rate and total thickness. Figure 70 shows a screen capture of the LabVIEW program successfully extracting the growth rate and thickness of a GaN growth.

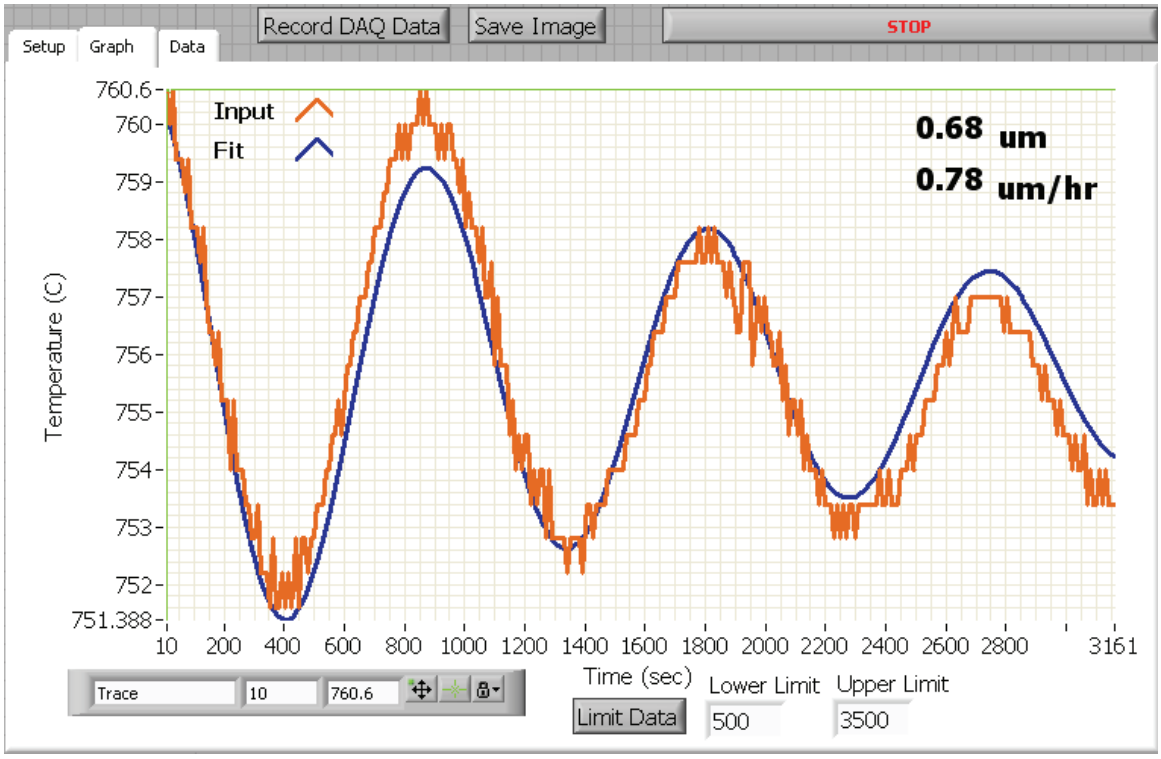


Figure 70: Screen shot of pyrometric interferometry (PI) LabVIEW program, which determines thickness and growth rate *in situ* (color online).

# REFERENCES


[1] W. C. Johnson, J. B. Parsons, and M. C. Crew, "Nitrogen Compounds of Gallium III," *Journal of Physical Chemistry,* vol. 36, pp. 2651-2654, Oct. 1932.

[2] W. Shan, T. Schmidt, X. H. Yang, J. J. Song, and B. Goldenberg, "Optical properties of wurtzite GaN grown by low-pressure metalorganic chemical-vapor deposition," *Journal of Applied Physics,* vol. 79, pp. 3691-3696, Apr 1996.

[3] A. Jones, M. Clemmet, A. Higton, and E. Golding, "Gases," in *Access to Chemistry* Cambridge: The Royal Society of Chemistry, 1999, pp. 173-184.

[4] M. Fukuda, "Optical Properties," in *Optical Semiconductor Devices* New York: John Wiley & Sons, Inc., 1999, pp. 37-54.

[5] M. A. Chancey, "Short Range Underwater Optical Communication Links," in *Electrical Engineering*. vol. Master of Science Raleigh, NC: North Carolina State University, 2005, p. 117.

[6] R. Juza and H. Hahn, "Über die Kristallstrukturen von Cu3N, GaN und InN Metallamide und Metallnitride," *Zeitschrift für anorganische und allgemeine Chemie,* vol. 239, pp. 282-287, 1938.

[7] H. G. Grimmeiss and H. Koelmans, "Edge and other emission of GaN," *Zeitschrift fur Naturforschung A (Astrophysik, Physik und Physikalische Chemie),* vol. 14a, pp. 264-271, 1959.

[8] H. P. Maruska and J. J. Tietjen, "THE PREPARATION AND PROPERTIES OF VAPOR-DEPOSITED SINGLE-CRYSTALLINE GaN," *Applied Physics Letters,* vol. 15, pp. 327-329, 1969.

[9] J. I. Pankove, E. A. Miller, and Berkeyhe.Je, "Gan Electroluminescent Diodes," *Rca Review,* vol. 32, pp. 383-&, 1971.

[10] P. Perlin, T. Suski, M. Leszczynski, and H. Teisseyre, "Physical properties of the Bulk GaN Cyrstals Grown by the High-Pressure, High Temperature Method," in

*Gan And Related Materials*. vol. 2, S. J. Pearton, Ed. Amsterdam: Gordon and Breach Science Publishers, 1997, pp. 315-332.

[11] C. G. Van De Walle, C. Stampfl, and J. Neugebauer, "Theory of doping and defects in III-V nitrides," *Journal of Crystal Growth,* vol. 189-190, pp. 505-510, June 1998.

[12] S. Yoshida, S. Misawa, and S. Gonda, "Improvements on the electrical and luminescent properties of reactive molecular beam epitaxially grown GaN films by using AlN-coated sapphire substrates," *Applied Physics Letters,* vol. 42, pp. 427-429, 1983.

[13] H. Amano, M. Kito, K. Hiramatsu, and I. Akasaki, "P-Type Conduction in Mg-Doped GaN Treated with Low-Energy Electron Beam Irradiation (LEEBI)," *Japan Journal of Applied Physics,* vol. 28, pp. L2112-L2114, 20 December 1989.

[14] S. Nakamura, N. Iwasa, M. Senoh, and T. Mukai, "Hole Compensation Mechanism of P-Type GaN Films," *Japan Journal of Applied Physics,* vol. 31, pp. 1258-1266, 15 May 1992.

[15] D. R. Lide, *CRC Handbook of Chemistry and Physics*, 78 ed. Boca Raton: CRC Press, 1997.

[16] B. Y. Ber, Y. A. Kudriavtsev, A. V. Merkulov, S. V. Novikov, D. E. Lacklison, J. W. Orton, T. S. Cheng, and C. T. Foxton, "Secondary ion mass spectroscopy investigations of magnesium and carbon doped gallium nitride films grown by molecular beam epitaxy," *Semiconductor Science and Technology,* vol. 13, pp. 71-74, Jan 1998.

[17] Y. Ohba and A. Hatano, "A Study on Strong Memory Effects for Mg Doping in Gan Metalorganic Chemical-Vapor-Deposition," *Journal of Crystal Growth,* vol. 145, pp. 214-218, Dec 1994.

[18] A. J. Ptak, T. H. Myers, L. T. Romano, C. G. Van De Walle, and J. E. Northrup, "Magnesium incorporation in GaN grown by molecular-beam epitaxy," *Applied Physics Letters,* vol. 78, p. 285, 2001.

[19] I. Akasaki, H. Amano, M. Kito , and K. Hiramatsu, "Photoluminescence of Mg-doped p-type GaN and electroluminescence of GaN p-n junction LED," *J. Lumin.,* vol. 48-49, pp. 666-670, January-February 1991.

[20] S. D. Burnham, G. Namkoong, W. Henderson, and W. A. Doolittle, "Mg Doped GaN Using a Valved, Thermally Energetic Source: Enhanced Incorporation, Control and Quantitative Optimization," in *Mater. Res. Soc.*, Boston, MA, USA, 2003, pp. Y8.11.1-Y8.11.6.

[21] S. D. Burnham, W. A. Doolittle, G. Namkoong, and W. Henderson, "Mg doped GaN using a valved, thermally energetic source: enhanced incorporation, control and quantitative optimization," in *Materials Research Society*, Boston, MA, USA, 2004, pp. 479-84.

[22] S. D. Burnham, G. Namkoong, W. Henderson, and W. A. Doolittle, "Mg doped GaN using a valved, thermally energetic source: enhanced incorporation, and control," *Journal of Crystal Growth,* vol. 279, pp. 26-30, 15 May 2005 2005.

[23] S. D. Burnham, G. Namkoong, and W. A. Doolittle, "New Physical Understanding of the Nature of Sublimed Mg and Mg Doped GaN," in *Workshop on Compound Semiconductor Materials and Devices*, M. Goorsky, Ed. Miami, Fl, 2005.

[24] S. D. Burnham and W. A. Doolittle, "Quantitative, In-Situ Growth Regime Characterization of AlN Using Reflection High Energy Electron Diffraction," in *33rd Conference on the Physics and Chemistry of Semiconductor Interfaces* Cocoa Beach, FL, 2006.

[25] S. D. Burnham and W. A. Doolittle, "In situ growth regime characterization of AlN using reflection high energy electron diffraction," *Journal of Vacuum Science & Technology B,* vol. 24, pp. 2100-2104, Jul 2006.

[26] S. D. Burnham, G. Namkoong, K.-K. Lee, and W. A. Doolittle, "Reproducible RHEED signatures for in situ growth regime characterization of AlN," in *24th North American Conference on Molecular Beam Epitaxy*, J. M. Millunchick, Ed. Durham, NC, 2006.

[27] S. D. Burnham, G. Namkoong, K.-K. Lee, and W. A. Doolittle, "Reproducible RHEED signatures for improvement of AlN using in situ growth regime characterization," *Journal of Vacuum Science and Technology B (Microelectronics Processing and Phenomena),* Submitted 2006.

[28] S. D. Burnham, E. W. Thomas, and W. A. Doolittle, "Resistivity analysis of expitaxially grown, doped semiconductors using energy dependent secondary ion mass spectroscopy," *Journal of Applied Physics,* vol. 100, p. 113719, 2006.

[29] G. Namkoong, W. A. Doolittle, and A. S. Brown, "Incorporation of Mg in GaN grown by plasma-assisted molecular beam epitaxy," *Applied Physics Letters,* vol. 77, pp. 4386-4388, December 25 2000.

[30] A. Roth, *Vacuum Sealing Techniques*. New York: Springer, 1994.

[31] M. A. Herman, W. Richter, and H. Sitter, *Epitaxy: Physical principles and technical implementation* vol. 62. Berlin: Springer, 2004.

[32] J. E. Davey and T. Pankey, "Epitaxial Gaas Films Deposited by Vacuum Evaporation," *Journal of Applied Physics,* vol. 39, pp. 1941-&, 1968.

[33] A. Y. Cho, "Molecular Beam Epitaxy of GaAs," in *3rd Int. Symp. on Gallium Arsenide and Related Compounds Conference Series*: The Institute of Physics, 1970, pp. 18-29.

[34] A. Y. Cho, "How molecular beam epitaxy (MBE) began and its projection into the future," *Journal of Crystal Growth,* vol. 202, pp. 1-7, May 1999.

[35] G. Namkoong, W. A. Doolittle, A. S. Brown, M. Losurdo, M. M. Giangregorio, and G. Bruno, "The impact of substrate nitridation temperature and buffer design and synthesis on the polarity of GaN epitaxial films," *Journal of Crystal Growth,* vol. 252, pp. 159-166, 2003.

[36] H. Lüth and H. Ibach, *Solid-State Physics: An Introduction to Principles of Materials Science*. Berlin: Springer, 2003.

[37] S. Strite and H. Morkoc, "GaN, AlN, and InN: A review," *Journal of Vacuum Science & Technology B (Microelectronics and Nanometer Structures),* vol. 10, pp. 1237-1266, 1992.

[38] L. Liu and J. H. Edgar, "Substrates for gallium nitride epitaxy," *Materials Science & Engineering R-Reports,* vol. 37, pp. 61-127, Apr 2002.

[39] E. S. Hellman, "The polarity of GaN: a critical review," *MRS Internet Journal of Nitride Semiconductor Research,* vol. 3, p. 11, 1998.

[40] S. C. Binari and H. B. Dietrich, "III-V Nitride Electronic Devices," in *GaN and Related Materials*, S. J. Pearton, Ed. Amsterdam: Gordon and Breach Science Publishers, 1997, pp. 509-534.

[41] M. S. Shur and M. A. Khan, "GaN and AlGaN Devices: Field Effect Transistors and Photodetectors," in *Gan and Related Materials II*. vol. 7, S. J. Pearton, Ed. Amsterdam: Gordon and Breach Science Publishers, 2000, pp. 47-92.

[42] E. F. Schubert, "http://www.lightemittingdiodes.org," Troy, NY: Rensselaer Polytechnic Institute, 2006.

[43] R. F. Pierret, *Advanced Semiconductor Fundamentals*, Second ed. vol. VI. Upper Saddle River, New Jersey: Prentice Hall, 2003.

[44] A. S. Barker and M. Ilegems, "Infrared Lattice-Vibrations and Free-Electron Dispersion in Gan," *Physical Review B,* vol. 7, pp. 743-750, 1973.

[45] M. Shur, *GaAs Devices and Circuits*. New York: Plenum Press, 1987.

[46] G. D. Chen, M. Smith, J. Y. Lin, H. X. Jiang, S. H. Wei, M. A. Khan, and C. J. Sun, "Fundamental optical transitions in GaN," *Applied Physics Letters,* vol. 68, pp. 2784-2786, May 1996.

[47] "Physical & Electronic Properties," http://www.cree.com/products/sic_sub_prop.asp, Ed. Durham, NC: Cree, Inc., 2006.

[48] J. E. Northrup, J. Neugebauer, R. M. Feenstra, and A. R. Smith, "Structure of GaN(0001): The laterally contracted Ga bilayer model," *Physical Review B (Condensed Matter and Materials Physics),* vol. 61, p. 9932, 2000.

[49] C. Adelmann, J. Brault, G. Mula, B. Daudin, L. Lymperakis, and J. Neugebauer, "Gallium adsorption on (0001) GaN surfaces," *Physical Review B (Condensed Matter and Materials Physics),* vol. 67, p. 165419, 2003.

[50] A. R. Smith, R. M. Feenstra, D. W. Greve, M. S. Shin, M. Skowronski, J. Neugebauer, and J. E. Northrup, "GaN(0001) surface structures studied using scanning tunneling microscopy and first-principles total energy calculations," *Surface Science,* vol. 423, p. 70, 1999.

[51] C. D. Lee, Y. Dong, R. M. Feenstra, J. E. Northrup, and J. Neugebauer, "Reconstructions of the AlN(0001) surface," *Physical Review B (Condensed Matter and Materials Physics),* vol. 68, p. 205317, 2003.

[52] B. Heying, R. Averbeck, L. F. Chen, E. Haus, H. Riechert, and J. S. Speck, "Control of GaN surface morphologies using plasma-assisted molecular beam epitaxy," *Journal of Applied Physics,* vol. 88, pp. 1855-1860, 15 Aug. 2000.

[53] C. Adelmann, J. Brault, D. Jalabert, P. Gentile, H. Mariette, G. Mula, and B. Daudin, "Dynamically stable gallium surface coverages during plasma-assisted molecular-beam epitaxy of (0001) GaN," *Journal of Applied Physics,* vol. 91, p. 9638, 2002.

[54] G. Koblmüller, R. Averbeck, L. Geelhaar, H. Riechert, W. Hosler, and P. Pongratz, "Growth diagram and morphologies of AlN thin films grown by molecular beam epitaxy," *Journal of Applied Physics,* vol. 93, pp. 9591-9596, 2003.

[55] "Sapphire Transmission Curve," http://www.redoptronics.com/sapphire-optical-material.html, Ed. Mountain View, CA: Red Optronics, 2006.

[56] N. Koide, H. Kato, M. Sassa, S. Yamasaki, K. Manabe, M. Hashimoto, H. Amano, K. Hiramatsu, and I. Akasaki, "Doping of Gan with Si and Properties of Blue M/I/N/N+ Gan Led with Si-Doped N+-Layer by Movpe," *Journal of Crystal Growth,* vol. 115, pp. 639-642, Dec 1991.

[57] W. Gotz, R. S. Kern, C. H. Chen, H. Liu, D. A. Steigerwald, and R. M. Fletcher, "Hall-effect characterization of III-V nitride semiconductors for high efficiency light emitting diodes," *Materials Science and Engineering B-Solid State Materials for Advanced Technology,* vol. 59, pp. 211-217, May 1999.

[58] J. B. Webb, H. Tang, S. Rolfe, and J. A. Bardwell, "Semi-insulating C-doped GaN and high-mobility AlGaN/GaN heterostructures grown by ammonia molecular beam epitaxy," *Applied Physics Letters,* vol. 75, pp. 953-955, Aug 1999.

[59] H. Amano, I. Akasaki, T. Kozawa, K. Hiramatsu, N. Sawaki, K. Ikeda, and Y. Ishii, "Electron-Beam Effects on Blue Luminescence of Zinc-Doped Gan," *Journal of Luminescence,* vol. 40-1, pp. 121-122, Feb 1988.

[60] L. Pauling, "The Properties of Solutions," in *General Chemistry* New York: Dover Publications, 1970, pp. 447-480.

[61] P. Vennegues, M. Leroux, S. Dalmasso, M. Benaissa, P. De Mierry, P. Lorenzini, B. Damilano, B. Beaumont, J. Massies, and P. Gibart, "Atomic structure of pyramidal defects in Mg-doped GaN," *Physical Review B,* vol. 68, Dec 2003.

[62] J. P. Schaffer, A. Saxena, S. D. Antolovich, T. H. Sanders, Jr., and S. B. Warner, "Crystal Structures," in *The Science and Design of Engineering Materials* Boston: McGraw-Hill, 1999, pp. 60-109.

[63] J. Neugebauer and C. G. Van de Walle, "Theory of point defects and complexes in GaN," *Materials Research Society Symposium - Proceedings,* vol. 395, pp. 645-656, 1996.

[64] Q. A. Sun, A. Selloni, T. H. Myers, and W. A. Doolittle, "Energetics of Mg incorporation at GaN(0001) and GaN(0001) surfaces," *Physical Review B,* vol. 73, Apr 2006.

[65] S. Figge, R. Kroger, T. Bottcher, P. L. Ryder, and D. Hommel, "Magnesium segregation and the formation of pyramidal defects in p-GaN," *Applied Physics Letters,* vol. 81, pp. 4748-4750, Dec 2002.

[66] V. Ramachandran, R. M. Feenstra, W. L. Sarney, L. Salamanca-Riba, J. E. Northrup, L. T. Romano, and D. W. Greve, "Inversion of wurtzite GaN(0001) by exposure to magnesium," *Applied Physics Letters,* vol. 75, pp. 808-810, Aug 1999.

[67] B. Beaumont, S. Haffouz, and P. Gibart, "Magnesium induced changes in the selective growth of GaN by metalorganic vapor phase epitaxy," *Applied Physics Letters,* vol. 72, pp. 921-923, Feb 1998.

[68] Z. Liliental-Weber, M. Benamara, W. Swider, J. Washburn, I. Grzegory, S. Porowski, D. J. H. Lambert, C. J. Eiting, and R. D. Dupuis, "Mg-doped GaN: Similar defects in bulk crystals and layers grown on Al2O3 by metal-organic chemical-vapor deposition," *Applied Physics Letters,* vol. 75, pp. 4159-4161, Dec 1999.

[69] P. Vennegues, M. Benaissa, B. Beaumont, E. Feltin, P. De Mierry, S. Dalmasso, M. Leroux, and P. Gibart, "Pyramidal defects in metalorganic vapor phase

epitaxial Mg doped GaN," *Applied Physics Letters,* vol. 77, pp. 880-882, Aug 2000.

[70] M. L. Timmons, P. K. Chiang, and S. V. Hattangady, "An alternative Mg precursor for p-type doping of OMVPE grown material," *Journal of Crystal Growth,* vol. 77, pp. 37-41, 1986.

[71] Veeco, "Vapor Pressure Data For Selected Elements," http://www.veeco.com/library/elements/images/VaporPress2b_large.jpg, 2006.

[72] H. Luth, "Preparation of Well-Defined Surfaces, Interfaces and Thin Films," in *Solid Surfaces, Interfaces and Thin Films* New York: Springer, 2001, pp. 33-76.

[73] M. Ohring, "Thin-Film Evaporation Process," in *Materials Science of Thin Films*, 2nd ed San Diego: Academic Press, 2002, pp. 95-144.

[74] Veeco, "Crucible dimensions of a high temperature source," St. Paul: http://www.veeco.com/pdfs.php/220, 2005.

[75] B. Y. Ber, Y. A. Kudriavtsev, A. V. Merkulov, S. V. Novikov, D. E. Lacklison, J. W. Orton, T. S. Cheng, and C. T. Foxon, "Secondary ion mass spectroscopy investigations of magnesium and carbon doped gallium nitride films grown by molecular beam epitaxy," *Semiconductor Science and Technology,* vol. 13, pp. 71-74, Jan 1998.

[76] P. Kozodoy, H. L. Xing, S. P. DenBaars, U. K. Mishra, A. Saxler, R. Perrin, S. Elhamri, and W. C. Mitchel, "Heavy doping effects in Mg-doped GaN," *Journal of Applied Physics,* vol. 87, pp. 1832-1835, Feb 2000.

[77] H. Nakayama, P. Hacke, M. R. H. Khan, T. Detchprohm, K. Hiramatsu, and N. Sawaki, "Electrical transport properties of p-GaN," *Japanese Journal of Applied Physics Part 2-Letters,* vol. 35, pp. L282-L284, Mar 1996.

[78] I. Akasaki, H. Amano, M. Kito , and K. Hiramatsu, "Photoluminescence of Mg-doped p-type GaN and electroluminescence of GaN p-n junction LED," *Journal of Luminescence,* vol. 48-49, pp. 666-670, January-February 1991.

[79] W. Kim, A. Salvador, A. E. Botchkarev, O. Aktas, S. N. Mohammad, and H. Morcoc, "Mg-doped p-type GaN grown by reactive molecular beam epitaxy," *Applied Physics Letters,* vol. 69, pp. 559-561, Jul 1996.

[80] W. Gotz, N. M. Johnson, J. Walker, D. P. Bour, and R. A. Street, "Activation of acceptors in Mg-doped GaN grown by metalorganic chemical vapor deposition," *Applied Physics Letters,* vol. 68, pp. 667-669, Jan 1996.

[81] T. Tanaka, A. Watanabe, H. Amano, Y. Kobayashi, I. Akasaki, S. Yamazaki, and M. Koike, "P-Type Conduction in Mg-Doped Gan and Al0.08ga0.92n Grown by Metalorganic Vapor-Phase Epitaxy," *Applied Physics Letters,* vol. 65, pp. 593-594, Aug 1994.

[82] A. Bhattacharyya, W. Li, J. Cabalu, T. D. Moustakas, D. J. Smith, and R. L. Hervig, "Efficient p-type doping of GaN films by plasma-assisted molecular beam epitaxy," *Applied Physics Letters,* vol. 85, pp. 4956-4958, Nov 2004.

[83] D. Huang, F. Yun, M. A. Reshchikov, D. Wang, H. Morkoc, D. L. Rode, L. A. Farina, C. Kurdak, K. T. Tsen, S. S. Park, and K. Y. Lee, "Hall mobility and carrier concentration in free-standing high quality GaN templates grown by hydride vapor phase epitaxy," *Solid-State Electronics,* vol. 45, pp. 711-715, May 2001.

[84] S. Nakamura, M. Senoh, and T. Mukai, "Highly P-Typed Mg-Doped Gan Films Grown with Gan Buffer Layers," *Japanese Journal of Applied Physics Part 2-Letters,* vol. 30, pp. L1708-L1711, Oct 1991.

[85] D. W. Covington and E. L. Meeks, "Unintentional dopants incorporated in GaAs layers grown by molecular beam epitaxy," *Journal of Vacuum Science & Technology,* vol. 16, pp. 847-850, 1979.

[86] J. Neugebauer and C. G. Vandewalle, "Hydrogen in Gan - Novel Aspects of a Common Impurity," *Physical Review Letters,* vol. 75, pp. 4452-4455, Dec 1995.

[87] S. Nakamura, T. Mukai, M. Senoh, and N. Iwasa, "Thermal Annealing Effects on P-Type Mg-Doped GaN Films," *Japan Journal of Applied Physics,* vol. 31, pp. L139-L142, 15 February 1992.

[88] B. C. Chung and M. Gershenzon, "The Influence of Oxygen on the Electrical and Optical-Properties of Gan Crystals Grown by Metalorganic Vapor-Phase Epitaxy," *Journal of Applied Physics,* vol. 72, pp. 651-659, Jul 1992.

[89] M. Suzuki, J. Nishio, M. Onomura, and C. Hongo, "Doping characteristics and electrical properties of Mg-doped AlGaN grown by atmospheric-pressure MOCVD," *Journal of Crystal Growth,* vol. 190, pp. 511-515, Jun 1998.

[90] H. Obloh, K. H. Bachem, U. Kaufmann, M. Kunzer, M. Maier, A. Ramakrishnan, and P. Schlotter, "Self-compensation in Mg doped p-type GaN grown by MOCVD," *Journal of Crystal Growth,* vol. 195, pp. 270-273, Dec 1998.

[91] M. McLaurin, T. E. Mates, and J. S. Speck, "Molecular-beam epitaxy of p-type m-plane GaN," *Applied Physics Letters,* vol. 86, Jun 2005.

[92] H. M. Ng, D. Doppalapudi, D. Korakakis, R. Singh, and T. D. Moustakas, "MBE growth and doping of III-V nitrides," *Journal of Crystal Growth,* vol. 190, pp. 349-353, Jun 1998.

[93] M. S. Brandt, N. M. Johnson, R. J. Molnar, R. Singh, and T. D. Moustakas, "Hydrogenation of P-Type Gallium Nitride," *Applied Physics Letters,* vol. 64, pp. 2264-2266, Apr 1994.

[94] H. Amano, N. Sawaki, I. Akasaki, and Y. Toyoda, "Metalorganic vapor phase epitaxial growth of a high quality GaN film using an AlN buffer layer," *Applied Physics Letters,* vol. 48, pp. 353-355, February 3 1986.

[95] E. Haus, I. P. Smorchkova, B. Heying, P. Fini, C. Poblenz, T. Mates, U. K. Mishra, and J. S. Speck, "The role of growth conditions on the p-doping of GaN by plasma-assisted molecular beam epitaxy," *Journal of Crystal Growth,* vol. 246, pp. 55-63, Dec 2002.

[96] L. S. McCarthy, I. P. Smorchkova, H. Xing, P. Kozodoy, P. Fini, J. Limb, D. L. Pulfrey, J. S. Speck, M. J. W. Fodwell, S. P. DenBaars, and U. K. Mishra, "GaN HBT: toward an RF device," *IEEE Transactions on Electron Devices,* vol. 48, pp. 543-551, March 2001.

[97] Veeco, "Veeco MBE corrosive series valved cracker," Veeco Instruments Inc., 2003.

[98] I. Berishev, E. Kim, A. Fartassi, M. Sayhi, and A. Bensoula, "Mg doping studies of electron cyclotron resonance molecular beam epitaxy of GaN thin films," *Journal of Vacuum Science & Technology A (Vacuum, Surfaces, and Films),* vol. 17, pp. 2166-2169, 1999.

[99] C. Pahlke, H. Dusterhoft, and U. Muller-Jahreis, "Measurements of the energy distributions of positive secondary ions in the energy range from 0 to about 500 eV," in *International Conference on Secondary Ion Mass Spectrometry*. vol. 3, A. Benninghoven, Ed. Budapest, Hungary: Springer-Verlag, Berlin, 1982, p. 124.

[100] P. A. W. Van Der Heide, "A systematic study of the characteristic velocities of the negative secondary ion emissions of H, O and matrix species from Sc, Ti, V, Co, Ni and Cu substrates," *Surface Science,* vol. 365, p. 473, 1996.

[101] W. M. Lau, "Energy distributions of secondary ions from GaAs," *Nuclear Instruments & Methods in Physics Research, Section B (Beam Interactions with Materials and Atoms),* vol. B16, p. 41, 1986.

[102] K. Wittmaack, "Design and performance of quadrupole-based SIMS instruments: a critical review," *Vacuum,* vol. 32, p. 65, 1982.

[103] B. A. Tsipinyuk and V. I. Veksler, "Energy spectra of secondary ions and secondary ion emission (SIE) mechanisms," *Vacuum,* vol. 29, p. 155, 1979.

[104] M. A. Rudat and G. H. Morrison, "Energy spectra of ions sputtered from elements by O/sub 2//sup +/: a comprehensive study," *Surface Science,* vol. 82, p. 549, 1979.

[105] P. H. Dawson, "SIMS studies of the adsorption of O/sub 2/, CO and CO/sub 2/ on titanium using low primary energies," *Surface Science,* vol. 65, p. 41, 1977.

[106] Z. Sroubek, "The theoretical and experimental study of the ionization processes during the low energy ion sputtering," *Surface Science,* vol. 44, p. 47, 1974.

[107] H. Yamazaki, "Matrix effects in SIMS analysis of high-dose boron implanted silicon wafers," *Nuclear Instruments & Methods in Physics Research, Section B (Beam Interactions with Materials and Atoms),* vol. 134, p. 121, 1998.

[108] K. Wittmaack, "Depth profiling by means of SIMS: recent progress and current problems," *Radiation Effects,* vol. 63, p. 205, 1982.

[109] K. Wittmaack, "Primary-ion charge compensation in SIMS analysis of insulators," *Journal of Applied Physics,* vol. 50, p. 493, 1979.

[110] T. Hasegawa, T. Date, A. Karen, and A. Masuda, "Study on change in SIMS intensities near the interface between silicon-nitride film and silicon substrate," *Applied Surface Science,* vol. 231-232, p. 725, 2004.

[111] P. H. Chi, D. S. Simons, A. E. Wickenden, and D. D. Koleske, "Repeatability of Si concentration measurements in Si-doped GaN films," *Journal of Vacuum Science & Technology A (Vacuum, Surfaces, and Films),* vol. 15, p. 2565, 1997.

[112] Veeco, "The Use of a Valved Mg Source for Improved p-type Doping of MBE-Growth GaN," Veeco Compound Semiconductor MBE Operations, 2004, pp. 1-4.

[113] H. Gnaser and H. Oechsner, "The influence of polarizability an the emission of sputtered molecular ions," *Surface Science,* vol. 302, p. 289, 1994.

[114] E. W. Thomas and A. Torabi, "SIMS analysis using ejected CsX/sup +/ ions," *Nuclear Instruments & Methods in Physics Research, Section B (Beam Interactions with Materials and Atoms),* vol. B73, pp. 214-20, 1993.

[115] D. L. Albritton, "Ion-neutral reaction-rate constants measured in flow reactors through 1977," *Atomic Data and Nuclear Data Tables,* vol. 22, p. 1, 1978.

[116] M. F. Dumke, T. A. Tombrello, R. A. Weller, R. M. Housley, and E. H. Cirlin, "Sputtering of the gallium-indium eutectic alloy in the liquid phase," *Surface Science,* vol. 124, p. 407, 1983.

[117] P. Williams, "Secondary Ion Mass Spectrometry," in *Applied Atomic Collision Physics: Condensed Matter*. vol. 4, S. Datz, Ed. Orlando: Academic Press, Inc., 1983, pp. 327-377.

[118] R. G. Wilson, F. A. Stevie, and C. W. Magee, *Secondary Ion Mass Spectrometry*. New York: Wiley, 1989.

[119] Z. L. Liau, J. W. Mayer, W. L. Brown, and J. M. Poate, "Sputtering of PtSi," *Journal of Applied Physics,* vol. 49, pp. 5295-5305, 1978.

[120] http://www.eeel.nist.gov/812/hall.html, "Hall Effect Measurements," National Institute of Standards and Technology, 2002.

[121] C. E. C. Wood, "RED intensity oscillations during MBE of GaAs," *Surface Science,* vol. 108, pp. 441-3, 1981.

[122] R. Held and D. E. Crawford, "N-limited versus Ga-limited growth on GaN(0001) by MBE using NH/sub 3," *Surface Review and Letters,* vol. 5, pp. 913-34, 1998.

[123] B. Daudin and F. Widmann, "Layer-by-layer growth of AlN and GaN by molecular beam epitaxy," *Journal of Crystal Growth,* vol. 182, pp. 1-5, 1997.

[124] K. R. Evans, R. Kaspi, W. T. Cooley, C. R. Jones, and J. S. Solomon, "Arbitrary composition profiles by MBE using desorption mass spectrometry," in *Mater. Res. Soc.*, San Francisco, CA, USA, 1993, pp. 495-500.

[125] M. McLaurin, B. Haskell, S. Nakamura, and J. S. Speck, "Gallium adsorption onto (1120) gallium nitride surfaces," *Journal of Applied Physics,* vol. 96, p. 327, 2004.

[126] J. Massies and N. Grandjean, "Real-time control of the molecular beam epitaxy of nitrides," *Journal of Crystal Growth,* vol. 202, pp. 382-387, May 1999.

[127] M. S. Shur and M. A. Khan, "GaN/AlGaN heterostructure devices: photodetectors and field-effect transistors," *MRS Bulletin,* vol. 22, pp. 44-50, 1997.

[128] K. R. Evans, C. E. Stutz, E. N. Taylor, and J. E. Ehret, "Incorporation/desorption rate variation at heterointerfaces in III-V molecular-beam epitaxy," *Journal of Vacuum Science and Technology B (Microelectronics Processing and Phenomena),* vol. 9, pp. 2427-32, 1991.

[129] R. Z. Bachrach, "Metal-Semiconductor Surface and Interface States on (110) Gaas," *Journal of Vacuum Science & Technology,* vol. 15, pp. 1340-1343, 1978.

[130] K. Mahalingam, D. L. Dorsey, K. R. Evans, and R. Venkatasubramanian, "A Monte Carlo study of gallium desorption kinetics during MBE of (100)-GaAs/AlGaAs heterostructures," *Journal of Crystal Growth,* vol. 175-176, pp. 211-15, 1997.

[131] C. D. Lee, Y. Dong, R. M. Feenstra, J. E. Northrup, and J. Neugebauer, "Growth and surface reconstructions of AlN(0001) films," in *Mater. Res. Soc.*, Boston, MA, USA, 2004, pp. 317-22.

[132] Y. Horikoshi, M. Kawashima, and H. Yamaguchi, "Photoluminescence Characteristics of Algaas-Gaas Single Quantum-Wells Grown by Migration-Enhanced Epitaxy at 300-Degrees-C Substrate-Temperature," *Applied Physics Letters,* vol. 50, pp. 1686-1687, Jun 1987.

[133] C. Poblenz, P. Waltereit, and J. S. Speck, "Uniformity and control of surface morphology during growth of GaN by molecular beam epitaxy," *Journal of Vacuum Science & Technology B,* vol. 23, pp. 1379-1385, Jul-Aug 2005.

[134] Y. Horikoshi, M. Kawashima, and H. Yamaguchi, "Low-Temperature Growth of Gaas and Alas-Gaas Quantum-Well Layers by Modified Molecular-Beam Epitaxy," *Japanese Journal of Applied Physics Part 2-Letters,* vol. 25, pp. L868-L870, Oct 1986.

[135] D. Sugihara, A. Kikuchi, K. Kusakabe, S. Nakamura, Y. Toyoura, T. Yamada, and K. Kishino, "High-quality GaN on AlN multiple intermediate layer with migration enhanced epitaxy by rf-molecular beam epitaxy," *Japanese Journal of Applied Physics Part 2-Letters,* vol. 39, pp. L197-L199, Mar 2000.

[136] N. Teraguchi, A. Suzuki, Y. Saito, T. Yamaguchi, T. Araki, and Y. Nanishi, "Growth of AlN films on SiC substrates by RF-MBE and RF-MEE," *Journal of Crystal Growth,* vol. 230, pp. 392-397, Sep 2001.

[137] H. Lu, W. J. Schaff, J. Hwang, H. Wu, W. Yeo, A. Pharkya, and L. F. Eastman, "Improvement on epitaxial grown of InN by migration enhanced epitaxy," *Applied Physics Letters,* vol. 77, pp. 2548-2550, Oct 2000.

[138] A. G. O. Mutambara, "Characteristics of Feedback Control Systems," in *Design and Analysis of Control Systems* Boca Raton: CRC Press, 1999, p. 264.

[139] Basler, "Basler A601f-HDR User's Manual," Germany: Basler, Inc, 2004.

[140] T. N. Cornsweet, *Visual Perception*. New York: Academic Press, 1970.

[141] F. B. Naranjo, M. A. Sanchez-Garcia, F. Calle, E. Calleja, B. Jenichen, and K. H. Ploog, "Strong localization in InGaN layers with high In content grown by molecular-beam epitaxy," *Applied Physics Letters,* vol. 80, pp. 231-233, Jan 2002.

[142] I. Stanley, G. Coleiny, and R. Venkat, "Theoretical study of In desorption and segregation kinetics in MBE growth of InGaAs and InGaN," *Journal of Crystal Growth,* vol. 251, pp. 23-28, Apr 2003.

[143] S. Kang, "The epitaxial growth of GaN and AlGaN/GaN Heterostructure Field Effect Transistors (HFET) on Lithium Gallate ($LiGaO_2$) substrates," in *Electrical and computer engineering* Atlanta, Ga: Georgia Institute of Technology, 2002

[144] J. W. Orton, C. T. Foxon, T. S. Cheng, S. E. Hooper, S. V. Novikov, B. Y. Ber, and Y. A. Kudriavtsev, "Incorporation of Mg in GaN grown by molecular beam epitaxy," *Journal of Crystal Growth,* vol. 197, pp. 7-11, Feb 1999.

[145] K. Saarinen, T. Laine, S. Kuisma, J. Nissila, P. Hautojarvi, L. Dobrzynski, J. M. Baranowski, K. Pakula, R. Stepniewski, M. Wojdak, A. Wysmolek, T. Suski, M. Leszczynski, I. Grzegory, and S. Porowski, "Observation of native Ga vacancies in GaN by positron annihilation," *Physical Review Letters,* vol. 79, pp. 3030-3033, Oct 1997.

[146] W. Gotz, N. M. Johnson, and D. P. Bour, "Deep level defects in Mg-doped, p-type GaN grown by metalorganic chemical vapor deposition," *Applied Physics Letters,* vol. 68, pp. 3470-3472, Jun 1996.

[147] H. Nagai, Q. S. Zhu, Y. Kawaguchi, K. Hiramatsu, and N. Sawaki, "Hole trap levels in Mg-doped GaN grown by metalorganic vapor phase epitaxy," *Applied Physics Letters,* vol. 73, pp. 2024-2026, Oct 1998.

[148] W. R. Runyan and T. J. Shaffner, "Impurity Concentration," in *Semiconductor Measurements and Instrumentation*, 2nd ed New York: McGraw-Hill, 1998, pp. 70-104.

[149] D. Seghier and H. P. Gislason, "Correlation between deep levels and the persistent photoconductivity in Mg-doped GaN grown MOCVD," *Journal of Physics D-Applied Physics,* vol. 35, pp. 291-294, Feb 2002.

[150] Y. Nakano and T. Kachi, "Current deep-level transient spectroscopy investigation of acceptor levels in Mg-doped GaN," *Applied Physics Letters,* vol. 79, pp. 1631-1633, Sep 2001.

[151] Q. S. Zhu, H. Nagai, Y. Kawaguchi, K. Hiramatsu, and N. Sawaki, "Effect of thermal annealing on hole trap levels in Mg-doped GaN grown by metalorganic vapor phase epitaxy," *Journal of Vacuum Science & Technology A,* vol. 18, pp. 261-267, Jan-Feb 2000.

[152] P. Hacke, H. Nakayama, T. Detchprohm, K. Hiramatsu, and N. Sawaki, "Deep levels in the upper band-gap region of lightly Mg-doped GaN," *Applied Physics Letters,* vol. 68, pp. 1362-1364, Mar 1996.

[153] Y. Nakano and T. Jimbo, "Electrical characterization of acceptor levels in Mg-doped GaN," *Journal of Applied Physics,* vol. 92, pp. 5590-5592, Nov 2002.

[154] D. Seghier and H. P. Gislason, "Electrical characterization of Mg-related energy levels and the compensation mechanism in GaN : Mg," *Journal of Applied Physics,* vol. 88, pp. 6483-6487, Dec 2000.

[155] S. D. Burnham and W. A. Doolittle, "A new growth kinetics model for AlN, based on DMS observations " in *Workshop on Compound Semiconductor Materials and Devices* Savannah, Ga, 2007.

[156] M. Diale, F. D. Auret, N. G. van der Berg, R. Q. Odendaal, and W. D. Roos, "Analysis of GaN cleaning procedures," *Applied Surface Science,* vol. 246, pp. 279-289, 2004.

[157] Z. Liu, Y. Sun, F. Machuca, P. Pianetta, and W. E. Spicer, "Optimization and characterization of III-V surface cleaning," *Journal of Vacuum Science & Technology B,* vol. 21, p. 1953, 2003.

[158] F. Machuca, Z. Liu, Y. Sun, P. Pianetta, W. E. Spicer, and R. F. W. Pease, "Simple method for cleaning gallium nitride (0001)," *Journal of Vacuum Science & Technology A (Vacuum, Surfaces, and Films),* vol. 20, p. 1784, 2002.

[159] R. Bresnahan, "Georgia Tech UNI-Bulb™ RF Source Aperture Options," Veeco Instruments, Inc., St. Paul, MN 2007.

[160] L. J. van der Pauw, "A Method of Measuring Specific Resistivity and Hall Effect of Discs of Arbitrary Shape," *Phil. Res. Rep.,* vol. 13, pp. 1-9, Feb. 1958.

[161] L. J. van der Pauw, "A Method of Measuring the Resistivity and Hall Coefficient on Lamellae of Arbitrary Shape," *Phil. Tech. Rev.,* vol. 20, pp. 220-224, Aug. 1958.

[162] R. Chwang, B. J. Smith, and C. R. Crowell, "Contact Size Effects on the van der Pauw Method for Resistivity and Hall Coefficient Measurement," *Solid State Electronics,* vol. 17, pp. 1217-1227, Dec. 1974.

[163] F. M. Li and A. Nathan, "Silicon Dioxide," in *CCD Image Sensors In Deep-Ultraviolet: Degradation Behavior and Damage Mechanisms* Netherlands: Springer, 2005, pp. 51-80.

[164] D. K. Schroder, "Defects," in *Semiconductor Materials and Device Characterization*, 3rd ed Hoboken, New Jersey: John Wiley & Sons, Inc., 2006, pp. 270-285.

[165] A. Zylbersztejn, "Trap Depth and Electron-Capture Cross-Section Determination by Trap Refilling Experiments in Schottky Diodes," *Applied Physics Letters,* vol. 33, pp. 200-202, 1978.

[166] W. A. Doolittle and A. Rohatgi, "A Novel Computer-Based Pseudologarithmic Capacitance Conductance Dlts System Specifically Designed for Transient Analysis," *Review of Scientific Instruments,* vol. 63, pp. 5733-5741, Dec 1992.

[167] E. H. Nicollian and A. Goetzberger, "Si-Sio2 Interface - Electrical Properties as Determined by Metal-Insulator-Silicon Conductance Technique," *Bell System Technical Journal,* vol. 46, pp. 1055-1133, July/Aug. 1967.

[168] R. H. Bube, "Transient photoelectronic analysis," in *Photoelectronic Properties of Semiconductors* Cambridge: Cambridge University Press, 1992, pp. 149-189.

[169] *Scanning Probe Microscopy Training Notebook*: Digital Instruments, Veeco Metrology Group, 1998.

[170] "The 16th series of cantilevers datasheets," http://www.spmtips.com/products/cantilevers/datasheets/dp16/: MikroMasch, May, 2007.

[171] N. Brailko, "n-Surf Image Processor," http://www.n-surf.com/, 2004.

[172] P. Klapetek and D. Necas, "Gwyddion," http://gwyddion.net, 2006.

[173] "Basler A601f-HDR User's Manual," http://www.baslerweb.com/downloads/12065/A601f-HDR_Users_Manual_DA00065902.pdf: Basler, Inc, 2004.

[174] "IEEE Standard for a High Performance Serial Bus (Amendment)," http://standards.ieee.org/, May, 2007.

[175] A. J. Springthorpe and A. Majeed, "Epitaxial-Growth Rate Measurements During Molecular-Beam Epitaxy," *Journal of Vacuum Science & Technology B,* vol. 8, pp. 266-270, Mar-Apr 1990.

[176] A. J. Springthorpe, T. P. Humphreys, A. Majeed, and W. T. Moore, "Insitu Growth-Rate Measurements During Molecular-Beam Epitaxy Using an Optical-Pyrometer," *Applied Physics Letters,* vol. 55, pp. 2138-2140, Nov 1989.

[177] S. Nakamura, "Insitu Monitoring of Gan Growth Using Interference Effects," *Japanese Journal of Applied Physics Part 1-Regular Papers Short Notes & Review Papers,* vol. 30, pp. 1620-1627, Aug 1991.

[178] H. M. Ng, S. N. G. Chu, and A. Y. Cho, "In situ determination of growth rate by pyrometric interferometry during molecular-beam epitaxy: Application to the growth of AlGaN/GaN quantum wells," *Journal of Vacuum Science & Technology a-Vacuum Surfaces and Films,* vol. 19, pp. 292-294, Jan-Feb 2001.

[179] L. Considine, E. J. Thrush, J. A. Crawley, K. Jacobs, W. Van der Stricht, I. Moerman, P. Demeester, G. H. Park, S. J. Hwang, and J. J. Song, "Growth and in situ monitoring of GaN using IR interference effects," *Journal of Crystal Growth,* vol. 195, pp. 192-198, Dec 1998.

[180] T. L. Tansley, M. Goldys, M. Godlewski, Z. B., and H. Y. Zuo, "The Contribution of Defects to the Electrical and Optical Properties of GaN," in *GaN and Related*

*Materials*, S. J. Pearton, Ed. Amsterdam, Netherlands: Gordon and Breach Science Publishers, 1997, p. 268.

# VITA

## INTRODUCTION

In June of 2007, Shawn Burnham was a graduate research assistant for Dr. William Alan Doolittle in the School of Electrical and Computer Engineering at the Georgia Institute of Technology in Atlanta, Georgia. Mr. Burnham was born and raised in Mobile, Al, and graduated Summa Cum Laude from Auburn University when receiving his Bachelor's degree in Electrical Engineering in 2001. He received his Master's degree in Electrical Engineering from Georgia Tech in 2002, and was expected to receive his Ph.D. in Electrical Engineering from Georgia Tech in 2007. During his research at Georgia Tech, his principle interest has been the development of nitride-based semiconductor materials and devices, specifically through innovative growth characterization and growth implementation techniques. At the time, Mr. Burnham had authored or coauthored over 17 research papers and presentations since 2004, over 5 per year. Although his interests have centered on plasma enhanced molecular beam epitaxy for III-Nitride electronic and optoelectronic devices, he has also published innovative work for novel electrical characterization of films using secondary ion mass spectroscopy, and was responsible for the development, assembly, control and first growths from an experimental metalorganic molecular beam epitaxy growth system which allows wide-band optical interaction during growth. However, work on *in situ*

characterization has been his focus, resulting in new growth techniques and growth models. Mr. Burnham was married to Kathryn Hill in December of 2002.

EDUCATION

Georgia Institute of Technology – Atlanta, Georgia

Ph.D. – Electrical Engineering 12/02 – 8/07 (Expected)

- Research Area: Improving understanding and control of Mg doped GaN
- Minor: Materials Science and Engineering
- GPA: 3.87/4.0

M.S. – Electrical Engineering 8/01 – 12/02

- Technical Areas: Microelectronics, Computer Engineering, Electronic Design and Applications
- Minor: Management
- GPA: 3.90/4.0

Auburn University – Auburn, Alabama

B.S. – Electrical Engineering (Computer Engineering Option) 3/98 – 5/01

- Summa Cum Laude
- GPA: 3.95/4.0

University Of South Alabama – Mobile, Alabama

B.S. – Computer Engineering 9/96 – 3/98 (Transfer)

SCHOLARLY ACCOMPLISHMENTS

**First author publications and presentations**

- **S. D. Burnham**, G. Namkoong, K.-K. Lee, and W. A. Doolittle, "Reproducible reflection high energy electron diffraction signatures for improvement of AlN

using in situ growth regime characterization," *Journal of Vacuum Science and Technology B (Microelectronics Processing and Phenomena),* vol. 25, pp. 1009-1013, May 2007.

- **S. D. Burnham**, E. W. Thomas, and W. A. Doolittle, "Resistivity analysis of epitaxially grown, doped semiconductors using energy dependent secondary ion mass spectroscopy," *Journal of Applied Physics*, vol. 100, p. 113719, 2006.
- **S. D. Burnham** and W. A. Doolittle, "*In situ* growth regime characterization of AlN using reflection high energy electron diffraction," *Journal of Vacuum Science & Technology B*, vol. 24, pp. 2100-2104, 2006.
- **S. D. Burnham**, G. Namkoong, W. Henderson, and W. A. Doolittle, "Mg doped GaN using a valved, thermally energetic source: enhanced incorporation, and control," *Journal of Crystal Growth*, vol. 279, pp. 26-30, 2005.
- **S. D. Burnham** and W. A. Doolittle, "A new growth kinetics model for AlN, based on DMS observations," presented at the Workshop on Compound Semiconductor Materials and Devices, Savannah, GA, 2007.
- **S. D. Burnham**, G. Namkoong, K.-K. Lee, and W. A. Doolittle, "Reproducible RHEED signatures for *in situ* growth regime characterization of AlN," presented at the 24th North American Conference on Molecular Beam Epitaxy, Durham, NC, 2006.
- **S. D. Burnham** and W. A. Doolittle, "Quantitative, *In Situ* Growth Regime Characterization of AlN Using Reflection High Energy Electron Diffraction," presented at the 33rd Conference on the Physics and Chemistry of Semiconductor Interfaces, Cocoa Beach, FL, 2006.

- **S. D. Burnham**, G. Namkoong, and W. A. Doolittle, "New Physical Understanding of the Nature of Sublimed Mg and Mg Doped GaN," presented at the Workshop on Compound Semiconductor Materials and Devices, Miami, FL, 2005.
- **S. D. Burnham**, W. A. Doolittle, G. Namkoong, and W. Henderson, "Mg doped GaN using a valved, thermally energetic source: enhanced incorporation, control and quantitative optimization," *Material Research Society Symposium Proceedings*, vol. 798, pp. 479-84, Boston, MA, 2004.

**Contributing author publications and presentations**

- D. Pritchett, W. Henderson, **S. D. Burnham**, and W. A. Doolittle, "Influence of growth conditions and surface reaction byproducts on GaN grown via metal organic molecular beam epitaxy: Toward an understanding of surface reaction chemistry," *Journal of Electronic Materials,* vol. 35, pp. 562-567, Apr 2006.
- G. Namkoong, **S. D. Burnham**, K.-K. Lee, E. Trybus, W. A. Doolittle, M. Losurdo, P. Capezzuto, G. Bruno, B. Nemeth, and J. Nause, "III-nitrides on oxygen- and zinc-face ZnO substrates," *Applied Physics Letters*, vol. 87, pp. 184104-3, 2005.
- E. Trybus, G. Namkoong, W. Henderson, **S. D. Burnham**, W. A. Doolittle, M. Cheung, and A. Cartwright, "InN: A material with Photovoltaic Promise and Challenges," *Journal of Crystal Growth*, vol. 288, pp. 218, 2005.
- D. Pritchett, W. Henderson, **S. D. Burnham**, and W. A. Doolittle, "Influence of Intense Ultraviolet Photoexcitation on Surface Reactions during Gallium Nitride Growth via Metal Organic Molecular Beam Epitaxy," presented at 33rd

Conference on the Physics and Chemistry of Semiconductor Interfaces, Cocoa Beach, FL, 2006.

- D. Pritchett, **S. D. Burnham**, W. Henderson, and W. A. Doolittle, "Metalorganic Molecular Beam Epitaxy (MOMBE) of GaN: Towards an Understanding of Surface Reaction Chemistry," presented at 47th TMS 2005 Electronic Materials Conference, Santa Barbara, CA, 2005.
- E. Trybus, W. A. Doolittle, W. Henderson, G. Namkoong, **S. D. Burnham**, K.-K. Lee, I. Ferguson, and C. Honsberg, "InN: Revolutionary Photovoltaic Material or Just a Revolting Material," presented at Workshop on Compound Semiconductor Materials and Devices, Miami, FL, 2005.
- Invited: W. A. Doolittle, E. Trybus, W. Henderson, G. Namkoong, **S. D. Burnham**, K. Lee, I. Ferguson, and C. Honsberg, "InN: A Material with Photovoltaic Promise and Challenges," AFOSR Indium Nitride Workshop 2, Jan. 9-13, 2005, Kailua-Kona, Hawaii.
- W. A. Doolittle, **S. D. Burnham**, G. Namkoong, and W. Henderson, "Mg Doped GaN Using A Valved, Thermally Energetic Source: Enhanced Incorporation, Control and Quantitative Optimization," Workshop on Compound Semiconductor Materials and Devices (WOCSEMMAD), Jan. 2004, Pasadena, CA.

Note: a commercial application note was written, based entirely on the first author's work:

- Veeco, "The Use of a Valved Mg Source for Improved p-type Doping of MBE-Growth GaN," Veeco Compound Semiconductor MBE Operations, 2004, pp. 1-4.